

Riemannian Batch Normalization: A Gyro Approach

Ziheng Chen*

University of Trento, Italy

ZIHENG_CH@163.COM

Xiao-Jun Wu

Jiangnan University, China

WU_XIAOJUN@JIANGNAN.EDU.CN

Bernhard Schölkopf

Max Planck Institute for Intelligent Systems, Germany

BERNHARD.SCHOELKOPF@TUEBINGEN.MPG.DE

Nicu Sebe

University of Trento, Italy

NICULAE.SEBE@UNITN.IT

Abstract

Normalization layers are crucial for deep learning, but their Euclidean formulations are inadequate for data on manifolds. On the other hand, many Riemannian manifolds in machine learning admit gyro-structures, enabling principled extensions of Euclidean neural networks to non-Euclidean domains. Inspired by this, we introduce GyroBN, a principled Riemannian batch normalization framework for gyrogroups. We establish two necessary conditions, namely *pseudo-reduction* and *gyroisometric gyrations*, that guarantee GyroBN with theoretical control over sample statistics, and show that these conditions hold for all known gyrogroups in machine learning. Our framework also incorporates several existing Riemannian normalization methods as special cases. We further instantiate GyroBN on seven representative geometries, including the Grassmannian, five constant curvature spaces, and the correlation manifold, and derive novel gyro and Riemannian structures to enable these instantiations. Experiments across these geometries demonstrate the effectiveness of GyroBN. The code is available at <https://github.com/GitZH-Chen/GyroBN.git>.

Keywords: Normalization, Riemannian Manifolds, Gyrogroups, Constant Curvature Spaces, Matrix Manifolds

1 Introduction

Deep Neural Networks (DNNs) on Riemannian manifolds have attracted increasing attention in diverse machine learning applications, such as computer vision (Huang et al., 2017; Huang and Van Gool, 2017; Huang et al., 2018; Skopek et al., 2020; Chen et al., 2023b; Gao et al., 2023; Wang et al., 2024b; Chen et al., 2025b), natural language processing (Ganea et al., 2018; Shimizu et al., 2021), drone classification (Brooks et al., 2019; Chen et al., 2024a), human neuroimaging (Pan et al., 2022; Kobler et al., 2022a; Bonet et al., 2023; Ju et al., 2024; Wang et al., 2024a; Li et al., 2025; Hu et al., 2025), medical imaging (Huang et al., 2019; Chakraborty et al., 2020), node and graph classification (Chami et al., 2019; Dai et al., 2021; Zhao et al., 2023; Chen et al., 2023a, 2024c), and genome sequence modeling (Khan

*. Corresponding Author.

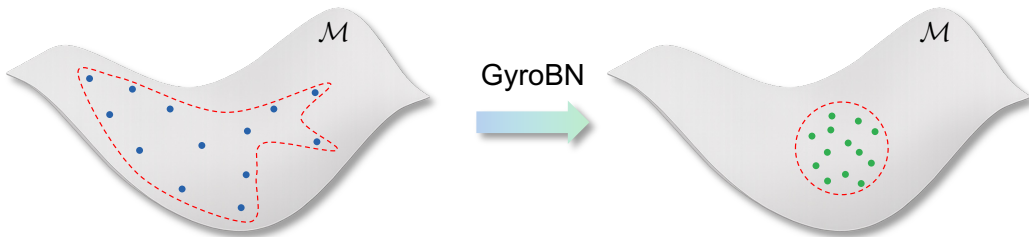


Figure 1: Illustration of GyroBN on manifold-valued data. Blue points, green points, and the red dashed curves indicate the input samples, normalized outputs, and data distributions, respectively.

et al., 2025). As in the Euclidean setting, normalization layers (Ioffe and Szegedy, 2015; Ba et al., 2016; Ulyanov et al., 2016; Wu and He, 2018) play a central role in facilitating training, motivating their adaptation to manifold-valued data.

Despite this need, most existing Riemannian normalization methods are restricted to specific geometries or cannot normalize sample statistics. For example, Brooks et al. (2019); Kobler et al. (2022a) introduced SPD Batch Normalization (SPDBN) on Symmetric Positive Definite (SPD) manifolds under the specific Affine-Invariant Metric (AIM), while Chakraborty (2020) proposed a Riemannian Batch Normalization (RBN) framework for homogeneous spaces. However, these approaches often fail to guarantee principled control of sample mean and variance. Similar limitations appear in Lou et al. (2020) and Bdeir et al. (2024). Chen et al. (2024b) further developed the RBN for general Lie groups, termed Lie Group Batch Normalization (LieBN). Although LieBN can normalize sample statistics, many important geometries in machine learning do not admit a Lie group structure. As a result, existing methods still lack a principled solution for Riemannian normalization.

Recently, gyro-structures have emerged as effective tools for building Riemannian networks across various geometries, including SPD (Nguyen, 2022b,a), Grassmannian (Nguyen, 2022a), hyperbolic (Ganea et al., 2018), and spherical manifolds (Skopek et al., 2020). They naturally extend Euclidean vector structures while encompassing Lie groups and non-group geometries. For instance, the Grassmannian, hyperbolic, and spherical manifolds do not form Lie groups but instead form gyrogroups.

Based on the analysis above, this paper introduces Gyrogroup Batch Normalization (GyroBN), a general RBN framework on gyrogroups, as illustrated in Figure 1. We employ gyrosubtraction, gyroaddition, and scalar gyromultiplication to generalize the centering (vector subtraction), biasing (vector addition), and scaling (scalar multiplication) in Euclidean Batch Normalization (BN) to curved manifolds in a principled manner. We clarify why centering and biasing in GyroBN rely on *left* gyroaddition, rather than other candidates, such as right gyroaddition or gyrocoaddition (Ungar, 2022, Definition. 2.9). To broaden the scope, we relax the classical gyrogroup to the *pseudo-reductive gyrogroup*, and show that when gyrations are *gyroisometries*, GyroBN enjoys theoretical control over sample statistics. These conditions are satisfied by all known gyrogroups in machine learning, providing a principled and unified normalization mechanism. Moreover, several existing RBN methods arise as special cases of GyroBN, including LieBN on Lie groups and various SPD-based variants, as summarized in Table 1.

Method	Controllable Statistics	Applied Geometries	Incorporated by GyroBN
SPDBN (Brooks et al., 2019)	M	SPD manifolds under AIM	✓
SPDBN (Kobler et al., 2022b)	M+V	SPD manifolds under AIM	✓
SPDDSMNB (Kobler et al., 2022a)	M+V	SPD manifolds under AIM	✓
ManifoldNorm (Chakraborty, 2020, Algorithms 1-2)	N/A	Riemannian homogeneous space	✗
ManifoldNorm (Chakraborty, 2020, Algorithms 3-4)	M+V	Matrix Lie groups under the distance $d(X, Y) = \ \text{mlog}(X^{-1}Y)\ $	✓
RBN (Lou et al., 2020, Algorithm 2)	N/A	Geodesically complete manifolds	✗
LieBN (Chen et al., 2024b)	M+V	Lie groups	✓
GyroBN	M+V	Pseudo-reductive gyrogroups with gyroisometric gyrations	N/A

Table 1: Comparison of previous RBN methods with our GyroBN, where M and V denote the sample mean and variance.

On the implementation side, we instantiate GyroBN on seven representative geometries: the Grassmannian (Bendokat et al., 2024), five constant curvature spaces (Ganea et al., 2018; Lee, 2018; Bachmann et al., 2020), and the full-rank correlation manifold (Thanwerdas and Pennek, 2022). For the Grassmannian, we propose an efficient implementation. For constant curvature spaces, we cover five models: Poincaré ball, hyperboloid, Beltrami–Klein, sphere, and projected hypersphere. To enable these instantiations, we refine the projected hypersphere structure (Bachmann et al., 2020), derive closed-form gyro-structures for the hyperboloid and sphere, and develop the Riemannian structure of the Beltrami–Klein model. For the correlation manifold, we demonstrate that its gyro-structure can be defined row-wise on its Cholesky factor. To facilitate adoption, we release a PyTorch-compatible toolbox (Paszke et al., 2019) with drop-in GyroBN layers, illustrated in Figure 2. Experiments on networks over these seven geometries validate the effectiveness of our framework.

In summary, our *main contributions* are

- Theoretical foundation: pseudo-reductive gyrogroups as a relaxation of classical gyrogroups;
- General framework: GyroBN as a plug-and-play normalization mechanism, with pseudo-reduction and gyroisometric gyrations ensuring theoretical control of batch statistics;
- Geometric insights: refined projected hypersphere gyro-structure, closed-form hyperboloid and sphere gyro-structures, Riemannian structure of the Beltrami–Klein model, and row-wise correlation manifold gyro-structure;
- Practical instantiations: implementations on the Grassmannian, five constant curvature spaces, and the correlation manifold with extensive experiments.

Outline. Section 2 reviews the background on Riemannian geometry, gyro-structures, and the manifolds considered in this work. Section 3 introduces pseudo-reductive gyrogroups and analyzes their theoretical properties, while Section 4 develops the GyroBN framework. Section 5 shows that prior RBN methods are our special cases, and instantiate our GyroBN

```

from GyroBN import *
from GyroBN.Geometry import *

# ==== Grassmannian ====
manifold = GrassmannianGyro(n=50, p=10)
X_gr = manifold.random_normal(30, 50, 10)
gybn_gr = GyroBNGr(shape=[50, 10])
out_gr = gybn_gr(X_gr)

# ==== Five Constant Curvature Spaces (CCSs) ====
models = [
    ("Poincare", Stereographic(K=-1.0)),
    ("Hyperboloid", Hyperboloid(K=-1.0)),
    ("Klein", Klein(K=-1.0)),
    ("Sphere", Sphere(K= 1.0)),
    ("ProjSphere", Stereographic(K= 1.0)),
]
for name, manifold in models:
    X_ccs = manifold.random_normal(30, 16)
    gybn_ccs = GyroBNCCS(shape=[16], model=name, K=manifold.K)
    out_ccs = gybn_ccs(X_ccs)

# ==== Full-Rank Correlation ====
manifold = CorPolyHyperbolicCholeskyMetric(n=10)
X_cor = manifold.random(30, 10, 10)
gybn_cor = GyroBNCor(shape=[10, 10])
out_cor = gybn_cor(X_cor)

```

Figure 2: Minimal examples of applying GyroBN.

on seven representative geometries. Section 6 reports experiments that validate GyroBN across these geometries. Section 7 concludes the paper. All proofs are deferred to Section E.

This paper extends our ICLR work (Chen et al., 2025c) both methodologically and in implementation. On the methodological side, we provide justification for why GyroBN relies on left gyroaddition. On the implementation side, we broaden the framework beyond the Grassmannian and Poincaré geometries to additional constant curvature spaces and the correlation manifold, introducing novel gyro and Riemannian structures. We further expand the experiments and release an open-source PyTorch toolbox.

2 Preliminaries

This section reviews the necessary background on Riemannian geometry, gyro-structures, and concrete gyrogroups in machine learning. For in-depth discussion of Riemannian manifolds and gyrospaces, we refer the reader to Lee (2018) and Ungar (2022), respectively.

2.1 Riemannian Geometry

Notation. For the Euclidean space \mathbb{R}^n (resp. $\mathbb{R}^{n \times n}$), we denote $\langle \cdot, \cdot \rangle$ as the standard Euclidean inner product on vectors (resp. Frobenius inner product on matrices), with $\|\cdot\|$ as the induced norm: the L_2 norm for vectors and the Frobenius norm for matrices. The zero vector and zero matrix are denoted uniformly by $\mathbf{0}$. For points on general manifolds, we use lowercase letters (e.g., x, y, z) unless the elements are matrix-valued, in which case we use uppercase letters (e.g., P, Q, R). A summary of notations is provided in Section A.

Riemannian Manifold. A Riemannian manifold (\mathcal{M}, g) , abbreviated as \mathcal{M} , carries a smoothly varying Riemannian metric $g_x : T_x\mathcal{M} \times T_x\mathcal{M} \rightarrow \mathbb{R}$ on each tangent space $T_x\mathcal{M}$. The induced norm is $\|v\|_x = \sqrt{g_x(v, v)}$. As an inner product, g_x is also denoted as $\langle \cdot, \cdot \rangle_x$. For a smooth curve $\gamma : [0, 1] \rightarrow \mathcal{M}$, its length is $L(\gamma) = \int_0^1 \|\dot{\gamma}(t)\|_{\gamma(t)} dt$, and the associated geodesic distance is $d(x, y) = \inf_{\gamma(0)=x, \gamma(1)=y} L(\gamma)$.

Geodesic. Straight lines are generalized to constant-speed curves that are locally length-minimizing between points $x, y \in \mathcal{M}$, known as geodesics:

$$\gamma^* = \arg \min_{\gamma} L(\gamma) \quad \text{subject to } \gamma(0) = x, \gamma(1) = y, \|\dot{\gamma}(t)\|_{\gamma(t)} = 1.$$

Exponential and Logarithmic Maps. For $x \in \mathcal{M}$ and $v \in T_x\mathcal{M}$, let $\gamma_{x,v}$ denote the unique geodesic with $\gamma_{x,v}(0) = x$ and $\dot{\gamma}_{x,v}(0) = v$. The exponential map $\text{Exp}_x : T_x\mathcal{M} \supset \mathcal{V} \rightarrow \mathcal{M}$ is defined by $\text{Exp}_x(v) = \gamma_{x,v}(1)$, where \mathcal{V} is an open neighborhood of the origin in $T_x\mathcal{M}$. Its local inverse, defined for y in a neighborhood $\mathcal{U} \subset \mathcal{M}$ of x , is the logarithmic map $\text{Log}_x : \mathcal{U} \rightarrow T_x\mathcal{M}$, satisfying $\text{Exp}_x \circ \text{Log}_x = \mathbb{1}_{\mathcal{U}}$. On Cartan–Hadamard manifolds, that is, complete and connected Riemannian manifolds with non-positive sectional curvature, the exponential and logarithmic maps are globally defined (Lee, 2018, Proposition 12.19). Representative cases include SPD, hyperbolic, and correlation manifolds. Throughout this paper, we assume that Exp_x and Log_x are globally defined, with numerical remedies adopted when singularities arise.

Parallel Transport. Given a geodesic γ from x to y , the parallel transport of a tangent vector $v \in T_x\mathcal{M}$ is the unique vector $\text{PT}_{x \rightarrow y}(v) \in T_y\mathcal{M}$ obtained by transporting v along γ so that its covariant derivative along γ vanishes. Parallel transport defines a linear isometry between $T_x\mathcal{M}$ and $T_y\mathcal{M}$.

Table 2 compares the corresponding operators in Euclidean and Riemannian geometries.

Isometry. The isometries generalize the bijection into the Riemannian geometry. If $\{\mathcal{M}, g\}$ and $\{\widetilde{\mathcal{M}}, \widetilde{g}\}$ are both Riemannian manifolds, a smooth map $f : \mathcal{M} \rightarrow \widetilde{\mathcal{M}}$ is called a (Riemannian) isometry if it is a diffeomorphism that satisfies

$$g_x(v, w) = \widetilde{g}_{f(x)}(f_{*,x}(v), f_{*,x}(w)),$$

where $f_{*,x}(\cdot) : T_x\mathcal{M} \rightarrow T_{f(x)}\widetilde{\mathcal{M}}$ is the differential map of f at $x \in \mathcal{M}$, and $v, w \in T_x\mathcal{M}$ are two tangent vectors.

Lie Group. A manifold is a Lie group, if it forms a group with a group operation \odot such that $m(x, y) \mapsto x \odot y$ and $i(x) \mapsto x_{\odot}^{-1}$ are both smooth, where x_{\odot}^{-1} is the group inverse of x .

Operation	Euclidean space	Riemannian manifold
Straight line	Straight line	Geodesic
Subtraction	$\vec{xy} = y - x$	$\vec{xy} = \text{Log}_x(y)$
Addition	$y = x + \vec{xy}$	$y = \text{Exp}_x(\vec{xy})$
Parallely moving	$v \rightarrow v$	$\text{PT}_{x \rightarrow y}(v)$

Table 2: The geometric reinterpretations of Riemannian operators.

2.2 Gyro-Structures

Definition 1 (Gyrogroups (Ungar, 2022)). Given a nonempty set G with a binary operation $\oplus : G \times G \rightarrow G$, (G, \oplus) forms a gyrogroup if its binary operation satisfies the following axioms for any $x, y, z \in G$:

(G1) There is at least one element $e \in G$ called a left identity (or neutral element) such that $e \oplus x = x$.

(G2) There is an element $\ominus x \in G$ called a left inverse of x such that $\ominus x \oplus x = e$.

(G3) There is an automorphism $\text{gyr}[x, y] : G \rightarrow G$ for each $x, y \in G$ such that

$$x \oplus (y \oplus z) = (x \oplus y) \oplus \text{gyr}[x, y]z \quad (\text{Left Gyroassociative Law}).$$

The automorphism $\text{gyr}[x, y]$ is called the gyroautomorphism, or the gyration of G generated by x, y .

(G4) Left reduction law: $\text{gyr}[x, y] = \text{gyr}[x \oplus y, y]$.

Definition 2 (Gyrocommutative Gyrogroups (Ungar, 2022)). A gyrogroup (G, \oplus) is gyrocommutative if it satisfies

$$x \oplus y = \text{gyr}[x, y](y \oplus x) \quad (\text{Gyrocommutative Law}).$$

Definition 3 (Nonreductive Gyrogroups (Nguyen, 2022a)). A groupoid (G, \oplus) is a nonreductive gyrogroup if it satisfies axioms (G1), (G2), and (G3).

Definition 4 (Gyrovector Spaces). A gyrocommutative gyrogroup (G, \oplus) equipped with a scalar gyromultiplication $\odot : \mathbb{R} \times G \rightarrow G$ is called a gyrovector space if it satisfies the following axioms for $s, t \in \mathbb{R}$ and $x, y, z \in G$:

(V1) Identity Scalar Multiplication: $1 \odot x = x$.

(V2) Scalar Distributive Law: $(s + t) \odot x = s \odot x \oplus t \odot x$.

(V3) Scalar Associative Law: $(st) \odot x = s \odot (t \odot x)$.

(V4) Gyroautomorphism: $\text{gyr}[x, y](t \odot z) = t \odot \text{gyr}[x, y]z$.

(V5) Identity Gyroautomorphism: $\text{gyr}[s \odot x, t \odot x] = \mathbb{1}$, where $\mathbb{1}$ is the identity map.

Remark 5. Nguyen (2022a) presented a similar definition, except that (V1) is defined as $1 \odot x = x$, $0 \odot x = t \odot e = e$, and $(-1) \odot x = \ominus x$. However, as implied by Ungar (2022, Theorem 6.4), $0 \odot x = t \odot e = e$, $(-1) \odot x = \ominus x$ are redundant.

Intuitively, gyrogroups are natural generalizations of groups. Unlike groups, gyrogroups are non-associative but have gyroassociativity characterized by gyrations. Since gyrations in any

(Lie) group are the identity map, every (Lie) group is automatically a gyrogroup. Similarly, the gyrovector space generalizes the vector space, which has shown impressive success in hyperbolic geometry (Ungar, 2022). Although this work employs scalar gyromultiplication, we do not require it to satisfy the axioms of a gyrovector space. Nevertheless, we present Theorem 4 for completeness.

2.3 Gyro-Structures over Manifolds

As shown by Nguyen and Yang (2023), for $x, y, z \in \mathcal{M}$ and $t \in \mathbb{R}$, the gyro-structure is defined as¹

$$\text{Gyroaddition: } x \oplus y = \text{Exp}_x(\text{PT}_{e \rightarrow x}(\text{Log}_e(y))), \quad (1)$$

$$\text{Scalar gyromultiplication: } t \odot x = \text{Exp}_e(t \text{Log}_e(x)), \quad (2)$$

$$\text{Gyroinverse: } \ominus x = -1 \odot x = \text{Exp}_e(-\text{Log}_e(x)), \quad (3)$$

$$\text{Gyration: } \text{gyr}[x, y]z = (\ominus(x \oplus y)) \oplus (x \oplus (y \oplus z)), \quad (4)$$

$$\text{Gyro inner product: } \langle x, y \rangle_{\text{gyr}} = \langle \text{Log}_e(x), \text{Log}_e(y) \rangle_e, \quad (5)$$

$$\text{Gyronorm: } \|x\|_{\text{gyr}} = \langle x, x \rangle_{\text{gyr}}, \quad (6)$$

$$\text{Gyrodistance: } d_{\text{gyr}}(x, y) = \|\ominus x \oplus y\|_{\text{gyr}}, \quad (7)$$

where e is the gyro identity element, and Log_e and $\langle \cdot, \cdot \rangle_e$ is the Riemannian logarithm and metric at e . A bijection $\omega : G \rightarrow G$ is called gyroisometry, if it preserves the gyrodistance:

$$d_{\text{gyr}}(\omega(x), \omega(y)) = d_{\text{gyr}}(x, y).$$

2.4 Examples

Several geometries in machine learning admit (nonreductive) gyrogroups.

SPD Manifold (Pennec et al., 2006). The set \mathcal{S}_{++}^n of $n \times n$ SPD matrices form a manifold, named the SPD manifold. We focus on three popular Riemannian metrics on the SPD manifold: Affine-Invariant Metric (AIM) (Pennec et al., 2006), Log-Euclidean Metric (LEM) (Arsigny et al., 2005), and Log-Cholesky Metric (LCM) (Lin, 2019). As shown by Nguyen (2022a, Section 3.1), each metric can induce a distinct gyro-structure via Equation (1)–Equation (7). Besides, the gyrogroups under the LEM and LCM coincide with the Lie groups proposed by Arsigny et al. (2005); Lin (2019), respectively.

Grassmannian Manifold (Bendokat et al., 2024). The Grassmannian is the set of p -dimensional subspace of n -dimensional vector space. It has two matrix representations, the Projector Perspective (PP) and Orthonormal Basis (ONB) perspective:

$$\text{PP: } \widetilde{\text{Gr}}(p, n) = \{P \in \mathcal{S}^n : P^2 = P, \quad \text{rank}(P) = p\},$$

$$\text{ONB: } \text{Gr}(p, n) = \{[U] : [U] := \{\tilde{U} \in \text{St}(p, n) \mid \tilde{U} = UR, \quad R \in \text{O}(p)\}\},$$

where \mathcal{S}^n is the Euclidean space of symmetric matrices, $\text{St}(p, n)$ is the Stiefel manifold, and $\text{O}(p)$ is the orthogonal group. By abuse of notations, we use $[U]$ and U interchangeably for

1. Nguyen and Yang (2023) assume all involved Riemannian operators are well-defined. For each singular cases in this paper, we will provide numerical solutions, which will be discussed in Section 5.

the element of $\text{Gr}(p, n)$, where the $n \times p$ column-wise orthonormal matrix U should be taken as a representative of an equivalence class. Helmke and Moore (2012) show that the ONB perspective is diffeomorphic to the PP by

$$\pi : \text{Gr}(p, n) \ni U \mapsto UU^\top \in \widetilde{\text{Gr}}(p, n). \quad (8)$$

As shown by Nguyen (2022a, Section 3.2) and Nguyen and Yang (2023, Section 2.3.1), the Grassmannian admits a gyrocommutative and nonreductive gyrogroup defined by Equation (1)–Equation (7).

K-Stereographic Model (Bachmann et al., 2020). It is defined as

$$\mathfrak{st}_K^n = \left\{ x \in \mathbb{R}^n : \|x\|^2 < -1/K \right\}, \text{ with } g_x^K = (\lambda_x^K)^2 g^E,$$

where $K \in \mathbb{R}$ is the constant curvature, $\lambda_x^K = \frac{2}{(1+K\|x\|^2)}$ is a conformal factor, g^K is its Riemannian metric, and $g^E = \langle \cdot, \cdot \rangle$ is the standard inner product. Particularly, \mathfrak{st}_K^n is the scaled \mathbb{R}^n when $K = 0$. It unifies the spherical projected hypersphere \mathbb{D}_K^n , Euclidean \mathbb{R}^n , and hyperbolic Poincaré ball \mathbb{P}_K^n :

$$\mathfrak{st}_K^n = \begin{cases} \mathbb{D}_K^n = \mathbb{R}^n, & \text{For } K > 0, \text{ spherical geometry,} \\ \mathbb{R}^n, & \text{For } K = 0, \text{ Euclidean geometry,} \\ \mathbb{P}_K^n = \left\{ x \in \mathbb{R}^n : \|x\|^2 < -1/K \right\}, & \text{For } K < 0, \text{ hyperbolic geometry.} \end{cases}$$

Although $\mathbb{D}_K^n = \mathbb{R}^n$ for $K < 0$, its metric is conformal to the Euclidean one. We will abbreviate the *K*-stereographic model as the stereographic model. Bachmann et al. (2020, Equations. 2–3) shows that this model admits a gyro-structure.

K-Radius Model (Skopek et al., 2020). It provides an extrinsic representation of the space with constant curvature $K \in \mathbb{R}$, encompassing the sphere \mathbb{S}_K^n , Euclidean space \mathbb{R}^n , and hyperboloid \mathbb{H}_K^n :

$$\mathcal{M}_K^n = \begin{cases} \mathbb{S}_K^n = \left\{ x \in \mathbb{R}^{n+1} : \|x\|^2 = \frac{1}{K} \right\}, & \text{For } K > 0, \text{ spherical geometry,} \\ \mathbb{R}^n, & \text{For } K = 0, \text{ Euclidean geometry,} \\ \mathbb{H}_K^n = \left\{ x \in \mathbb{R}^{n+1} : \|x\|_{\mathcal{L}}^2 = \frac{1}{K}, x_t > 0 \right\}, & \text{For } K < 0, \text{ hyperbolic geometry,} \end{cases}$$

where $\|x\|_{\mathcal{L}}^2 = \|x_s\|^2 - x_t^2$ is the Lorentz inner product. Following the conventions of the hyperboloid, we write $x = (x_t, x_s^\top)^\top$, with $x_t \in \mathbb{R}$ as the time component and $x_s \in \mathbb{R}^n$ as the spatial component (Ratcliffe, 2006). When $K \neq 0$, the model can be written compactly as

$$\mathcal{M}_K^n = \left\{ x \in \mathbb{R}^{n+1} : \langle x, x \rangle_K = 1/K \right\}, \text{ with } \langle \cdot, \cdot \rangle_K = \begin{cases} \langle \cdot, \cdot \rangle, & K > 0, \\ \langle \cdot, \cdot \rangle_{\mathcal{L}}, & K < 0 \wedge x_t > 0. \end{cases}$$

We abbreviate the *K*-radius model as the radius model. Its gyro-structure is developed in Section 5.5.1.

Geometry	Symbol	$P \oplus Q$ or $x \oplus y$	E	$\ominus P$ or $\ominus x$	Lie group	Gyrogroup	References
AIM \mathcal{S}_{++}^n	\oplus^{AI}	$P^{\frac{1}{2}}QP^{\frac{1}{2}}$	I_n	P^{-1}	✗	✓	(Nguyen, 2022b)
LEM \mathcal{S}_{++}^n	\oplus^{LE}	$\text{mexp}(\text{mlog}(P) + \text{mlog}(Q))$	I_n	P^{-1}	✓	✓	(Arsigny et al., 2005) (Nguyen, 2022b) (Lin, 2019)
LCM \mathcal{S}_{++}^n	\oplus^{LC}	$\psi_{\text{LC}}^{-1}(\psi_{\text{LC}}(P) + \psi_{\text{LC}}(Q))$	I_n	$\psi_{\text{LC}}(-\psi_{\text{LC}}(P))$	✓	✓	(Nguyen, 2022b) (Chen et al., 2024d)
$\widetilde{\text{Gr}}(p, n)$ $\text{Gr}(p, n)$	\oplus^{Gr} \oplus^{Gr}	$\text{mexp}(\Omega)Q \text{mexp}(-\Omega)$ $\text{mexp}(\Omega)V$	$\widetilde{I}_{p,n}$ $\widetilde{I}_{p,n}$	$\text{mexp}(-\Omega)\widetilde{I}_{p,n} \text{mexp}(\Omega)$ $\text{mexp}(-\Omega)\widetilde{I}_{p,n}$	✗	Non-reductive	(Nguyen, 2022a) (Nguyen and Yang, 2023)
\mathfrak{st}_K^n	\oplus_K	$\frac{(1-2K\langle x,y\rangle - K\ y\ ^2)x + (1+K\ x\ ^2)y}{1-2K\langle x,y\rangle + K^2\ x\ ^2\ y\ ^2}$	$\mathbf{0}$	$-x$	✗(✓ for $K=0$)	✓	(Ungar, 2022) (Bachmann et al., 2020) Theorem 22
\mathbb{K}_K^n	\oplus_E	$\frac{1}{1-K\langle x,y\rangle} \left(x + \frac{1}{\gamma_x} y - K \frac{\gamma_x}{1+\gamma_x} \langle x, y \rangle x \right)$	$\mathbf{0}$	$-x$	✗	✓	(Ungar, 2022)

Table 3: Gyrogroup on several geometries.

Beltrami–Klein Model. There are five models over the hyperbolic space (Cannon et al., 1997). Apart from the above Poincaré ball and hyperboloid models, we further study the Beltrami–Klein model:

$$\mathbb{K}_K^n = \left\{ x \in \mathbb{R}^n : \|x\|^2 < -\frac{1}{K} \right\}, \text{ with } g_x^{\mathbb{K}}(v, w) = \frac{\langle v, w \rangle}{1 + K \|x\|^2} - \frac{K \langle x, v \rangle \langle x, w \rangle}{(1 + K \|x\|^2)^2},$$

where $K < 0$ is the constant curvature and $g^{\mathbb{K}}$ is its Riemannian metric. Although the Poincaré ball and Beltrami–Klein models share the same underlying set, their Riemannian metrics differ. This model admits an Einstein gyrovector space (Ungar, 2022, Chapter 6.18).

Full-Rank Correlation. The correlation matrix of a covariance matrix Σ is defined as $C = \text{Cor}(\Sigma) = \mathbb{D}(\Sigma)^{-1/2} \Sigma \mathbb{D}(\Sigma)^{-1/2}$, where $\mathbb{D}(\cdot)$ returns a diagonal matrix with diagonal elements of Σ . The space of $n \times n$ full-rank correlation matrices, denoted as $\text{Cor}^+(n)$, forms a manifold (David and Gu, 2019, Theorem 1), referred to as the correlation manifold. This manifold can be viewed as a compact representation of SPD matrices that preserves scale-invariant information. However, its Riemannian structure has been less studied than SPD matrices. Recently, Thanwerdas and Pennec (2022); Thanwerdas (2024) developed five convenient Riemannian metrics. Among them, Poly-Hyperbolic-Cholesky Metric (PHCM) (Thanwerdas and Pennec, 2022) identifies each correlation matrix with a product of hyperbolic spaces via the Cholesky decomposition. In Section 5.7, we construct the corresponding gyrostructure based on this identification.

Table 3 summarizes the existing gyrogroups on the above geometries. The associated notations are defined as follows.

- Let $\mathcal{M} \in \{\mathcal{S}_{++}^n, \widetilde{\text{Gr}}(p, n)\}$ be a matrix manifold, and consider $P, Q \in \mathcal{M}$. For the Grassmannian, $U = \pi^{-1}(P)$ and $V = \pi^{-1}(Q)$ denote the ONB representations. The matrix exponential, logarithm, and Cholesky decomposition are denoted by mexp , mlog , and \mathcal{L} , respectively. We further define $\psi_{\text{LC}} = \text{Dlog} \circ \mathcal{L}$, where ψ_{LC} is the diagonal logarithm. We write I_n for the $n \times n$ identity matrix, $I_{p,n} = (I_p, 0)^\top \in \mathbb{R}^{n \times p}$ for the ONB identity, and $\widetilde{I}_{p,n} = \pi(I_{p,n})$ for the PP identity. For the Grassmannian $\widetilde{\text{Gr}}(p, n)$, we define $\Omega = [\overline{P}, \widetilde{I}_{p,n}]$, where $\overline{P} = \text{Log}_{\widetilde{I}_{p,n}}(P)$ and $[\cdot, \cdot]$ denote the matrix commutator.

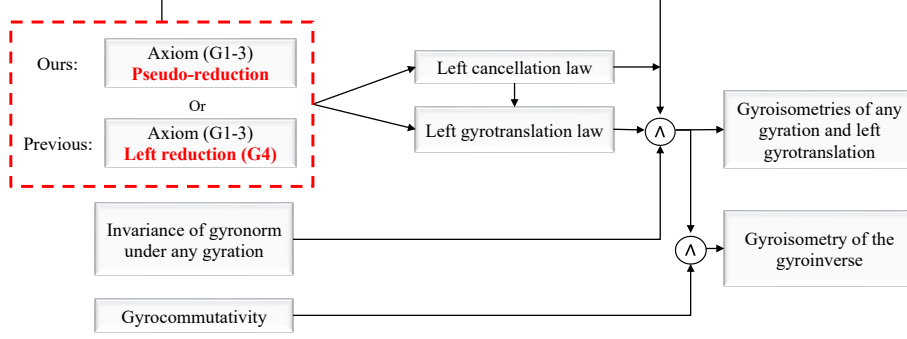


Figure 3: The conceptual comparison of derivation logic of our work against previous work (Nguyen and Yang, 2023), where the left gyrotranslation law is presented in Theorem E.8. The previous work proves the results on the SPD and Grassmannian manifolds in a case-by-case manner. In contrast, we relax the left reduction into pseudo-reduction and give a general analysis. Our framework also corrects the proof for the Grassmannian cases.

- Let $\mathcal{C}_K^n \in \{\mathfrak{st}_K^n, \mathbb{K}_K^n\}$ be a constant curvature space, and consider $x, y \in \mathcal{C}_K^n$. The gamma factor is defined as $\gamma_x = 1/\sqrt{1 + K\|x\|^2}$.

3 Pseudo-Reductive Gyrogroups

Given a gyrogroup (G, \oplus) , the left gyrotranslation by $x \in G$ is defined as

$$L_x : G \rightarrow G, \quad L_x(y) = x \oplus y, \quad \forall y \in G.$$

If any gyrotranslation is a gyroisometry, we can use gyrotranslation to center manifold-valued samples for the normalization layer. Nguyen and Yang (2023) show that any left gyrotranslation on the SPD and Grassmannian manifolds is a gyroisometry. However, the proof relies on the left cancellation law of gyrogroups, which does not hold for nonreductive gyrogroups, such as the Grassmannian. Therefore, the proof is questionable for the Grassmannian. We propose an intermediate structure, referred to as *pseudo-reductive gyrogroups*, which can support the left cancellation law and, therefore, the gyroisometry of gyrotranslation. This will form the algebraic foundation for building the normalization layer. As illustrated in Figure 3, our derivation extends the the case-by-case approach by Nguyen and Yang (2023) into general pseudo-reductive gyrogroups.

3.1 From Gyrogroups to Pseudo-Reductive Gyrogroups

Definition 6 (Pseudo-Reductive Gyrogroups). A groupoid (G, \oplus) is a pseudo-reductive gyrogroup if it satisfies the axioms (G1), (G2), (G3) and the following pseudo-reductive law:

$$\text{gyr}[a, x] = \mathbb{1}, \text{ for any left inverse } a \text{ of } x \text{ in } G, \quad (9)$$

where $\mathbb{1}$ is the identity map.

Equation (9) can be intuitively viewed as the intermediate between reduction and non-reduction. For gyrogroups, Equation (9) can be directly obtained from left gyroassociativity (G3) and reduction (G4) (Ungar, 2022, Theorem 2.10, item 3). However, there is no theoretical guarantee that Equation (9) holds for non-reductive gyrogroups. Therefore, we name Equation (9) pseudo-reduction. Nevertheless, for the specific non-reductive Grassmannian, it is indeed pseudo-reductive.

Proposition 7. \llcorner $\text{Gr}(p, n)$ and $\widetilde{\text{Gr}}(p, n)$ are pseudo-reductive gyrocommutative gyrogroups.

Our pseudo-reductive gyrogroup naturally generalizes the vanilla gyrogroup, as it shares most of the basic properties of gyrogroups (Ungar, 2022, Theorems. 2.10–2.11).

Theorem 8 (First Pseudo-Reductive Gyrogroups Properties). \llcorner Let (G, \oplus) be a pseudo-reductive gyrogroup. For any elements $x, y, z, a \in G$, we have:

1. If $x \oplus y = x \oplus z$, then $y = z$ (General Left Cancellation law; see (8) below).
2. $\text{gyr}[e, x] = \mathbb{1}$ for any left identity e in G .
3. $\text{gyr}[a, x] = \mathbb{1}$ for any left inverse a of x in G .
4. There is a left identity that is a right identity.
5. There is only one left identity.
6. Every left inverse is a right inverse.
7. There is only one left inverse, $\ominus x$, of x , and $\ominus(\ominus x) = x$.
8. The left cancellation law: $\ominus x \oplus (x \oplus y) = y$.
9. The gyrator identity: $\text{gyr}[x, y]a = \ominus(x \oplus y) \oplus \{x \oplus (y \oplus a)\}$.
10. $\text{gyr}[x, y]e = e$.
11. $\text{gyr}[x, y](\ominus a) = \ominus \text{gyr}[x, y]a$.
12. $\text{gyr}[x, e] = \mathbb{1}$.
13. The gyrosum inversion law: $\ominus(x \oplus y) = \text{gyr}[x, y](\ominus y \ominus x)$.

Remark 9. In non-reductive gyrogroups, 2 and 3 are undefined. Consequently, any property relying on them, such as 4 and those from 6 to 10, is not guaranteed to hold. The absence of these basic properties undermines the rationality of non-reductive gyrogroups. In contrast, our pseudo-reductive gyrogroups preserve most of the fundamental properties of gyrogroups.

3.2 Isometries over Pseudo-Reductive Gyrogroups

The gyro-structure in the following is assumed to be defined as Equation (1)–Equation (7). We first clarify that the Riemannian distance agrees with the gyrodistance, and the Riemannian isometry agrees with the gyroisometry. These justify gyrodistance and gyroisometry for gyrospaces over manifolds.

Lemma 10 (Distances). \llcorner Given a pseudo-reductive gyrogroup (\mathcal{M}, \oplus) , we have

$$d(x, y) = \|\text{Log}_x(y)\|_x = \|\ominus x \oplus y\|_{\text{gyr}} = d_{\text{gyr}}(x, y), \quad \forall x, y \in \mathcal{M}, \quad (10)$$

where $e \in \mathcal{M}$ is the origin of the manifold, and d denotes the geodesic distance.²

Lemma 11 (Isometries). \lrcorner Let (\mathcal{M}, \oplus) and $(\widetilde{\mathcal{M}}, \widetilde{\oplus})$ be two pseudo-reductive gyrogroups. Their gyro identity elements are $e \in \mathcal{M}$ and $\widetilde{e} \in \widetilde{\mathcal{M}}$, respectively. Suppose $\phi : \mathcal{M} \rightarrow \widetilde{\mathcal{M}}$ is a Riemannian isometry with $\widetilde{e} = \phi(e)$, we have the following.

1. The Riemannian isometry is a gyroisometry:

$$d_{\text{gyr}}(x, y) = \widetilde{d}_{\text{gyr}}(\phi(x), \phi(y)), \quad (11)$$

where d_{gyr} and $\widetilde{d}_{\text{gyr}}$ are the gyrodistances over \mathcal{M} and $\widetilde{\mathcal{M}}$, respectively.

2. If the gyroinverse, gyration, or left gyrotranslation over \mathcal{M} is a gyroisometry, its counterpart over $\widetilde{\mathcal{M}}$ is also a gyroisometry.

Theorem 10 implies that, as long as the gyro-structure is defined by Equation (1)–Equation (7), the gyrodistance coincides with the geodesic distance. Unless otherwise specified, we shall not distinguish between the two and uniformly denote them by $d(\cdot, \cdot)$. Besides, the second result in Theorem 11 is particularly useful, as several geometries are isometric, such as the ONB and PP Grassmannian, as well as different models in hyperbolic geometry.

Now, we analyze gyroisometries over pseudo-reductive gyrogroups. The most related property in Theorem 8 is the left cancellation law, one of the key prerequisites for gyro translation to be gyroisometry. Note that the left cancellation comes from left gyro associativity and Equation (9) (Ungar, 2022, Theorem 2.10, item 9). Therefore, left cancellation does not generally hold for non-reductive gyrogroups but exists in pseudo-reductive gyrogroups. We first present an iff statement about gyroisometry, which will be useful in the following.

Theorem 12. \lrcorner Given a pseudo-reductive gyrogroup (G, \oplus) , $\text{gyr}[x, y]$ preserves the gyronorm for any $x, y \in G$, iff $\text{gyr}[x, y]$ is a gyroisometry for any $x, y \in G$.

The gyroisometry of any gyration is a prerequisite for other operators to be gyroisometries.

Theorem 13 (Gyroisometries). \lrcorner Given a pseudo-reductive gyrogroup (G, \oplus) with any $\text{gyr}[\cdot, \cdot]$ as a gyroisometry, we have the following.

1. The left gyrotranslation is a gyroisometry.
2. If (G, \oplus) is gyrocommutative, then any gyroinverse is a gyroisometry.

Now, we can discuss the gyroisometries w.r.t. Table 3.

Theorem 14. \lrcorner For the pseudo-reductive gyrogroups corresponding to the SPD manifold (under AIM, LEM, and LCM), the ONB and PP Grassmannian, and the stereographic model with $K \leq 0$ (the Poincaré ball for $K < 0$ and Euclidean space for $K = 0$), the gyrodistance coincides with the geodesic distance. Moreover, the gyroinverse, any gyration, and any left gyrotranslation are gyroisometries.

Proof [Credit and Sketch of the Proof] As Theorem 10 already shows that the gyrodistance coincides with the geodesic distance, it remains to establish the isometries. For the

2. On Cartan–Hadamard manifolds, the statement holds for all $x, y \in \mathcal{M}$. More generally, the equality requires x, y to lie within a geodesic ball of convexity radius to ensure the well-definedness of the minimizing geodesic and logarithm. In this paper, we implicitly assume these conditions are satisfied.

Grassmannian and SPD manifolds, these were proved by Nguyen and Yang (2023, Theorems 2.12–2.14 and 2.16–2.18), although their arguments implicitly treated the non-reductive Grassmannian as a gyrogroup by using left cancellation. Our Theorems 7 and 8 confirms that the Grassmannian is pseudo-reductive and does satisfy left cancellation, thereby validating their results. However, we can directly establish these properties from Theorems 12 and 13. The complete proof is given in Section E.7. \blacksquare

Remark 15. The remaining manifolds in Section 2.4, including the stereographic model with $K > 0$, radius model, and Beltrami–Klein model, also satisfy these properties. Their verifications will be presented in Section 5.

4 GyroBN on Pseudo-Reductive Gyrogroups

Building on Theorem 14, which establishes that several geometries admit isometric gyrotranslations, we develop RBN in a principled way for general pseudo-reductive gyrogroups, referred to as Gyrogroup Batch Normalization (GyroBN). Throughout, we assume (\mathcal{M}, \oplus) is a pseudo-reductive gyrogroup with the gyro-structure defined by Equation (1)–Equation (7).³ As Theorem 10 establishes the equivalence between gyrodistance and geodesic distance, we use the terms “gyromean” and “gyrovariance” interchangeably with their Riemannian counterparts.

4.1 Euclidean Batch Normalization Revisited

As the core operations of different Euclidean normalization variants (Ioffe and Szegedy, 2015; Ba et al., 2016; Ulyanov et al., 2016; Wu and He, 2018) are similar, this paper focuses on BN. Given a batch of activations $\{x_{i \dots N}\}$, the BN update can be expressed as

$$\forall i \leq N, \quad x_i \leftarrow \gamma \frac{x_i - \mu}{\sqrt{v^2 + \epsilon}} + \beta \quad (12)$$

where μ and v^2 denote the mean and variance of the sample, and γ and β are the learnable scaling and bias parameters.

4.2 GyroBN

To generalize the Euclidean BN into gyrogroups, we first define sample mean, sample variance, centering, biasing, and scaling over gyrogroups. Then, we introduce our GyroBN framework with a theoretical analysis of the ability to normalize sample statistics.

We define the gyromean as the Fréchet mean (Fréchet, 1948) under gyrodistance:

$$\mu = \text{FM}(\{x_i \in \mathcal{M}\}_{i=1}^N) = \underset{y \in \mathcal{M}}{\text{argmin}} \frac{1}{N} \sum_{i=1}^N d^2(x_i, y). \quad (13)$$

The gyrovariance is the corresponding Fréchet variance. By Theorem 10, the gyromean and gyrovariance coincide with the Riemannian mean and variance, *i.e.*, the Fréchet mean and

3. In GyroBN, \odot is not required to satisfy the axioms of a gyrovector space (Theorem 4).

Algorithm 1: Gyrogroup Batch Normalization (GyroBN)

Require : batch of activations $\{x_{1\dots N} \in \mathcal{M}\}$, small positive constant ϵ , and momentum $\eta \in [0, 1]$, running mean μ_r , running variance v_r^2 , bias parameter $\beta \in \mathcal{M}$, scaling parameter $s \in \mathbb{R}$.

Return : normalized batch $\{\tilde{x}_{1\dots N} \in \mathcal{M}\}$

1 **if** *training* **then**

2 | Compute batch mean μ_b and variance v_b^2 of $\{x_{1\dots N}\}$;

3 | Update running statistics $\mu_r = \text{Bar}_\gamma(\mu_b, \mu_r)$, and $v_r^2 = \gamma v_b^2 + (1 - \gamma)v_r^2$;

4 **end**

5 $(\mu, v^2) = (\mu_b, v_b^2)$ **if** *training* **else** (μ_r, v_r^2)

6 $\forall i \leq N, \tilde{x}_i = \beta \oplus \left(\frac{s}{\sqrt{v^2 + \epsilon}} \odot (\ominus \mu \oplus x_i) \right)$

variance under geodesic distance. For completeness, Section B reviews the existence and uniqueness of the Fréchet mean.

Easy computation shows that centering, biasing, and scaling in the Euclidean BN (Equation 12) correspond to gyrosbtraction (Equations 1 and 3), gyroaddition (Equation 1), and scalar gyromultiplication (Equation 2) in \mathbb{R}^n . Motivated by this, we define normalization layer over gyrogroups via gyro operations. Given a batch of activations $\{x_i\}_{i=1}^N \subset \mathcal{M}$, the core operations of GyroBN are

$$\forall i \leq N, \quad \tilde{x}_i \leftarrow \overbrace{\beta \oplus}^{\text{Biasing}} \left(\overbrace{\frac{s}{\sqrt{v^2 + \epsilon}} \odot}^{\text{Scaling}} \left(\overbrace{\ominus \mu \oplus x_i}^{\text{Centering}} \right) \right), \quad (14)$$

where $\mu \in \mathcal{M}$ and v^2 are gyromean and gyrovariance, $\beta \in \mathcal{M}$ is the bias parameter, $s \in \mathbb{R}$ is the scaling parameter, and ϵ is a small value for numerical stability. The following theorem shows that Equation (14) can normalize manifold-valued data.

Theorem 16 (Homogeneity). [↓] *Let (\mathcal{M}, \oplus) be a pseudo-reductive gyrogroup in which every gyration $\text{gyr}[\cdot, \cdot]$ is a gyroisometry. For N samples $\{x_i\}_{i=1}^N \subset \mathcal{M}$, we have*

$$\text{Homogeneity of gyromean: } \text{FM}(\{\beta \oplus x_i\}_{i=1}^N) = \beta \oplus \text{FM}(\{x_i\}_{i=1}^N), \quad \forall \beta \in \mathcal{M}, \quad (15)$$

$$\text{Homogeneity of dispersion from } e: \frac{1}{N} \sum_{i=1}^N d^2(t \odot x_i, e) = \frac{t^2}{N} \sum_{i=1}^N d^2(x_i, e), \quad (16)$$

The most important property of the Euclidean BN (Ioffe and Szegedy, 2015) lies in its ability to normalize the sample mean and variance. Theorem 16 shows that our formulation in Equation (14) enjoys the same property: Equation (15) guarantees that centering and biasing shift the gyromean, while Equation (16) ensures that scaling controls the sample variance. As a result, GyroBN provides a theoretical guarantee of normalization on any pseudo-reductive gyrogroup with isometric gyrations. Moreover, since the gyromean and gyrovariance coincide with their Riemannian counterparts, GyroBN also normalizes Riemannian statistics.

To finalize our GyroBN, we define the running mean updates over gyrogroups as the binary barycenter based on gyrodistance:

$$\text{Bar}_\eta(x_1, x_2) = \operatorname{argmin}_{y \in \mathcal{M}} (\eta d^2(x_1, y) + (1 - \eta) d^2(x_2, y)), \quad \eta \in [0, 1],$$

which can be calculated by the geodesic. With these ingredients, the general framework for GyroBN is presented in Algorithm 1. In particular, it recovers the classic Euclidean BN (Ioffe and Szegedy, 2015) when $\mathcal{M} = \mathbb{R}^n$.

Remark 17. We make the following two remarks w.r.t. left translation.

- *Other Candidates.* There are three alternatives of left gyrotranslation. However, they are not necessarily gyroisometries and therefore are not suitable for building the normalization layer. Specifically, analogous to the left gyrotranslation, the right gyrotranslation is

$$R_x : G \rightarrow G, \quad R_x(y) = y \oplus x, \quad \forall y \in G.$$

Along with the gyroaddition, there is the gyrogroup coaddition (Ungar, 2022, Definition 2.9):

$$x \boxplus y = x \oplus \operatorname{gyr}[x, \ominus y]y, \quad \forall x, y \in G.$$

Coaddition is symmetric to gyroaddition in many ways; for instance, when gyroaddition is gyrocommutative, coaddition is commutative (Ungar, 2022, Theorem 3.3). However, the right gyrotranslation, as well as the left and right translations by coaddition, are not guaranteed to be gyroisometries. Numerical experiments confirm that these three translations on the hyperbolic Poincaré ball fail to preserve gyrodistance (see `gyrocoadd.py`). A theoretical reason is that they all lack a counterpart of the left gyrotranslation law, which is important for the translation to be a gyroisometry (see Figure 3).

- *Special Cases.* For Lie groups with a right-invariant Riemannian metric, right translations are isometries, and GyroBN can then be formulated using them, with Theorem 16 extending directly. In general, however, only left gyrotranslations are guaranteed to be isometries.

5 Instantiations

As indicated by Theorems 14 and 16, our GyroBN can be applied to different geometries with guaranteed normalization of the sample statistics. Once the required operators are specified, Algorithm 1 can be used in a plug-and-play manner. We first show that existing RBN methods with control over sample statistics, such as LieBN on Lie groups and AIM-based SPDBNs, are special cases of our framework. We then instantiate GyroBN on seven representative geometries: the Grassmannian, five constant curvature models (Poincaré ball, projected hypersphere, hyperboloid, sphere, and Beltrami–Klein), and the full-rank correlation manifold. To support these instantiations, we simplify the Grassmannian operators for efficient computation, refine the gyro-structures on the Poincaré ball and projected hypersphere, establish new gyro-structures for the hyperboloid and sphere, characterize the Beltrami–Klein geometry, and formulate a row-wise realization for the correlation manifold.

5.1 LieBN as a Special Case

Chakraborty (2020, Algorithms 3–4) introduced the Riemannian normalization on matrix Lie groups under a specific distance. Chen et al. (2024b) extended this framework to general Lie groups, yielding LieBN, which provides theoretical normalization over the Riemannian mean and variance. This subsection shows that LieBN is a special case of our GyroBN.

LieBN is formulated with a left-invariant metric on a Lie group. Centering and biasing are performed through left group translations, while scaling is defined in the tangent space at the identity element (Chen et al., 2024b, Equations 13–15), which coincides with our gyromultiplication in Equation (2). Since every Lie group is automatically a gyrogroup, gyrotranslation reduces exactly to the group translation. Consequently, the centering, biasing, and scaling in LieBN are identical to those in GyroBN. Moreover, as shown in Theorem 10, the mean, variance, and running mean update defined via the geodesic distance in LieBN are equivalent to their counterparts based on gyrodistance in GyroBN. Therefore, LieBN is a special case of our GyroBN. Chen et al. (2024b) implemented LieBN on three left-invariant metrics of the SPD manifold (AIM⁴, LEM, and LCM) and on a bi-invariant metric over the special orthogonal group. These are therefore incorporated by our GyroBN.

5.2 AIM-Based SPDBNs as Special Cases

Several RBNs on the SPD manifold were developed based on AIM (Brooks et al., 2019; Kobler et al., 2022b,a). The core operations of these approaches can be expressed as

$$\text{Normalization: } \forall i \leq N, \quad \tilde{P}_i \leftarrow B^{\frac{1}{2}} \left(M^{-\frac{1}{2}} P_i M^{-\frac{1}{2}} \right)^{\frac{s}{\sqrt{v^2+\epsilon}}} B^{\frac{1}{2}}, \quad (17)$$

where M and v^2 are the Riemannian mean and variance. The running mean is updated by the binary barycenter under the geodesic distance.

As gyrodistance is identical to the geodesic distance, the gyromean, gyrovariance, and running mean updates are identical to the Riemannian ones. Recalling Table 3, Equation (17) is exactly the specific implementation of Equation (14) under AIM-based gyrogroup on the SPD manifold.⁵ Therefore, the SPDBNs developed by Brooks et al. (2019); Kobler et al. (2022b,a) are also special cases of our GyroBN.

Remark 18. Brooks et al. (2019) only consider centering and biasing. Kobler et al. (2022b) use running mean for centering during the training. Kobler et al. (2022a) use different momentum to update running statistics for training and testing and multi-channel mechanisms for domain adaptation. Nevertheless, all of them are based on Equation (17). Therefore, tricks such as multi-channel and separate momentum can also be applied to our GyroBN. This is what we mean by claiming that our GyroBN incorporates their approaches.

5.3 Grassmannian Manifold

The Grassmannian $\text{Gr}(p, n)$, representing the space of p -dimensional subspaces in \mathbb{R}^n , has been widely applied in machine learning, ranging from action recognition (Huang et al., 2018;

4. AIM is left-invariant with respect to the Lie group operation $P \oplus_{\text{AI}}^{\text{Lie}} Q = LQL^{\top}$, where L is the Cholesky factor of $P = LL^{\top}$ (Thanwerdas and Pennec, 2022). This group structure differs from the one in Table 3.

5. Nguyen (2022b, Lemma 4) show that the AIM gyromultiplication is $t \odot^{\text{AI}} S = S^t, \forall t \in \mathbb{R}, \forall S \in \mathcal{S}_{++}^n$.

Operator	Expression	Operator	Expression
$d(U, V)$	$\ \arccos(\Sigma)\ $ $U^\top V \stackrel{\text{SVD}}{:=} O\Sigma R^\top$	$U \oplus^{\text{Gr}} V$	$\text{mexp}(\Omega)V$
$\text{Log}_U V$	$O \arctan(\Sigma)R^\top$ $(I_n - UU^\top)V(U^\top V)^{-1} \stackrel{\text{SVD}}{:=} O\Sigma R^\top$	Identity	$I_{p,n}$
$\text{Exp}_U \Delta$	$UR \cos(\Sigma)R^\top + O \sin(\Sigma)R^\top$ $\Delta \stackrel{\text{SVD}}{:=} O\Sigma R^\top$	$t \odot^{\text{Gr}} U$	$\text{mexp}(t\Omega)I_{p,n}$
		$\ominus^{\text{Gr}} U$	$\text{mexp}(-\Omega)I_{p,n}$

(a) Riemannian operators
(b) Gyro operators

Table 4: Operators on the ONB Grassmannian.

(Nguyen and Yang, 2023) to question answering (Nguyen and Yang, 2023), shape generation (Yataka et al., 2023), image classification (Wang et al., 2023), and signal analysis (Wang et al., 2024a). We focus on the ONB perspective. Let $U, V \in \text{Gr}(p, n)$, $t \in \mathbb{R}$, and $\Delta \in T_U \text{Gr}(p, n)$. Following the notation in Table 3, Table 4 summarizes the key operators.

Instantiation. Building on Table 4, we now implement the ONB Grassmannian GyroBN. Given a batch of activations $\{U_{1\dots N}\}$, the three core steps of GyroBN are

$$\text{Centering to the identity } I_{p,n}: U_i^1 = \text{mexp}\left(-[\overline{MM^\top}, \tilde{I}_{p,n}]\right) U_i, \quad (18)$$

$$\text{Scaling the dispersion from } I_{p,n}: U_i^2 = \text{mexp}\left(\frac{s}{\sqrt{v^2 + \epsilon}}[\overline{U_i^1(U_i^1)^\top}, \tilde{I}_{p,n}]\right) I_{p,n}, \quad (19)$$

$$\text{Biasing towards } B \in \mathcal{M}: U_i^3 = \text{mexp}\left([\overline{B}, \tilde{I}_{p,n}]\right) U_i^2. \quad (20)$$

Here $\overline{(\cdot)} = \widetilde{\text{Log}}_{\tilde{I}_{p,n}}(\cdot)$ is the Riemannian logarithm under the PP Grassmannian, M (resp. v^2) is the Riemannian batch mean (resp. variance), and $\tilde{I}_{p,n} = I_{p,n}I_{p,n}^\top$ is the PP identity. The mean M can be obtained by the Karcher flow (Karcher, 1977), with the Riemannian logarithm computed by the efficient and stable Algorithm 5.3 of Bendokat et al. (2024).

Efficient Computation. The commutators $[\overline{MM^\top}, \tilde{I}_{p,n}]$ and $[\overline{U_i^1(U_i^1)^\top}, \tilde{I}_{p,n}]$ can be efficiently computed by the following result.

Proposition 19. $\{\downarrow\}$ Given $U = (U_1^\top, U_2^\top)^\top \in \text{Gr}(p, n)$ with $U_1 \in \mathbb{R}^{p \times p}$ and $U_2 \in \mathbb{R}^{(n-p) \times p}$, then

$$[\overline{UU^\top}, \tilde{I}_{p,n}] = \begin{pmatrix} \mathbf{0} & -\tilde{U}_2^\top \\ \tilde{U}_2 & \mathbf{0} \end{pmatrix},$$

where $\tilde{U}_2 = U_2 Q \frac{\arcsin(\hat{S})}{\hat{S}} R^\top$ and $U_1^\top \stackrel{\text{SVD}}{:=} QSR^\top$. Here S is in ascending order, Q and R are flipped column-wise, and $\hat{S} = \sqrt{1 - S^2}$.

Remark 20. Two technical issues are worth noting. (1) *Cut locus:* the logarithm $\text{Log}_U(V)$ exists only when U and V are not in each other's cut locus (Bendokat et al., 2024). Similarly, gyroaddition and gyromultiplication are not globally defined due to the cut locus (Nguyen, 2022a, Section 3.2). However, Algorithm 5.3 of Bendokat et al. (2024) provides a numerical

Operator	Expression	Operator	Expression
$d(x, y)$	$\frac{2}{\sqrt{ K }} \tanh_K^{-1}(\sqrt{ K } \ -x \oplus_K y \)$	$x \oplus_K y$	$\frac{(1 - 2K \langle x, y \rangle - K \ y\ ^2)x + (1 + K \ x\ ^2)y}{1 - 2K \langle x, y \rangle + K^2 \ x\ ^2 \ y\ ^2}$
$\text{Log}_x y$	$\frac{2}{\sqrt{ K } \lambda_x^K} \tanh_K^{-1}(\sqrt{ K } \ -x \oplus_K y \) \frac{-x \oplus_K y}{\ -x \oplus_K y \ }$	Identity	$\mathbf{0}$
$\text{Exp}_x v$	$x \oplus_K \left(\tanh_K \left(\sqrt{ K } \frac{\lambda_x^K \ v\ }{2} \right) \frac{v}{\sqrt{ K } \ v\ } \right)$	$t \odot_K x$	$\frac{\tanh_K \left(t \tanh_K^{-1}(\sqrt{ K } \ x\) \right)}{\sqrt{ K }} \frac{x}{\ x\ }$
$\text{PT}_{x \rightarrow y}(v)$	$\frac{\lambda_x^K}{\lambda_y^K} \text{gyr}[y, -x]v$	$\ominus_K x$	$-x$

(a) Riemannian operators
(b) Gyro operators

Table 5: Operators on the stereographic model.

remedy. (2) *PP Grassmannian*: although our derivation is based on the ONB Grassmannian, GyroBN under the PP Grassmannian can be obtained by mapping data via $\pi^{-1} : \widetilde{\text{Gr}}(p, n) \rightarrow \text{Gr}(p, n)$, normalizing, and mapping back via π . Details are deferred to Section C.

5.4 Stereographic Model

The stereographic model has shown success in different applications, including computer vision (Van Spengler et al., 2023), natural language processing (Ganea et al., 2018; Shimizu et al., 2021), graph learning (Bachmann et al., 2020; Grover et al., 2025a,b), and astronomy (Chen et al., 2025a). We begin by analyzing its gyro-structure and then instantiate GyroBN.

5.4.1 STEREOGRAPHIC GYROVECTOR SPACE

As introduced in Section 2.4, the stereographic model \mathfrak{st}_K^n unifies constant curvature geometries: the hyperbolic Poincaré ball \mathbb{P}_K^n for $K < 0$, Euclidean space \mathbb{R}^n for $K = 0$, and the spherical projected hypersphere \mathbb{D}_K^n for $K > 0$. For $x, y, z \in \mathfrak{st}_K^n$, $t \in \mathbb{R}$, and $v \in T_x \mathfrak{st}_K^n$, its Riemannian and gyro operators are summarized in Table 5, where $\tan_K = \tanh$ if $K < 0$ and $\tan_K = \tan$ if $K > 0$. The gyration is given by Bachmann et al. (2020, Appendix C.2.6):

$$\text{gyr}[x, y]z = z + 2 \frac{Ax + By}{D}, \quad (21)$$

with

$$\begin{aligned} A &= -K^2 \langle x, z \rangle \|y\|^2 - K \langle y, z \rangle + 2K^2 \langle x, y \rangle \langle y, z \rangle, \\ B &= -K^2 \langle y, z \rangle \|x\|^2 + K \langle x, z \rangle, \\ D &= 1 - 2K \langle x, y \rangle + K^2 \|x\|^2 \|y\|^2 > (1 - K \langle x, y \rangle)^2 > 0. \end{aligned}$$

For $K < 0$, the Poincaré ball $(\mathbb{P}_K^n, \oplus_K, \odot_K)$ forms a Möbius gyrovector space (Ungar, 2022, Theorem 6.85). For $K > 0$, however, the situation is subtler (Bachmann et al., 2020):

- gyroaddition is definite except $x = \frac{y}{K \|y\|^2} = \mathbf{0}$;
- gyromultiplication is definite except $r \tan^{-1}(\sqrt{K} \|x\|) = \pi/2 + k\pi$ for some $k \in \mathbb{Z}$.

Even if assumed well-defined, it remains unclear whether $(\mathfrak{st}_K^n, \oplus_K, \odot_K)$ with $K > 0$ satisfies the axioms of a gyrovector space, in contrast to the Poincaré ball. Closing this gap is part of

our contribution: under the assumption of well-definedness, we show that the stereographic gyro operations coincide with those in Equations (1) and (2) and prove that the stereographic model satisfies all axioms of a gyrovector space.

Proposition 21. $\lfloor \downarrow \rfloor$ *The stereographic gyroaddition and gyromultiplication coincide with the Riemannian definitions:*

$$x \oplus_K y = \text{Exp}_x(\text{PT}_{\mathbf{0} \rightarrow x}(\text{Log}_{\mathbf{0}}(y))), \quad \forall x, y \in \mathfrak{st}_K^n, \quad (22)$$

$$t \odot_K x = \text{Exp}_{\mathbf{0}}(t \text{Log}_{\mathbf{0}}(x)), \quad \forall t \in \mathbb{R}, x \in \mathfrak{st}_K^n. \quad (23)$$

Theorem 22. $\lfloor \downarrow \rfloor$ *For any $K \in \mathbb{R}$, the stereographic model $(\mathfrak{st}_K^n, \oplus_K)$ satisfies all axioms of a gyrocommutative gyrogroup. When further endowed with gyromultiplication \odot_K , it satisfies all axioms of a gyrovector space.*

5.4.2 STEREOGRAPHIC GYROBN

Next, we extend Theorem 14 to the stereographic model with arbitrary curvature.

Theorem 23. $\lfloor \downarrow \rfloor$ *For the stereographic model, the gyrodistance coincides with the geodesic distance. Moreover, the gyroinverse, any gyration, and any left gyrotranslation are gyroisometries.*

Combining Theorem 16 and Theorem 23, GyroBN in the stereographic model is theoretically guaranteed to normalize sample statistics. Practically, implementation only requires substituting the operators in Table 5 into Algorithm 1. For efficient computation, the Poincaré Fréchet mean can be obtained using the algorithm of Lou et al. (2020, Algorithm 1), while the mean on the sphere is computed via the Karcher flow (Karcher, 1977).

5.5 Radius Model

As introduced in Section 2.4, the radius model \mathcal{M}_K^n is another representation of constant-curvature spaces, unifying the hyperboloid \mathbb{H}_K^n for $K < 0$, the sphere \mathbb{S}_K^n for $K > 0$, and the Euclidean space \mathbb{R}^n for $K = 0$. Although this model has been effective in various applications (Chami et al., 2019; Chen et al., 2021; Bdeir et al., 2024; Pal et al., 2024; He et al., 2025; Khan et al., 2025), its gyro-structure has not been formalized. We first analyze the gyro-structure on \mathcal{M}_K^n and then instantiate GyroBN.

5.5.1 RADIUS GYROVECTOR SPACE

The radius model \mathcal{M}_K^n is isometric to the stereographic model \mathfrak{st}_K^n via stereographic projection fixing the south pole (Skopek et al., 2020):

$$\pi_{\mathcal{M}_K^n \rightarrow \mathfrak{st}_K^n} : \mathcal{M}_K^n \ni \begin{bmatrix} \xi \in \mathbb{R} \\ x \in \mathbb{R}^n \end{bmatrix} \mapsto \frac{x}{1 + \sqrt{|K|}\xi} \in \mathfrak{st}_K^n, \quad (24)$$

$$\pi_{\mathfrak{st}_K^n \rightarrow \mathcal{M}_K^n} : \mathfrak{st}_K^n \ni y \mapsto \begin{bmatrix} \frac{1}{\sqrt{|K|}} \frac{1-K\|y\|^2}{1+K\|y\|^2} \\ \frac{2y}{1+K\|y\|^2} \end{bmatrix} \in \mathcal{M}_K^n. \quad (25)$$

The origin in \mathcal{M}_K^n is defined as $\bar{\mathbf{0}} = [\sqrt{1/|K|}, 0, \dots, 0]^\top$, corresponding to $\mathbf{0} \in \mathfrak{st}_K^n$. For $K > 0$, we have $\mathcal{M}_K^n = \mathbb{S}_K^n$ and $\mathfrak{st}_K^n = \mathbb{D}_K^n$. Since Equation (24) is undefined at the south

Operator	Expression	Operator	Expression
$d(x, y)$	$\frac{1}{\sqrt{ K }} \cos_K^{-1}(\beta)$ $\beta = K \langle x, y \rangle_K$	$d(\bar{\mathbf{0}}, x)$	$\frac{1}{\sqrt{ K }} \cos_K^{-1}(\sqrt{ K } x_t)$
$\text{Log}_x y$	$\frac{\cos_K^{-1}(\beta)}{\sqrt{\text{sign}(K)(1-\beta^2)}} (y - \beta x)$ $\beta = K \langle x, y \rangle_K$	$\text{Log}_{\bar{\mathbf{0}}}(x)$	$\begin{bmatrix} 0 \\ \frac{\cos_K^{-1}(\sqrt{ K } x_t)}{\sqrt{ K } \ x_s\ } x_s \end{bmatrix}$
$\text{Exp}_x v$	$\cos_K(\alpha) x + \frac{\sin_K(\alpha)}{\alpha} v$ $\alpha = \sqrt{ K } \ v\ _K$	$\text{Exp}_{\bar{\mathbf{0}}}(v)$	$\frac{1}{\sqrt{ K }} \begin{bmatrix} \cos_K(\sqrt{ K } \ v_s\) \\ \frac{\sin_K(\sqrt{ K } \ v_s\)}{\ v_s\ } v_s \end{bmatrix}$
$\text{PT}_{x \rightarrow y}(v)$	$v - \frac{K \langle y, v \rangle_K}{1 + K \langle x, y \rangle_K} (x + y)$	$\text{PT}_{\bar{\mathbf{0}} \rightarrow x}(v)$	$v - \frac{K \langle x_s, v_s \rangle}{1 + \sqrt{ K } x_t} \begin{bmatrix} x_t + 1/\sqrt{ K } \\ x_s \end{bmatrix}$

(a) General form
(b) At the origin $\bar{\mathbf{0}}$

Table 6: Riemannian operators on the radius model.

pole $-\bar{\mathbf{0}}$ when $K > 0$, we use the one-point compactification $\mathbb{D}_K^n \cup \{\infty\}$ with the identification $\pi_{\mathcal{M}_K^n \rightarrow \text{st}_K^n}(-\bar{\mathbf{0}}) = \infty$ (Skopek et al., 2020, Remark A.9). For simplicity, we use \mathbb{D}_K^n and $\mathbb{D}_K^n \cup \{\infty\}$ interchangeably.

Table 6 lists the Riemannian operators (Skopek et al., 2020, Table 1), together with the simplified expressions at $\bar{\mathbf{0}}$. We adopt the following curvature-aware functions:

$$\sin_K = \begin{cases} \sin & \text{if } K > 0 \\ \sinh & \text{if } K < 0 \end{cases} \quad \cos_K = \begin{cases} \cos & \text{if } K > 0 \\ \cosh & \text{if } K < 0 \end{cases} \quad \langle \cdot, \cdot \rangle_K = \begin{cases} \langle \cdot, \cdot \rangle & \text{if } K > 0 \\ \langle \cdot, \cdot \rangle_{\mathcal{L}} & \text{if } K < 0 \end{cases}$$

Besides, $\|\cdot\|_K$ is the norm induced by $\langle \cdot, \cdot \rangle_K$, $(\cdot)_s$ denotes the space vector, and $(\cdot)_t$ denotes the time scalar.

By Table 6, we define the gyroaddition and gyromultiplication as Equations (1) and (2):

$$x \oplus_K^{\mathcal{M}} y = \text{Exp}_x(\text{PT}_{\bar{\mathbf{0}} \rightarrow x}(\text{Log}_{\bar{\mathbf{0}}}(y))), \quad \forall x, y \in \mathcal{M}_K^n, \quad (26)$$

$$t \odot_K^{\mathcal{M}} x = \text{Exp}_{\bar{\mathbf{0}}}(t \text{Log}_{\bar{\mathbf{0}}}(x)), \quad \forall t \in \mathbb{R}, \forall x \in \mathcal{M}_K^n. \quad (27)$$

We give the following clarifications regarding the above two gyro operations.

- For hyperbolic geometry ($K < 0$), Equation (26) has been employed in prior work (Chami et al., 2019; He et al., 2025). However, there exists no closed-form expression, which could be more efficient than the composition of Riemannian operators. Besides, the underlying gyro-structure has not been formally discussed.
- For spherical geometry ($K > 0$), the geodesic between antipodal points (x and $-x$) is not unique, making the logarithm and parallel transport along such a geodesic ill-defined. For the sphere, Equation (26) assumes that $x \neq -\bar{\mathbf{0}}$ and $y \neq -\bar{\mathbf{0}}$, while Equation (27) assumes that $x \neq -\bar{\mathbf{0}}$. Like before, we always make these assumptions implicitly.

In the following, we first give the closed-form expressions of Equations (26) and (27). Then, we show that Equations (26) and (27) conform with all the axioms of a gyrovector space.

Proposition 24 (Gyromultiplication and Gyroinverse). $\llbracket \downarrow \rrbracket$ Let $x = [x_t, x_s^\top]^\top$ be a point in \mathcal{M}_K^n , where $x_t \in \mathbb{R}$ is the time scalar, and $x_s \in \mathbb{R}^n$ is the spatial part. The gyromultiplication and inverse have closed-form expressions:

$$t \odot_K^{\mathcal{M}} x = \begin{cases} \bar{\mathbf{0}}, & t = 0 \vee x = \bar{\mathbf{0}}, \\ \frac{1}{\sqrt{|K|}} \begin{bmatrix} \cos_K \left(t \cos_K^{-1}(\sqrt{|K|} x_t) \right) \\ \frac{\sin_K \left(t \cos_K^{-1}(\sqrt{|K|} x_t) \right)}{\|x_s\|} x_s \end{bmatrix}, & t \neq 0, \end{cases} \quad (28)$$

$$\ominus_K^{\mathcal{M}} x = -1 \odot_K^{\mathcal{M}} x = \begin{bmatrix} x_t \\ -x_s \end{bmatrix}. \quad (29)$$

In particular, the gyro identity is $\bar{\mathbf{0}}$. Besides, the following shows that the sphere gyromultiplication is still valid for the singular cases in the projected hypersphere. Assume $K > 0$ and $x \neq \pm \bar{\mathbf{0}}$, and let $\mathfrak{st}_K^n \ni u = \pi_{\mathcal{M}_K^n \rightarrow \mathfrak{st}_K^n}(x)$ be its stereographic image. For $t \in \mathbb{R}$, set $\theta = \cos^{-1}(\sqrt{K} x_t) \in (0, \pi)$. Then the following are equivalent:

$$(i) \ t \tan^{-1}(\sqrt{K} \|u\|) = \frac{\pi}{2} + k\pi \iff (ii) \ t\theta = (2k+1)\pi, \quad k \in \mathbb{Z}.$$

In these singular cases, Equation (28) is still valid, while the stereographic gyromultiplication returns infinity:

$$t \odot_K^{\mathcal{M}} x = -\bar{\mathbf{0}} \in \mathcal{M}_K^n, \quad t \odot_K u = \infty \in \mathfrak{st}_K^n, \quad (30)$$

where ∞ denotes the added point in the one-point compactification $\mathbb{D}_K^n \cup \{\infty\}$ ($\mathfrak{st}_K^n = \mathbb{D}_K^n$ for $K > 0$) and $\pi_{\mathcal{M}_K^n \rightarrow \mathfrak{st}_K^n}(-\bar{\mathbf{0}}) = \infty$.

Proposition 25 (Gyroaddition). $\llbracket \downarrow \rrbracket$ Let $x = [x_t, x_s^\top]^\top$ and $y = [y_t, y_s^\top]^\top$ be points in \mathcal{M}_K^n , where $x_t, y_t \in \mathbb{R}$ are the time scalars, and $x_s, y_s \in \mathbb{R}^n$ are the spatial parts. Then, the gyroaddition on \mathcal{M}_K^n admits the closed form:

$$x \oplus_K^{\mathcal{M}} y = \begin{cases} x, & y = \bar{\mathbf{0}}, \\ y, & x = \bar{\mathbf{0}}, \\ \begin{bmatrix} \frac{1}{\sqrt{|K|}} \frac{D-KN}{D+KN} \\ \frac{2(A_s x_s + A_y y_s)}{D+KN} \end{bmatrix}, & \text{Others.} \end{cases} \quad (31)$$

Here, $A_s = ab^2 - 2Kbs_{xy} - Kan_y$ and $A_y = b(a^2 + Kn_x)$ with the following notations:

$$a = 1 + \sqrt{|K|} x_t, \quad b = 1 + \sqrt{|K|} y_t, \quad n_x = \|x_s\|^2, \quad n_y = \|y_s\|^2, \quad s_{xy} = \langle x_s, y_s \rangle.$$

$$D = a^2 b^2 - 2Kabs_{xy} + K^2 n_x n_y, \quad N = a^2 n_y + 2abs_{xy} + b^2 n_x.$$

Besides, the following shows that the sphere gyroaddition is still valid under the singular cases in the projected hypersphere. Assume $K > 0$ and $x, y \neq \pm \bar{\mathbf{0}}$, and let $u = \pi_{\mathcal{M}_K^n \rightarrow \mathfrak{st}_K^n}(x)$ and $v = \pi_{\mathcal{M}_K^n \rightarrow \mathfrak{st}_K^n}(y)$ be the stereographic images. The following statements are equivalent:

1. $u = \frac{v}{K \|v\|^2}$ ($v \neq \mathbf{0}$);
2. $x_s = y_s$ and $x_t = -y_t$ (same meridian, mirrored across the equator);
3. $D = 0$.

In such singular cases, we have $N > 0$ and Equation (31) is still valid, while the stereographic gyroaddition returns infinity:

$$x \oplus_K^{\mathcal{M}} y = -\bar{\mathbf{0}}, \quad u \oplus_K v = \infty,$$

where ∞ is the point added in the one-point compactification of \mathbb{D}_K^n .

The above two propositions immediately imply that $\pi_{\mathcal{M}_K^n \rightarrow \text{st}_K^n}$ preserves the gyro operations.

Corollary 26 (Isomorphism). \lrcorner For the hyperbolic geometry ($K < 0$), the isometry $\pi_{\mathcal{M}_K^n \rightarrow \text{st}_K^n} : \mathbb{H}_K^n \rightarrow \mathbb{P}_K^n$ preserves the gyro operations:

$$\begin{aligned} x \oplus_K^{\mathcal{M}} y &= \pi_{\text{st}_K^n \rightarrow \mathcal{M}_K^n} \left(\pi_{\mathcal{M}_K^n \rightarrow \text{st}_K^n}(x) \oplus_K \pi_{\mathcal{M}_K^n \rightarrow \text{st}_K^n}(y) \right), \quad \forall x, y \in \mathcal{M}_K^n, \\ r \odot_K^{\mathcal{M}} y &= \pi_{\text{st}_K^n \rightarrow \mathcal{M}_K^n} \left(r \odot_K \pi_{\mathcal{M}_K^n \rightarrow \text{st}_K^n}(y) \right), \quad \forall r \in \mathbb{R}, \forall x \in \mathcal{M}_K^n. \end{aligned} \quad (32)$$

For the spherical geometry ($K > 0$), the isometry $\pi_{\mathcal{M}_K^n \rightarrow \text{st}_K^n} : \mathbb{S}_K^n \rightarrow \mathbb{D}_K^n \cup \{\infty\}$ preserves the gyro operations:

$$\begin{aligned} x \oplus_K^{\mathcal{M}} y &= \pi_{\text{st}_K^n \rightarrow \mathcal{M}_K^n} \left(\pi_{\mathcal{M}_K^n \rightarrow \text{st}_K^n}(x) \oplus_K \pi_{\mathcal{M}_K^n \rightarrow \text{st}_K^n}(y) \right), \quad \forall x, y \in \mathcal{M}_K^n / \{-\bar{\mathbf{0}}\}, \\ r \odot_K^{\mathcal{M}} y &= \pi_{\text{st}_K^n \rightarrow \mathcal{M}_K^n} \left(r \odot_K \pi_{\mathcal{M}_K^n \rightarrow \text{st}_K^n}(y) \right), \quad \forall r \in \mathbb{R}, \forall x \in \mathcal{M}_K^n / \{-\bar{\mathbf{0}}\}. \end{aligned} \quad (33)$$

Remark 27. We provide two clarifications regarding Theorem 26.

- *Compactified projected hypersphere.* Although stereographic operations for $K > 0$ may be undefined in certain cases, they become well-defined on the one-point compactification $\mathbb{D}_K^n \cup \{\infty\}$, where undefined cases corresponds to ∞ .
- *Sphere vs. Projected Hypersphere.* Theorem 26 suggests a numerical advantage of the sphere: gyro-operations are well-defined on \mathbb{S}_K^n at all points except the single south pole $-\bar{\mathbf{0}}$, including cases corresponding to singularities on the projected hypersphere. This broader domain can make computations on \mathbb{S}_K^n more stable.

From the above corollary, it is expected that the operations $\oplus_K^{\mathcal{M}}$ and $\odot_K^{\mathcal{M}}$ also satisfy the axioms of a gyrovector space for both negative and positive curvature K .

Theorem 28 (Radius Gyrovector Spaces). \lrcorner $(\mathcal{M}_K^n, \oplus_K^{\mathcal{M}})$ forms a gyrocommutative gyrogroup, and $(\mathcal{M}_K^n, \oplus_K^{\mathcal{M}}, \odot_K^{\mathcal{M}})$ forms a gyrovector space.⁶

Due to the isometry, Theorem 11 implies gyroisometries over \mathcal{M}_K^n .

Theorem 29. *On the radius model, the gyrodistance is identical to the geodesic distance, whereas the gyroinverse, gyration, and left gyrotranslation are gyroisometries.*

6. For $K > 0$, we implicitly assume the addition and multiplication are well-defined; whenever they are, all corresponding axioms hold.

5.5.2 RADIUS GYROBN

Theorem 29 guarantees that GyroBN on the radius model normalizes the sample mean and variance. Substituting the operators from Table 6 and Theorems 24 and 25 into Algorithm 1 can directly yield the radius GyroBN. For $K < 0$ (hyperboloid), the Fréchet mean can be computed efficiently by Algorithm 3 of Lou et al. (2020); for $K > 0$ (projected hypersphere), we compute the Fréchet mean using the Karcher flow (Karcher, 1977).

5.6 Hyperbolic Beltrami–Klein

The Beltrami–Klein model has recently emerged as a promising alternative to the Poincaré ball for representing hyperbolic geometry (Mao et al., 2024). As the Poincaré ball admits the Möbius gyrovector space, the Beltrami–Klein model admits the Einstein gyrovector space (Ungar, 2022, Chapter 6.18). While prior studies mainly focused on the case $K = -1$ (Mao et al., 2024), we study the Einstein gyrospace and the Beltrami–Klein geometry under arbitrary negative curvature. This allows us to establish the equivalence between their gyro and Riemannian formulations and, ultimately, to instantiate GyroBN on this model.

5.6.1 EINSTEIN GYROVECTOR SPACE AND BELTRAMI–KLEIN GEOMETRY

For $x, y, z \in \mathbb{K}_K^n$ and $t \in \mathbb{R}$, the Einstein gyro operations are given by

$$x \oplus_E y = \frac{1}{1 - K \langle x, y \rangle} \left(x + \frac{1}{\gamma_x} y - K \frac{\gamma_x}{1 + \gamma_x} \langle x, y \rangle x \right), \quad (34)$$

$$t \odot_E x = \frac{\tanh(t \tanh^{-1}(\sqrt{-K} \|x\|))}{\sqrt{-K}} \frac{x}{\|x\|}, \quad (35)$$

$$\text{gyr}[x, y]z = z + \frac{Ax + By}{D}, \quad (36)$$

where $\gamma_x^K = \frac{1}{\sqrt{1+K\|x\|^2}}$ is the gamma factor, and

$$\begin{aligned} A &= K \frac{\gamma_x^2}{(\gamma_x + 1)} (\gamma_y - 1) (\langle x, z \rangle) - K \gamma_x \gamma_y (\langle y, z \rangle) \\ &\quad + 2K^2 \frac{\gamma_x^2 \gamma_y^2}{(\gamma_x + 1)(\gamma_y + 1)} (\langle x, y \rangle) (\langle y, z \rangle), \\ B &= K \frac{\gamma_y}{\gamma_y + 1} \{ \gamma_x (\gamma_y + 1) (\langle x, z \rangle) + (\gamma_x - 1) \gamma_y (\langle y, z \rangle) \}, \\ D &= 1 + \gamma_x \gamma_y (1 - K \langle x, y \rangle) = 1 + \gamma_{x \oplus_E y} > 1. \end{aligned} \quad (37)$$

Note that the Einstein gyromultiplication coincides with the Möbius gyromultiplication.

For the Poincaré ball, Möbius operations are equivalent to those defined by Equations (1) and (2) (Ganea et al., 2018, Section 2.4). Similarly, under $K = -1$, the Einstein operations coincide with Equations (1) and (2) (Mao et al., 2024, Section 4.2). We extend these results to arbitrary $K < 0$ and further show that the Beltrami–Klein Riemannian operators can be equivalently expressed in terms of the Einstein gyrospace. To this end, we first establish the isometry between the Beltrami–Klein and Poincaré models.

Proposition 30 (Beltrami–Klein Isometries). [\Downarrow] *The following maps are Riemannian isometries between the Beltrami–Klein and Poincaré ball models:*

$$\begin{aligned}\pi_{\mathbb{K}_K^n \rightarrow \mathbb{P}_K^n} : \mathbb{K}_K^n \ni x &\longmapsto \frac{1}{1 + \sqrt{1 + K \|x\|^2}} x \in \mathbb{P}_K^n, \\ \pi_{\mathbb{P}_K^n \rightarrow \mathbb{K}_K^n} : \mathbb{P}_K^n \ni x &\longmapsto \frac{2}{1 - K \|x\|^2} x \in \mathbb{K}_K^n.\end{aligned}$$

Particularly, $\pi_{\mathbb{P}_K^n \rightarrow \mathbb{K}_K^n}(\mathbf{0}) = \mathbf{0}$. Given x in the hyperbolic model $\mathcal{H} \in \{\mathbb{K}_K^n, \mathbb{P}_K^n\}$ and tangent vector $v \in T_x \mathcal{H}$, the differential maps of $\pi_{\mathbb{K}_K^n \rightarrow \mathbb{P}_K^n}$ and $\pi_{\mathbb{P}_K^n \rightarrow \mathbb{K}_K^n}$ are

$$\begin{aligned}(\pi_{\mathbb{K}_K^n \rightarrow \mathbb{P}_K^n})_{*,x}(v) &= \frac{1}{1 + \sqrt{1 + K \|x\|^2}} v - \frac{K \langle x, v \rangle}{\left(1 + \sqrt{1 + K \|x\|^2}\right)^2 \sqrt{1 + K \|x\|^2}} x, \\ (\pi_{\mathbb{P}_K^n \rightarrow \mathbb{K}_K^n})_{*,x}(v) &= \frac{2}{\left(1 - K \|x\|^2\right)} v + \frac{4K \langle x, v \rangle}{\left(1 - K \|x\|^2\right)^2} x.\end{aligned}$$

Especially, the differential maps at the zero vector are

$$(\pi_{\mathbb{K}_K^n \rightarrow \mathbb{P}_K^n})_{*,\mathbf{0}}(v) = \frac{1}{2} v, \quad (38)$$

$$(\pi_{\mathbb{P}_K^n \rightarrow \mathbb{K}_K^n})_{*,\mathbf{0}}(v) = 2v. \quad (39)$$

Moreover, these isometries preserve gyroaddition and gyromultiplication:

$$\begin{aligned}\pi_{\mathbb{K}_K^n \rightarrow \mathbb{P}_K^n}(x \oplus_M y) &= \pi_{\mathbb{K}_K^n \rightarrow \mathbb{P}_K^n}(x) \oplus_E \pi_{\mathbb{K}_K^n \rightarrow \mathbb{P}_K^n}(y), \quad \forall x, y \in \mathbb{P}_K^n, \\ \pi_{\mathbb{P}_K^n \rightarrow \mathbb{K}_K^n}(t \odot_M x) &= t \odot_E \pi_{\mathbb{P}_K^n \rightarrow \mathbb{K}_K^n}(x), \quad \forall t \in \mathbb{R}, \forall x \in \mathbb{P}_K^n,\end{aligned} \quad (40)$$

where \oplus_M and \odot_M are Möbius operations, while \oplus_E and \odot_E are the Einstein counterparts.

Theorem 31 (Einstein by Beltrami–Klein). [\Downarrow] *The Einstein gyro operations can be rewritten as Equations (1) and (2):*

$$\begin{aligned}x \oplus_E y &= \text{Exp}_x(\text{PT}_{\mathbf{0} \rightarrow x}(\text{Log}_{\mathbf{0}}(y))), \quad \forall x, y \in \mathbb{K}_K^n, \\ t \odot_E x &= \text{Exp}_{\mathbf{0}}(t \text{Log}_{\mathbf{0}}(x)), \quad \forall x \in \mathbb{K}_K^n, \forall t \in \mathbb{R}.\end{aligned}$$

Theorem 31 demonstrates that the Einstein gyro-structure can be expressed by the Beltrami–Klein geometry. Conversely, the Beltrami–Klein geometry can also be formulated by the Einstein gyro-structure.

Theorem 32 (Beltrami–Klein by Einstein). [\Downarrow] *Given $x, y \in \mathbb{K}_K^n$ and $v \in T_x \mathbb{K}_K^n$, the distance, exponential, and logarithmic operators under the Beltrami–Klein geometry are*

$$d(x, y) = \frac{2}{\sqrt{|K|}} \tanh^{-1} \left(\sqrt{|K|} \frac{\|-x \oplus_E y\|}{1 + \sqrt{1 + K \|-x \oplus_E y\|^2}} \right), \quad (41)$$

$$\text{Exp}_x(v) = x \oplus_{\mathbb{E}} \text{Exp}_{\mathbf{0}} \left(\frac{1}{\sqrt{1 + K \|x\|^2}} v - \frac{K \langle x, v \rangle}{\left(1 + \sqrt{1 + K \|x\|^2}\right) (1 + K \|x\|^2)} x \right), \quad (42)$$

$$\text{Log}_x(y) = \frac{1}{\lambda_{\tilde{x}}^K} (\pi_{\mathbb{P}_K^n \rightarrow \mathbb{K}_K^n})_{*, \tilde{x}} (\text{Log}_{\mathbf{0}}(-x \oplus_{\mathbb{E}} y)), \quad (43)$$

where $\tilde{x} = \pi_{\mathbb{K}_K^n \rightarrow \mathbb{P}_K^n}(x)$. Particularly, the exponential and logarithmic maps at the zero vector $\mathbf{0}$ are identical across the Beltrami–Klein and Poincaré ball models:

$$\text{Exp}_{\mathbf{0}}(v) = \tanh(\sqrt{|K|} \|v\|) \frac{v}{\sqrt{|K|} \|v\|}, \quad \forall v \in T_{\mathbf{0}}\mathcal{H}, \quad (44)$$

$$\text{Log}_{\mathbf{0}}(x) = \tanh^{-1}(\sqrt{|K|} \|x\|) \frac{x}{\sqrt{|K|} \|x\|}, \quad \forall x \in \mathcal{H}, \quad (45)$$

with $\mathcal{H} \in \{\mathbb{K}_K^n, \mathbb{P}_K^n\}$.

Remark 33. Since the Beltrami–Klein and Poincaré ball models share the same $\text{Exp}_{\mathbf{0}}$ and $\text{Log}_{\mathbf{0}}$, it naturally follows that the Einstein and Möbius gyromultiplication coincide.

As the Beltrami–Klein is isometric to the Poincaré ball, Theorem 11 implies gyroisometries.

Theorem 34. *On the Beltrami–Klein model, the gyrodistance is identical to the geodesic distance, whereas the gyroinverse, gyration, and left gyrotranslation are gyroisometries.*

5.6.2 BELTRAMI–KLEIN GYROBN

Theorem 34 ensures that GyroBN on the Beltrami–Klein model normalizes the sample mean and variance. Owing to the isometry between the Beltrami–Klein and Poincaré models, the Fréchet mean can be computed via the Poincaré ball: map the data to the Poincaré model using $\pi_{\mathbb{K}_K^n \rightarrow \mathbb{P}_K^n}$, compute the Poincaré Fréchet mean (Lou et al., 2020, Algorithm 1), and map the result back using $\pi_{\mathbb{P}_K^n \rightarrow \mathbb{K}_K^n}$. Together with the gyro and Riemannian operators in Section 5.6.1, we have all the ingredients to implement Algorithm 1.

5.7 Correlation Manifolds

Thanwerdas and Pennek (2022, Section 4.1) show that any correlation matrix can be identified with a product of hyperbolic spaces via its Cholesky decomposition. Given $C \in \text{Cor}^+(n)$, let $L = \text{Chol}(C)$ be its Cholesky factor. The k -th row of L has the form $(L_{k1}, \dots, L_{k,k-1}, L_{kk}, 0, \dots, 0)$ with $L_{kk} > 0$, which belongs to the hyperbolic open hemisphere⁷ $\text{HS}^{k-1} = \{x \in \mathbb{R}^k \mid \|x\| = 1, x_k > 0\}$. As shown by Chen et al. (2025d), HS^n is isometric to the unit Poincaré ball $\mathbb{P}_{-1}^n = \{x \in \mathbb{R}^n \mid \|x\| < 1\}$ by

$$\pi_{\text{HS}^n \rightarrow \mathbb{P}_{-1}^n} \left(\begin{bmatrix} x \\ x_{n+1} \end{bmatrix} \right) = \frac{x}{1 + x_{n+1}}.$$

7. Also known as the Jemisphere model, where the “J” is pronounced as in Spanish (Cannon et al., 1997, Section 7).

$U \oplus^{\text{Gr}} V$	$\ominus^{\text{Gr}} U$	$t \odot^{\text{Gr}} U$	Fréchet mean
$\text{mexp}(\Omega)V$	$\text{mexp}(-\Omega)I_{p,n}$	$\text{mexp}(t\Omega)I_{p,n}$	Karcher flow

(a) The ONB Grassmannian

Operator	st_K^n	\mathcal{M}_K^n	\mathbb{K}_K^n
$x \oplus y$	$\frac{(1 - 2K\langle x, y \rangle - K\ y\ ^2)x + (1 + K\ x\ ^2)y}{1 - 2K\langle x, y \rangle + K^2\ x\ ^2\ y\ ^2}$	Equation (31)	$\frac{1}{1 - K\langle x, y \rangle} \left(x + \frac{1}{\gamma_x} y - K \frac{\gamma_x}{1 + \gamma_x} \langle x, y \rangle x \right)$
$\ominus x$	$-x$	$\begin{bmatrix} x_t \\ -x_s \end{bmatrix}$	$-x$
$t \odot x$	$\frac{\tanh(t \tanh^{-1}(\sqrt{-K}\ x\))}{\sqrt{-K}} \frac{x}{\ x\ }$	Equation (28)	$\frac{\tanh(t \tanh^{-1}(\sqrt{-K}\ x\))}{\sqrt{-K}} \frac{x}{\ x\ }$
Fréchet mean	$K < 0$: Algorithm 1 (Lou et al., 2020) $K > 0$: Karcher flow	$K < 0$: Algorithm 3 (Lou et al., 2020) $K > 0$: Karcher flow	Via Poincaré ball (see Section 5.6.2)

(b) Constant curvature spaces

Table 7: Summary of operators for GyroBN across representative manifolds.

Therefore, each correlation matrix can be identified with $n - 1$ Poincaré vectors (Chen et al., 2025d):

$$\text{Cor}^+(n) \ni C \mapsto \begin{bmatrix} 1 & 0 & \cdots & 0 \\ L_{21} & L_{22} & \cdots & 0 \\ \vdots & \vdots & \ddots & \vdots \\ L_{n1} & L_{n2} & \cdots & L_{nn} \end{bmatrix} \mapsto \begin{bmatrix} x_1 \in \mathbb{P}_{-1}^1 \\ \vdots \\ x_{n-1} \in \mathbb{P}_{-1}^{n-1} \end{bmatrix}. \quad (46)$$

where $x_i = \pi_{\text{HS}^i \rightarrow \mathbb{P}_{-1}^i} (L_{(i+1,1)}, \dots, L_{(i+1,i+1)})^\top$ corresponds to the $(i + 1)$ -th row of the Cholesky factor. Let $\mathbb{P}^{n-1} = \prod_{i=1}^{n-1} \mathbb{P}_{-1}^i$ denote the product of unit Poincaré balls. We denote the identification in Equation (46) by $\Phi : \text{Cor}^+(n) \rightarrow \mathbb{P}^{n-1}$. GyroBN on the correlation manifold can then be realized via the Poincaré GyroBN applied row-wise: first map C to \mathbb{P}^{n-1} via Φ , apply GyroBN_i independently on each \mathbb{P}_{-1}^i , and finally map back with Φ^{-1} . For a batch of activations $\{C^i\}_{i=1}^N \subset \text{Cor}^+(n)$, the process can be expressed as

$$\forall i \leq N, \quad C^i \xrightarrow{\Phi} \begin{bmatrix} x_1^i \in \mathbb{P}_{-1}^1 \\ \vdots \\ x_{n-1}^i \in \mathbb{P}_{-1}^{n-1} \end{bmatrix} \xrightarrow{\text{GyroBN}_1} \begin{bmatrix} \tilde{x}_1^i \in \mathbb{P}_{-1}^1 \\ \vdots \\ \tilde{x}_{n-1}^i \in \mathbb{P}_{-1}^{n-1} \end{bmatrix} \xrightarrow{\Phi^{-1}} \tilde{C}^i. \quad (47)$$

5.8 Summary

To conclude this section, Table 7 summarizes the key gyro operators needed to implement GyroBN on representative manifolds. The correlation manifold is excluded, since its GyroBN is realized row-wise through the Poincaré ball.

6 Experiments

Our GyroBN layers are model-agnostic and can be seamlessly integrated into networks over gyrogroups. This section evaluates GyroBN on the Grassmannian, five constant curvature spaces, and the correlation manifold. The main findings are summarized as follows.

Geometry	Hyperboloid		Sphere	
	Riemannian	Close-form	Riemannian	Close-form
16	361.22	121.68 (33.69%)	323.58	122.02 (37.71%)
32	363.41	123.08 (33.87%)	327.75	123.71 (37.74%)
64	387.94	181.50 (46.78%)	453.42	181.05 (39.93%)
128	574.37	272.10 (47.37%)	644.18	270.21 (41.95%)
256	1149.58	534.09 (46.46%)	1137.62	538.58 (47.34%)
1024	3364.23	1414.67 (42.05%)	3551.69	1421.67 (40.03%)
2048	6479.95	2497.47 (38.54%)	6930.69	2449.56 (35.34%)

Table 8: Efficiency (in μs) of gyroaddition on the radius manifold: closed form v.s. Riemannian definition. Values in parentheses indicate the runtime of the closed-form implementation as a percentage of the corresponding Riemannian implementation.

- *Numerical Experiments (Section 6.1)*. The closed-form expression derived for radius gyroaddition in Equation (31) significantly accelerate the computation compared to their definition-based counterpart in Equation (26), achieving $2\times-3\times$ speedups. Furthermore, visualizations demonstrate that GyroBN effectively normalizes sample distributions across diverse geometries.
- *Performance (Sections 6.2 to 6.4)*. On Grassmannian, constant curvature, and correlation networks, GyroBN consistently improves backbone networks, whereas existing RBN methods often degrade performance. Compared to these methods, GyroBN is generally faster or comparable in runtime, requires fewer or equal parameters, and improves robustness.
- *Discussions (Section 6.5)*. Ablations further validate the design: (i) covariate shift is evident in manifold networks, underscoring the necessity of normalization; (ii) GyroBN consistently reduces the condition numbers of both weight matrices and network Jacobians, thereby stabilizing optimization; (iii) Fréchet mean iterations need not to be run to full convergence, since one or two iterations are generally sufficient, which provides a favorable trade-off between efficiency and accuracy.

6.1 Numerical Experiments

6.1.1 EFFICIENCY OF THE CLOSED-FORM RADIUS GYROADDITION

Recalling Section 5.5.1, we derive closed-form expressions for the radius gyrooperations to improve computational efficiency. To assess this, we compare two variants of radius gyroaddition: (i) the definition-based operator Equation (26), implemented via a composition of the Riemannian logarithm, parallel transport, and exponential map; and (ii) the closed-form operator Equation (31). We report the mean wall-clock time (in μs), averaged over 100 runs with a batch size of 10,000, across varying dimensions. As shown in Table 8, our closed-form implementation consistently outperforms its definition-based counterpart, achieving speedups of roughly $2\times-3\times$ across the hyperboloid and sphere.

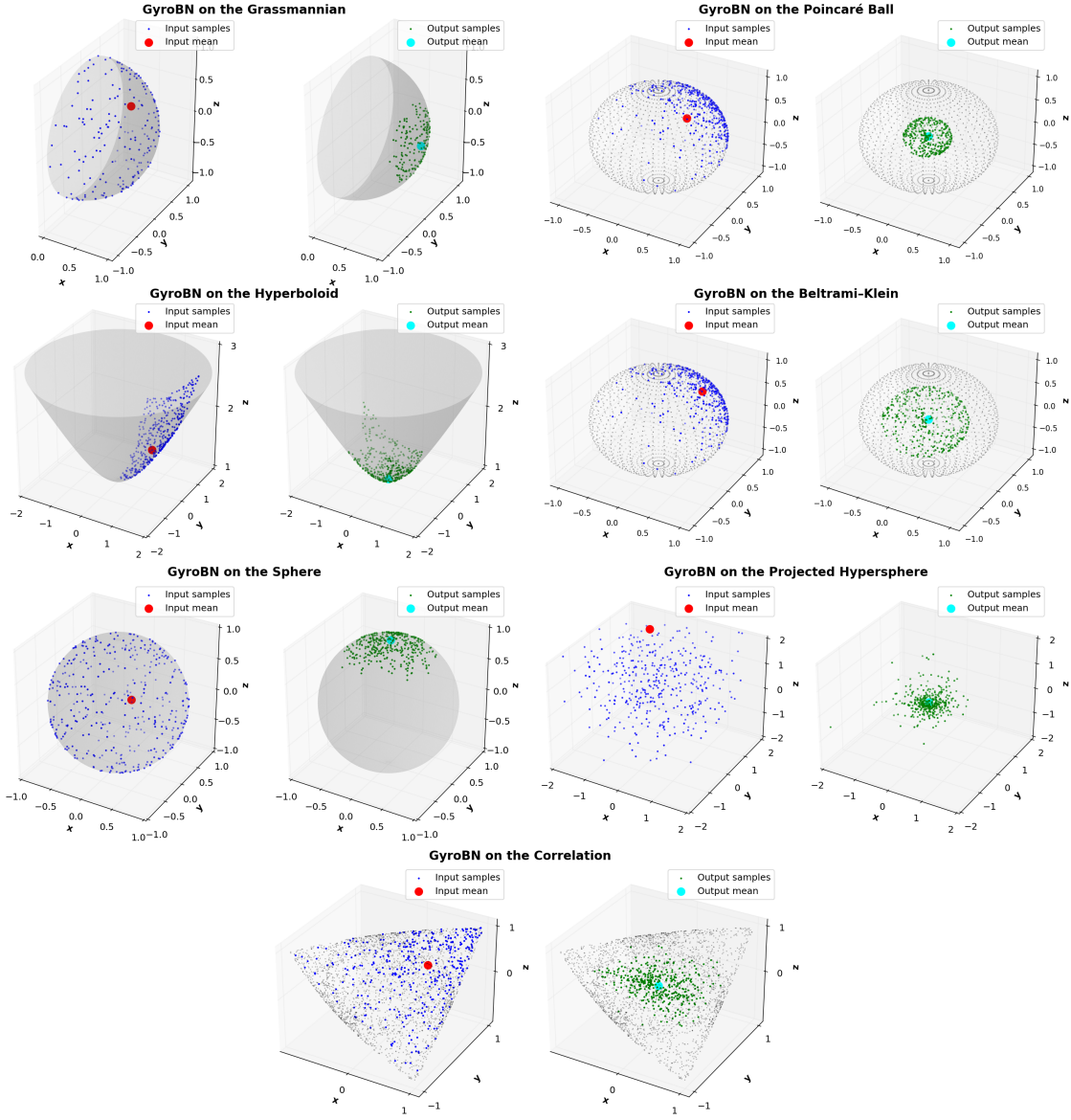


Figure 4: Visualization of GyroBN across different geometries. Blue and green points represent input and normalized data, respectively. Red and cyan points denote the input and output batch means. Black points mark the manifold boundary, and the gray surface depicts the manifold.

6.1.2 VISUALIZATION OF GYROBN ON DIFFERENT GEOMETRIES

To intuitively illustrate the effect of GyroBN, we visualize its behavior on the ONB Grassmannian $\text{Gr}(1, 3)$, five constant curvature spaces with $|K| = 1$, and the correlation manifold $\text{Cor}^+(3)$. For each geometry, we randomly generate a batch of points, compute their batch mean, apply GyroBN, and then plot the normalized batch along with the resulting mean. The visualizations are constructed using the following embeddings:

- *Grassmannian*. Since $\text{Gr}(1, 3)$ is homeomorphic to the real projective space \mathbb{RP}^2 , it is depicted as the unit hemisphere with antipodal points identified.
- *Constant Curvature Spaces*. The unit Poincaré ball \mathbb{P}_{-1}^3 and unit Beltrami–Klein ball \mathbb{K}_{-1}^3 are shown as the interior of the unit ball in \mathbb{R}^3 . The unit hyperboloid \mathbb{H}_{-1}^2 is visualized as the upper sheet of a two-sheeted hyperboloid in \mathbb{R}^3 . The unit sphere \mathbb{S}_{-1}^2 is embedded as a 2-sphere in \mathbb{R}^3 , while the projected hypersphere \mathbb{D}_{-1}^2 coincides with \mathbb{R}^3 itself.
- *Correlation Manifold*. $\text{Cor}^+(3)$ is embedded in \mathbb{R}^3 as an open ellipsope using its strictly lower triangular part.

For better visualization, we fix the bias parameter to the gyro identity element and set the scaling parameter to 0.4 for the Grassmannian, correlation manifold, and sphere; 0.7 for the Poincaré ball, Beltrami–Klein ball, and hyperboloid; and 1 for the projected hypersphere. As shown in Figure 4, GyroBN consistently normalizes data distributions across these geometries. Notably, although the Poincaré and Beltrami–Klein inputs are identical, their GyroBN behavior and resulting sample distributions differ due to their distinct Riemannian metrics, underscoring that GyroBN faithfully respects the underlying geometry.

6.2 Experiments on Grassmannian Neural Networks

6.2.1 SETUP

Data sets and Preprocessing. In line with previous work (Huang et al., 2018; Nguyen and Yang, 2023), we evaluate our method on three skeleton-based action recognition tasks, including HDM05 (Müller et al., 2007), NTU60 (Shahroudy et al., 2016), and NTU120 (Liu et al., 2019) data sets, focusing on mutual actions for NTU60 and NTU120. Each sequence is represented as a Grassmannian matrix of size 93×10 , 150×10 , and 150×10 for HDM05, NTU60, and NTU120, respectively. Additional details are provided in Section D.2.1.

Comparative Methods. Since no Grassmannian-specific batch normalization methods exist, we adapt two previous approaches to the Grassmannian: ManifoldNorm (Chakraborty, 2020, Algorithms 1–2) and the Riemannian batch normalization method of Lou et al. (2020, Algorithm 2), which we denote LRBN for clarity. Both methods are briefly reviewed in Section D.1. Although neither was originally designed for the Grassmannian, they can be adapted by employing Riemannian operators such as geodesics, exponential/logarithmic maps, and parallel transport. *The key difference is that our GyroBN can normalize data distributions across different geometries, whereas the other two methods cannot.*

Backbone Networks. We adopt the recently proposed GyroGr architecture (Nguyen and Yang, 2023) as our backbone, which is briefly reviewed in Section D.2.2. GyroGr replaces the non-intrinsic FRMap + ReOrth block in GrNet (Huang et al., 2018) with Grassmannian left gyrotranslation, thereby improving numerical stability and performance. It consists of three basic components: left gyrotranslation, pooling (Huang et al., 2018), and the Projection Map (ProjMap) (Huang et al., 2018), where ProjMap maps Grassmannian points to symmetric matrices for classification. We consider both the 1-block and L -block variants. The 1-block version is structured as: gyrotranslation \rightarrow pooling \rightarrow ProjMap \rightarrow classification, where the

Method	HDM05 (47 × 10)			NTU60 (75 × 10)			NTU120 (75 × 10)		
	Acc	Fit Time	#Params	Acc	Fit Time	#Params	Acc	Fit Time	#Params
GyroGr	48.97±0.24	2.09	2.0744	70.13±0.16	28.16	0.5062	53.76±0.18	49.62	1.1812
GyroGr-ManifoldNorm	49.67±0.76	32.90	2.0921	68.56±0.43	232.60	0.5512	51.41±0.38	399.78	1.2262
GyroGr-LRBN	48.64±0.77	33.31	2.0781	67.77±0.52	238.53	0.5122	50.56±0.22	403.40	1.1872
GyroGr-GyroBN	51.89±0.37	3.04	2.0773	72.60±0.04	35.85	0.5114	55.47±0.10	67.37	1.1864

Table 9: Comparison of GyroBN against other Grassmannian BN methods under the GyroGr backbone. Here, fit time denotes the average training time per epoch (s/epoch), and #Params denotes the number of parameters. Values in parentheses specify the dimension of the Grassmannian input to the BN layer. The best results are marked in **bold**, while the largest number of parameters is marked in **red**.

classification is implemented as a Fully Connected (FC) layer with softmax. The L -block version stacks L blocks of gyrotranslation and pooling, followed by a final ProjMap and classification layer. Since each pooling step approximately halves the dimensionality, we omit the pooling operation in the last block when $L > 1$. Following Huang et al. (2018), the number of channels is fixed to 8.

Implementation Details. Following Nguyen and Yang (2023), we use the Cayley map to approximate the matrix exponential of skew-symmetric matrices, and apply the trivialization trick (Lezcano Casado, 2019) to parameterize the Grassmannian variables in both the gyrotranslation and our GyroBN layers. Specifically, each Grassmannian parameter is trivialized via the exponential map at the identity, as detailed in Section D.2.3, ensuring that all parameters lie in Euclidean spaces. This allows direct use of PyTorch optimizers (Paszke et al., 2019) and avoids the additional cost of Riemannian optimization. In contrast, we find that the Grassmannian LRBN benefits from Riemannian optimization. Thus, we employ `geoopt` (Kochurov et al., 2020) to optimize its Grassmannian bias parameter. Similarly, we use `geoopt` to update the orthogonal bias parameter in ManifoldNorm. For all models, the BN layer is inserted after the first pooling layer with a momentum of 0.1. Training uses SGD with a learning rate of $5e^{-2}$, batch size 30, and 400, 200, and 200 epochs for HDM05, NTU60, and NTU120, respectively. All models are optimized with a standard cross-entropy loss. Following previous normalization methods on matrix manifolds (Kobler et al., 2022a; Chen et al., 2024b; Wang et al., 2025), we adopt a single Fréchet mean iteration.

6.2.2 MAIN RESULTS

We compare our GyroBN with ManifoldNorm and LRBN under the 1-block GyroGr backbone. The 5-fold results are presented in Table 9. We have the following four findings, which highlight the effectiveness of our GyroBN in facilitating network training.

- *Improved Accuracy.* Across all three data sets, GyroBN consistently improves performance, enhancing the accuracy of the vanilla GyroGr by +2.92%, +2.47%, and +1.71% on HDM05, NTU60, and NTU120, respectively. In contrast, both ManifoldNorm and LRBN often degrade performance, particularly on NTU60 and NTU120. This advantage comes from the theoretical guarantee of GyroBN for normalizing sample statistics, which is absent in the other two methods (see Table 1).

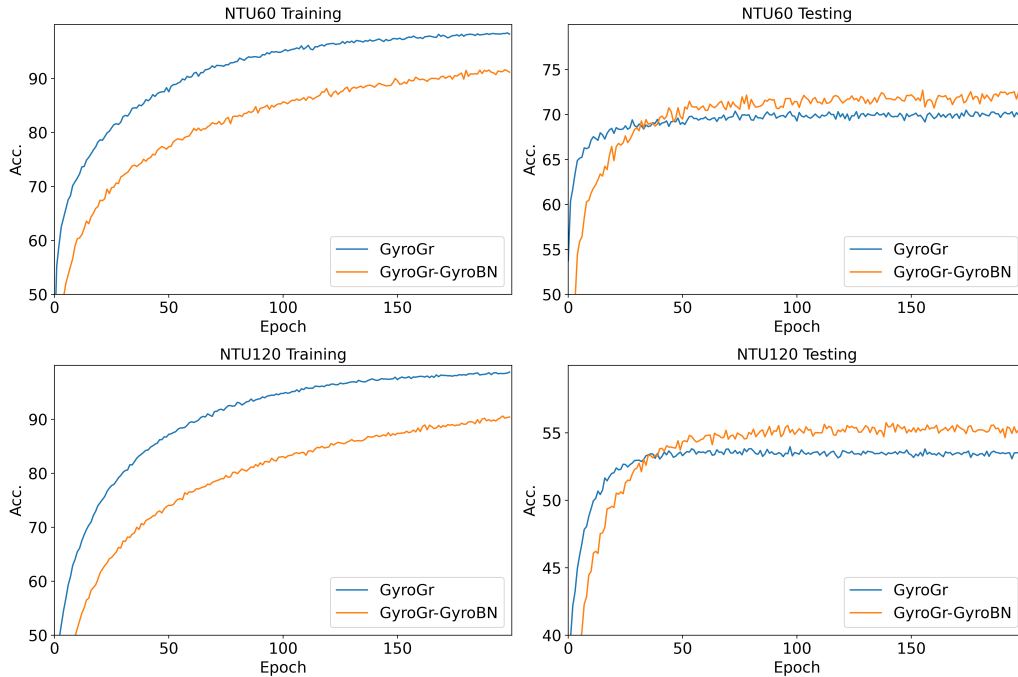


Figure 5: Training and testing curves of 1-block GyroGr on two NTU data sets.

- *Enhanced Efficiency.* GyroBN is substantially more efficient than ManifoldNorm and LRBN. The efficiency gain is mainly attributed to: (i) replacing computationally expensive Riemannian operators (e.g., parallel transport, exponential/logarithmic maps) with simpler gyro operations, (ii) reducing matrix multiplications from $n \times p$ to $(n - p) \times p$ or $p \times p$ (see Theorem 19), and (iii) applying trivialization to avoid costly Riemannian optimization. A detailed analysis is provided in Section D.2.4.
- *Improved Parameter Economy.* GyroBN also requires fewer parameters than LRBN and ManifoldNorm. The key difference lies in the bias parameter. GyroBN, due to the trivialization in Section D.2.3, only needs an $(n - p) \times p$ Euclidean matrix, whereas LRBN requires an $n \times p$ Grassmannian matrix and ManifoldNorm requires an $n \times n$ orthogonal matrix.
- *Stronger Generalization.* As shown in Figure 5, we observe that GyroBN can narrow the gap between training and testing accuracy, indicating a stronger generalization ability.

6.2.3 ABLATIONS ON ARCHITECTURES

We further validate GyroBN across different GyroGr architectures with up to four blocks of gyrotranslation and pooling. As shown in Table 9, both GyroGr and GyroGr-GyroBN exhibit relatively small variances, so we perform ablations using a single trial. The results of all three data sets are reported in Table 10. We find that GyroBN consistently improves the vanilla GyroGr baseline, highlighting the effectiveness of the proposed framework. Notably,

Method	HDM05				NTU60				NTU120			
	1-Block	2-Block	3-Block	4-Block	1-Block	2-Block	3-Block	4-Block	1-Block	2-Block	3-Block	4-Block
GyroGr	49.23	49.09	47.02	27.36	70.32	70.14	70.23	65.03	53.96	54.1	54.59	47.59
GyroGr-GyroBN	52.43	50.62	51.56	30.29	72.65	71.93	72.25	66.67	55.59	56.15	54.63	48.9

Table 10: Ablation of Grassmannian GyroBN under various network architectures.

as network depth increases, the performance of GyroGr, with or without GyroBN, declines. This degradation arises because the dimensionality of the final feature representation becomes excessively low, leading to underfitting. For example, in the deepest four-block architecture on the HDM05 data set, the final feature dimension is 12×10 , which is insufficient to capture discriminative information. Nevertheless, GyroBN still provides consistent improvements over GyroGr across all settings.

6.3 Experiments on Constant Curvature Neural Networks

6.3.1 SETUP

Data sets. Following Lou et al. (2020), we focus on the link prediction task on four graph data sets: Cora (Sen et al., 2008), Disease (Anderson and May, 1991), Airport (Zhang and Chen, 2018), and Pubmed (Namata et al., 2012). Details can be found in Section D.3.1.

Comparative Methods. We compare our GyroBN with LRBN (Lou et al., 2020, Algorithm 2). As the original LRBN is only implemented in the Poincaré ball, we extend it to the other four constant curvature spaces. In particular, the core difference between LRBN and our GyroBN lies in normalization: Our GyroBN can normalize sample statistics across different geometries, while LRBN lacks this guarantee.

Backbone Networks. We use HNN (Ganea et al., 2018) for the Poincaré ball and Klein HNN (KNN) (Mao et al., 2024) for the Beltrami–Klein. For the sphere and projected hypersphere, we mimic the transformation and activation in HNN (Ganea et al., 2018, Section 3.2) to build the corresponding layers. The layers on the four spaces above can be expressed as

$$\text{Transformation: } x^k = \text{Exp}_e(M^k \text{Log}_e(x^{k-1})) \oplus b^k, \text{ with } b^k \in \mathcal{N}, \text{ and } M^k \in \mathbb{R}^{m \times n}, \quad (48)$$

$$\text{Activation: } x^k = \text{Exp}_e(\phi(\text{Log}_e(x^{k-1}))), \text{ with } \phi \text{ as an activation}, \quad (49)$$

where e is the origin, \oplus is the gyroaddition, and $\mathcal{N} \in \{\mathbb{P}_K^n, \mathbb{K}_K^n, \mathbb{S}_K^n, \mathbb{D}_K^n\}$. For the hyperboloid, we use the Lorentz fully-connected layer (Chen et al., 2021, Equation 3) and Lorentz activation layer (Bdeir et al., 2024, Equation 13), which are briefly reviewed in Section D.3.2. The above backbone network is referred to as HNN, KNN, SNN, PHNN, and LNN, respectively. We collectively call them Constant Curvature Neural Networks (CCNNs). We also adopt Riemannian ResNet (RResNet) (Katsman et al., 2024) and HNN++ (Shimizu et al., 2021) as additional backbones.

Implementation Details on CCNNs. We follow the official implementations of HGNC⁸ (Chami et al., 2019), LRBN⁹ (Lou et al., 2020), and HCNN¹⁰ (Bdeir et al., 2024) to conduct

8. <https://github.com/HazyResearch/hgcn>
9. <https://github.com/CUAI/Differentiable-Frechet-Mean>
10. <https://github.com/kschwethelm/HyperbolicCV>

GYROBN

Space		Poincaré Ball \mathbb{P}_K^n			Hyperboloid \mathbb{H}_K^n			Beltrami-Klein \mathbb{K}_K^n		
Method		HNN	HNN-LRBN	HNN-GyroBN	LNN	LNN-LRBN	LNN-GyroBN	KNN	KNN-LRBN	KNN-GyroBN
Disease	Roc	79.21 ± 2.14	76.58 ± 2.15	81.18 ± 0.93	87.71 ± 1.42	85.31 ± 0.95	88.87 ± 0.33	81.31 ± 1.37	78.98 ± 1.51	81.56 ± 0.70
	Fit Time	0.027	0.088	0.084	0.012	0.057	0.057	0.020	0.089	0.077
	#Params	0.0180	0.0183	0.0183	0.0184	0.0187	0.0187	0.0180	0.0183	0.0183
Airport	Roc	94.63 ± 0.19	94.17 ± 0.40	95.40 ± 0.17	93.86 ± 0.21	93.05 ± 1.00	95.06 ± 0.12	95.00 ± 0.05	94.47 ± 0.33	96.14 ± 0.05
	Fit Time	0.054	0.122	0.119	0.047	0.089	0.092	0.056	0.136	0.126
	#Params	0.0182	0.0184	0.0184	0.0186	0.0188	0.0188	0.0182	0.0184	0.0184
Pubmed	Roc	95.02 ± 0.42	93.40 ± 0.20	95.83 ± 0.11	95.36 ± 0.10	95.88 ± 0.09	95.89 ± 0.11	95.87 ± 0.11	89.83 ± 0.27	96.23 ± 0.12
	Fit Time	0.125	0.342	0.335	0.111	0.242	0.249	0.125	0.353	0.337
	#Params	0.0806	0.0809	0.0809	0.0815	0.0818	0.0818	0.0806	0.0809	0.0809
Cora	Roc	89.96 ± 0.44	93.47 ± 0.49	94.32 ± 0.22	91.84 ± 1.01	92.62 ± 0.17	93.66 ± 0.30	90.03 ± 0.32	93.38 ± 0.12	93.48 ± 0.25
	Fit Time	0.032	0.091	0.076	0.114	0.244	0.242	0.038	0.091	0.076
	#Params	0.2001	0.2003	0.2003	0.2019	0.2021	0.2021	0.2001	0.2003	0.2003

(a) Results on three hyperbolic spaces.

Space		Projected Hypersphere \mathbb{D}_K^n			Sphere \mathbb{S}_K^n		
Method		PHNN	PHNN-LRBN	PHNN-GyroBN	SNN	SNN-LRBN	SNN-GyroBN
Disease	Roc	69.70 ± 2.01	60.25 ± 1.25	72.26 ± 0.61	54.19 ± 2.21	53.38 ± 4.07	71.84 ± 0.89
	Fit Time	0.022	0.066	0.063	0.029	0.042	0.043
	#Params	0.0180	0.0183	0.0183	0.0181	0.0183	0.0183
Airport	Roc	89.60 ± 0.99	87.06 ± 0.46	90.44 ± 0.93	83.63 ± 0.77	86.14 ± 0.79	91.12 ± 1.57
	Fit Time	0.056	0.102	0.095	0.053	0.070	0.071
	#Params	0.0182	0.0184	0.0184	0.0182	0.0184	0.0184
Pubmed	Roc	89.86 ± 0.39	90.06 ± 0.23	92.06 ± 0.64	79.94 ± 1.76	90.10 ± 0.21	93.31 ± 0.08
	Fit Time	0.121	0.175	0.174	0.120	0.140	0.156
	#Params	0.0806	0.0809	0.0809	0.0806	0.0809	0.0809
Cora	Roc	92.88 ± 0.26	92.03 ± 0.42	93.26 ± 0.42	92.10 ± 0.40	82.01 ± 0.71	93.16 ± 0.32
	Fit Time	0.026	0.067	0.063	0.025	0.044	0.045
	#Params	0.2001	0.2003	0.2003	0.2001	0.2003	0.2003

(b) Results on two spherical spaces.

Table 11: Comparison of GyroBN against LRBN across five constant curvature spaces. The best results are highlighted with **bold**. When LRBN degenerates the backbone network, the results are highlighted with **red**.

experiments, where we adopt the same training settings as Lou et al. (2020, Section H.1). Specifically, the baseline encoder is a CCNN with two transformation layers: the first maps the input feature dimension to 128, and the second maps 128 to 128. After each transformation layer, we use a ReLU activation (in Equations 49 and D.9), except for the Cora data set where activation is omitted. A BN layer, GyroBN or LRBN, is inserted after each transformation layer. The curvature is set as $|K| = 1$. For the manifold-valued bias parameter in GyroBN and LRBN, we apply the exponential map $\text{Exp}_e(v)$ to trivialize it via a Euclidean parameter v . The optimization is performed with Adam (Kingma, 2014), using a learning rate of $1e^{-2}$ and a weight decay of $1e^{-3}$, except for the Cora data set, where weight decay is set to 0. The Fréchet mean iterations are performed until convergence.

6.3.2 MAIN RESULTS

We compare our GyroBN with LRBN across five constant curvature spaces under the CCNN backbone. Table 11 reports the 5-fold average testing AUC on four data sets. We highlight the following findings.

- *Improved Performance.* GyroBN consistently improves performance over the vanilla CCNNs across all data sets and geometries, whereas LRBN degrades performance in several cases (highlighted in **red**). The gains are especially pronounced on the sphere

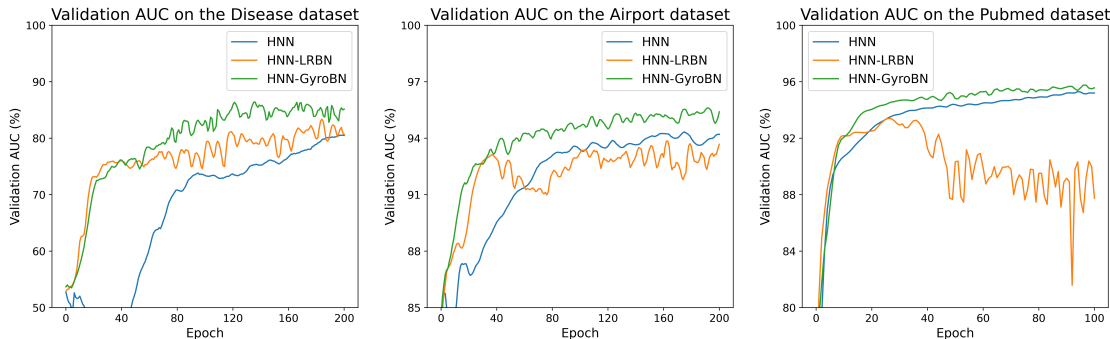


Figure 6: Validation AUC of HNN with or without GyroBN or LRBN.

Method	Disease	Airport	Cora
HNN++	80.19 \pm 0.51	94.74 \pm 0.24	91.06 \pm 0.47
HNN++-LRBN	61.18 \pm 1.00	95.21 \pm 0.65	88.22 \pm 0.67
HNN++-GyroBN	81.06 \pm 0.95	95.77 \pm 0.18	92.83 \pm 0.32

Weight Decay	0	$1e^{-3}$	$5e^{-4}$
HNN++	96.03 \pm 0.13	69.26 \pm 0.47	70.75 \pm 0.33
HNN++-LRBN	92.33 \pm 0.32	92.18 \pm 0.18	92.16 \pm 0.57
HNN++-GyroBN	95.48 \pm 0.20	95.36 \pm 0.18	95.56 \pm 0.10

(a) Main Results.

(b) Pubmed with varying weight decay.

Table 12: LRBN vs. GyroBN on Poincaré HNN++.

(SNN), where GyroBN achieves improvements of +17.65% (Disease), +7.49% (Airport), and +13.37% (Pubmed). This contrast underscores the advantage of GyroBN’s theoretical guarantee of normalizing sample statistics.

- *Efficiency.* As shown in the “Fit Time” rows of Table 11, GyroBN is more efficient than LRBN on the Poincaré ball, Beltrami–Klein and projected hypersphere, due to the simplicity of gyro operations. On the hyperboloid and sphere, GyroBN and LRBN exhibit comparable efficiency.
- *Parameter Equivalence.* GyroBN and LRBN require the same number of parameters, only marginally more than those of the vanilla backbone. Thus, the performance gains of GyroBN cannot be attributed to parameter size, but rather to its principled normalization mechanism.

6.3.3 ABLATIONS

Training Dynamics. Figure 6 presents the validation AUC curves on the Poincaré HNN. LRBN can even degrade baseline performance. In contrast, GyroBN consistently accelerates convergence and enhances overall performance.

Results on HNN++. We further validate our GyroBN on Poincaré HNN++¹¹ (Shimizu et al., 2021), which are briefly reviewed in Section D.3.2. It replaces the transformation layer in Equation (48) with a Poincaré FC layer (Shimizu et al., 2021, Section 3.2) for a more intrinsic transformation. Following the HNN experiments, we adopt a 2-block HNN++ as the encoder, consisting of two blocks of Poincaré FC and activation layers. Similarly, the BN

11. https://github.com/mil-tokyo/hyperbolic_nn_plusplus

GYROBN

Dim	8	16	32	64	128
RResNet	68.32 ± 11.31	67.01 ± 9.58	71.48 ± 8.63	67.03 ± 2.91	54.19 ± 3.43
RResNet-LRBN	62.96 ± 7.27	69.77 ± 10.27	65.72 ± 0.91	71.62 ± 3.04	63.06 ± 3.88
RResNet-GyroBN	76.18 ± 2.98	77.32 ± 1.59	69.87 ± 2.97	76.38 ± 2.15	66.04 ± 4.04

(a) Results on the Disease data set.

Dim	8	16	32	64	128
RResNet	92.90 ± 0.45	91.20 ± 2.72	91.30 ± 0.82	89.70 ± 1.90	89.34 ± 0.66
RResNet-LRBN	90.42 ± 1.43	88.56 ± 2.36	89.05 ± 1.25	89.65 ± 1.56	88.77 ± 2.22
RResNet-GyroBN	94.28 ± 1.51	91.65 ± 2.30	92.37 ± 1.07	90.41 ± 0.65	89.65 ± 0.32

(b) Results on the Airport data set.

Dim	8	16	32	64	128
RResNet	71.77 ± 6.67	77.38 ± 10.82	77.14 ± 7.48	66.73 ± 11.85	80.75 ± 4.12
RResNet-LRBN	61.94 ± 2.28	63.54 ± 3.01	62.26 ± 3.48	60.38 ± 2.97	87.92 ± 2.67
RResNet-GyroBN	84.58 ± 5.44	87.67 ± 2.53	88.08 ± 2.90	86.50 ± 1.59	89.52 ± 3.42

(c) Results on the Cora data set.

Table 13: LRBN vs. GyroBN on the Poincaré RResNet with different hidden dimensions.

layer is inserted after each Poincaré FC layer. Other settings remain the same. The 5-fold average results are reported in Table 12. We highlight the following findings.

- *Improved Performance and Robustness.* While LRBN can degrade HNN++’s performance, particularly on the Disease data set, GyroBN consistently enhances it. We also observe that HNN++ could be sensitive to weight decay. For instance, on the Pubmed, setting the weight decay to $1e^{-3}$ reduces drastically the performance, from 96.03% to 69.26%. In contrast, HNN++ with GyroBN is robust to weight decay.
- *Accelerated convergence.* On Cora, vanilla HNN++ requires more than 400 epochs to converge, whereas HNN++-GyroBN converges in roughly 150 epochs, substantially speeding up training.

Results on RResNet. As an additional backbone, we adopt the Poincaré RResNet Horo¹² (Katsman et al., 2024), which extends the classical ResNet (He et al., 2016) to the Poincaré ball. For brevity, we denote it RResNet. A brief review is provided in Section D.3.2. The input features are first mapped by a Euclidean linear layer into a hidden dimension and then projected onto the Poincaré ball. The resulting representations are processed by RResNet, consisting of two residual blocks parameterized by horosphere-induced vector fields. A normalization layer, LRBN or our GyroBN, is inserted after RResNet, followed by a ReLU activation as defined in Equation (49). For a complete comparison, we vary the hidden dimension from 8 to 128. Training is performed with a learning rate of $1e^{-2}$ and a weight decay of $1e^{-3}$, while keeping other settings identical to Katsman et al. (2024). The 5-fold average results are summarized in Table 13, leading to the following findings.

1. *Improved Performance.* LRBN often degrades the RResNet baseline, particularly on the Airport and Cora data sets. In contrast, GyroBN consistently improves accuracy across most hidden dimensions, with gains of up to +11.85% on Disease (from 54.19%

12. <https://github.com/CUAI/Riemannian-Residual-Neural-Networks>

Methods	Radar			HDM05			FPHA		
	Acc	Fit Time	#Params	Acc	Fit Time	#Params	Acc	Fit Time	#Params
CorNet	96.56 ± 0.86	2.12	0.0438	82.26 ± 0.92	0.74	0.4091	90.03 ± 0.63	0.70	1.1210
CorNet-LRBN	92.85 ± 2.46	2.33	0.0439	N/A	1.64	0.4094	81.53 ± 0.72	1.12	1.1213
CorNet-GyroBN	97.67 ± 0.36	2.19	0.0439	80.82 ± 0.86	1.33	0.4094	92.88 ± 0.20	1.07	1.1213

Table 14: Comparison of CorNet with or without RBN layers.

to 66.04%), +1.38% on Airport (from 92.90% to 94.28%), and +19.77% on Cora (from 66.73% to 86.50%).

2. *Stabilized Training.* On the Cora data set, both RResNet and RResNet-LRBN are highly sensitive to hidden dimensions, leading to large performance fluctuations. In contrast, RResNet-GyroBN exhibits much stabler performance, indicating that GyroBN not only improves accuracy but also enhances robustness to architectural variations.

6.4 Experiments on Correlation Neural Networks

6.4.1 SETUP

Data sets and Preprocessing. Following Chen et al. (2025d), we use the Radar, HDM05 and FPFA data sets, modeling each input sequence as multichannel correlation matrices. Please refer to Sections D.4.1 and D.4.2 for more details.

Comparative Methods. Similar to Section 6.3, we compare GyroBN against LRBN.

Backbone Networks. We adopt CorNet-PHCM (Chen et al., 2025d), abbreviated as CorNet, as the backbone network. CorNet identifies each correlation matrix $C \in \text{Cor}^+(n)$ with a Poincaré vector and applies Poincaré layers. Specifically, C is mapped to the poly-Poincaré space $\mathbb{P}\mathbb{P}^{n-1}$ via Equation (46). The resulting multi-channel Poincaré vectors are then merged into a single Poincaré representation through β -concatenation (Shimizu et al., 2021, Section 3.3), as recapped in Section D.3.2. Then, a Poincaré FC layer followed by a Poincaré Multinomial Logistics Regression (MLR) layer constructs the network.

Implementation Details. We follow all the implementation settings in Chen et al. (2025d). Since CorNet operates in the Poincaré geometry, both GyroBN and LRBN are instantiated in the Poincaré model and applied after the Poincaré FC layer. To stabilize training, we scale the learning rate of the shift parameter s by factors of 0.1 and 0.5 for Radar and HDM05, respectively. On FPFA, we further regularize the scaling by clamping: $\min\left(\frac{s}{\sqrt{v^2+c}}, 4\right)$. For better efficiency, the number of Fréchet mean iterations is set to 2.

6.4.2 MAIN RESULTS

We summarize the comparison of CorNet with or without normalization layers in Table 14. Overall, GyroBN demonstrates clear benefits on Radar and FPFA with negligible parameter cost and modest efficiency trade-offs. On HDM05, however, neither GyroBN nor LRBN improves the baseline, with LRBN even diverging and failing to converge.

	Pooling	Transformation
$d(M_{out}, I_{p,n})$	2.90 ± 0.11	4.18 ± 0.04
Δ (%)	$58.47\% \pm 2.28\%$	$84.22\% \pm 0.72\%$

Table 15: Ten-fold results for geodesic distance $d(M_{out}, I_{p,n})$ and shift $\Delta = \frac{d(M_{out}, I_{p,n})}{\sqrt{p\pi/2}} \times 100$.

6.5 Discussions

6.5.1 ABLATIONS ON COVARIATE SHIFTS

The covariate shift is the central motivation behind the classical Euclidean BN (Ioffe and Szegedy, 2015). Similar issues also arise in Riemannian networks, which can distort data distributions across layers, highlighting the importance of normalization. To examine this phenomenon, we conduct numerical experiments on Grassmannian and hyperbolic networks.

Grassmannian. The transformation and pooling layers in the GyroGr baseline, which are recapped in Equations (D.5) and (D.7), can be expressed as

$$\begin{aligned} f_{\text{trans}} &: \text{Gr}(p, n) \rightarrow \text{Gr}(p, n), \\ f_{\text{pooling}} &: \text{Gr}(p, n) \rightarrow \text{Gr}(p, n/2). \end{aligned}$$

For simplicity, we assume n is even for the pooling layer. Since the ONB Grassmannian $\text{Gr}(p, n)$ is a quotient manifold and pooling changes dimensions, we use the geodesic distance between the batch mean and the identity element $I_{p,n} = (I_p, \mathbf{0})^\top \in \mathbb{R}^{n \times p}$ as a consistent measure. Note that the geodesic distance on $\text{Gr}(p, n)$ is bounded by $\sqrt{p}\frac{\pi}{2}$ (Wong, 1967, Theorem 8). We randomly generate 30 Grassmannian matrices of size 100×10 with an initial batch mean as the identity element $I_{p,n}$. We denote the resulting batch mean after transformation or pooling as M_{out} . If the distribution were preserved, the geodesic distance $d(M_{out}, I_{p,n})$ (or $d(M_{out}, I_{p,n/2})$ for pooling) would be zero. Table 15 shows that M_{out} significantly deviates from $I_{p,n}$, indicating the covariate shift.

Hyperbolic Spaces. We examine the covariate shift of the transformation layer in the Poincaré HNN (Equation (48)). We focus on the canonical Poincaré ball (curvature $K = -1$). We randomly generate 30 5-dimensional Poincaré vectors. The batch mean vectors of input and output in the transformation layer are

$$\begin{aligned} M_{in} &= [-0.0055, 0.0503, -0.0913, -0.0493, 0.0652]^\top, \\ M_{out} &= [-0.0969, -0.0443, 0.0385, 0.0936, -0.0770]^\top. \end{aligned}$$

The geodesic distance between M_{in} and M_{out} is 0.55, indicating the covariate shift in HNN.

6.5.2 ABLATIONS ON CONDITION NUMBERS

In the GyroGr network, the transformation layer outputs $n \times p$ Grassmannian matrices whose singular values are all 1, yielding trivial condition numbers. Similarly, the transformation layers in constant curvature networks output vectors, which also lead to trivial condition numbers. For CorNet, where each correlation is identified as a Poincaré vector, the condition

Data set	BN	Mean	Min	Max
HDM05	None	3.81 ± 0.23	3.46	4.17
	ManifoldNorm	1.97 ± 0.15	1.83	2.30
	LRBN	3.49 ± 0.46	2.96	4.43
	GyroBN	2.37 ± 0.18	2.12	2.67
NTU120	None	3.35 ± 0.28	2.97	3.72
	ManifoldNorm	1.91 ± 0.10	1.80	2.14
	LRBN	2.22 ± 0.11	2.00	2.36
	GyroBN	2.16 ± 0.11	2.00	2.33

(a) Weight matrices in the transformation layer.

Data set	BN	Mean	Min	Max
HDM05	None	61.05 ± 4.15	52.19	74.29
	ManifoldNorm	67.38 ± 6.82	51.15	88.81
	LRBN	64.16 ± 6.44	50.54	80.07
	GyroBN	59.85 ± 4.33	48.46	70.47
NTU120	None	122.24 ± 68.45	61.8	399.28
	ManifoldNorm	116.75 ± 65.17	75.46	443.01
	LRBN	108.75 ± 52.27	63.19	349.25
	GyroBN	97.01 ± 41.88	61.19	262.55

(b) Network Jacobian (output w.r.t. input).

Table 16: Condition numbers under different normalization methods on the GyroGr baseline.

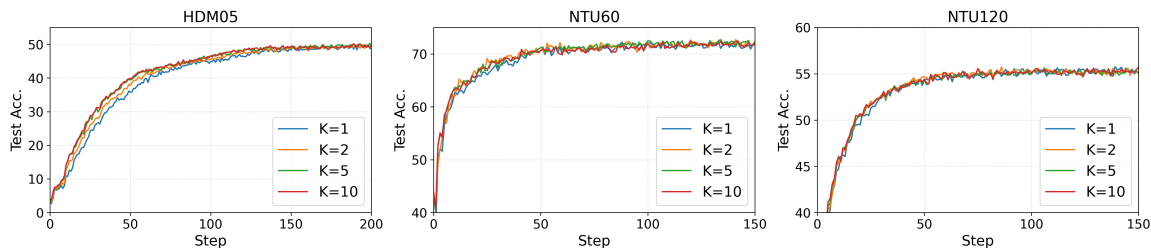


Figure 7: Testing accuracy curve of the Grassmannian GyroGr-GyroBN under different Karcher steps.

numbers are likewise trivial. Hence, we focus our analysis on the condition numbers of the weight matrices in the hidden transformation layer and the overall network Jacobian. Both analyses are conducted on the Grassmannian GyroGr under the 1-block architecture. To cover different scales, we report results on small-scale HDM05 and large-scale NTU120.

Transformation Layers. Since the weight matrices have 8 channels, we report the mean, standard deviation (std), minimum, and maximum values of their condition numbers. The dimensions of the 8-channel transformation matrices are 83×10 and 140×10 on HDM05 and NTU120, respectively. As shown in Table 16a, GyroBN consistently reduces the condition numbers of the weight matrices across both data sets. Interestingly, although ManifoldNorm achieves the smallest condition numbers, its performance can be worse than the vanilla GyroGr baseline. This suggests that excessively reducing the condition number may constrain the model’s expressive capacity.

Network Jacobian. We randomly select 100 samples and feed them into the trained models to compute Jacobian statistics. The dimensions of the Jacobian matrices are 117×930 on HDM05 and 11×9600 on NTU120. As reported in Table 16b, GyroBN achieves lower condition numbers than competing methods on both data sets, indicating that it stabilizes network training. Moreover, the reduction in maximum condition numbers, especially on NTU120, highlights GyroBN’s ability to avoid extreme outliers in conditioning, further underscoring its advantage. Notably, on HDM05, both ManifoldNorm and LRBN actually increase the Jacobian condition numbers.

GYROBN

Geometry	Model	Iteration	Disease	Airport	Pubmed	Cora
Hyperbolic	Poincaré Ball	1	67.47 ± 2.76	91.74 ± 2.52	94.93 ± 0.39	92.39 ± 0.27
		2	74.76 ± 3.65	96.14 ± 0.10	95.93 ± 0.17	94.01 ± 0.23
		5	80.92 ± 1.19	96.06 ± 0.05	96.08 ± 0.08	94.03 ± 0.21
		10	81.44 ± 1.96	96.13 ± 0.12	96.05 ± 0.24	94.03 ± 0.21
		∞	81.18 ± 0.93	95.40 ± 0.17	95.83 ± 0.11	94.32 ± 0.22
	Hyperboloid	1	89.29 ± 0.52	94.50 ± 0.16	96.03 ± 0.03	93.72 ± 0.08
		2	88.96 ± 0.58	94.58 ± 0.21	96.02 ± 0.20	93.78 ± 0.25
		5	87.62 ± 1.49	94.60 ± 0.15	95.91 ± 0.11	93.80 ± 0.23
		10	89.35 ± 0.57	94.44 ± 0.17	96.01 ± 0.10	93.80 ± 0.23
		∞	88.87 ± 0.33	95.06 ± 0.12	95.89 ± 0.11	93.66 ± 0.30
	Beltrami–Klein	1	81.56 ± 1.71	96.06 ± 0.08	95.71 ± 0.19	93.27 ± 0.18
		2	81.62 ± 1.33	96.16 ± 0.08	95.83 ± 0.23	93.42 ± 0.13
5		81.38 ± 0.80	96.17 ± 0.17	95.88 ± 0.08	93.40 ± 0.15	
10		80.84 ± 1.08	96.15 ± 0.05	95.81 ± 0.19	93.38 ± 0.12	
∞		81.56 ± 0.70	96.14 ± 0.05	96.23 ± 0.12	93.48 ± 0.25	
Spherical	Projected Hypersphere	1	74.07 ± 0.83	91.32 ± 0.82	91.08 ± 0.26	92.30 ± 0.20
		2	71.64 ± 1.24	91.08 ± 0.43	91.34 ± 0.23	92.95 ± 0.46
		5	72.01 ± 1.20	90.90 ± 0.29	92.30 ± 0.24	92.76 ± 0.62
		10	72.25 ± 1.97	90.44 ± 0.93	91.89 ± 0.49	92.92 ± 0.16
		∞	72.26 ± 0.61	90.44 ± 0.93	92.06 ± 0.64	93.26 ± 0.42
	Projected Hypersphere	1	70.49 ± 3.18	91.57 ± 1.00	93.24 ± 0.31	92.43 ± 0.90
		2	72.96 ± 2.00	90.72 ± 1.90	93.24 ± 0.22	93.09 ± 0.53
		5	72.82 ± 1.74	89.61 ± 1.81	93.46 ± 0.10	92.85 ± 0.41
		10	71.73 ± 0.91	91.12 ± 1.57	93.31 ± 0.08	92.64 ± 0.35
		∞	71.84 ± 0.89	91.12 ± 1.57	93.31 ± 0.08	93.16 ± 0.32

Table 17: Ablation study on the number of Fréchet mean iterations for different constant curvature spaces. The symbol ∞ indicates that iterations are performed until convergence, which is the setting used in our main experiments.

Geometry	Iteration	HDM05	NTU60	NTU120
	1	3.04	35.85	67.37
Grassmannian	2	3.70	40.07	69.23
	5	5.51	54.49	93.03
	10	8.64	74.67	130.77

Table 18: Efficiency (s/epoch) of Grassmannian GyroBN under different Fréchet mean iterations. Entries in are the setting used in our main experiments.

6.5.3 ABLATIONS ON THE NUMBER OF FRÉCHET MEAN ITERATIONS

We ablate the number of iterations used by the Fréchet mean solver in GyroBN across the Grassmannian and five constant curvature spaces. Figure 7 shows that on the Grassmannian, a single iteration is sufficient. Similarly, Table 17 indicates that GyroBN over constant curvature spaces is generally saturated with two iterations, except for the Poincaré ball on the Disease data set, where ten iterations yield further improvement. Meanwhile, Table 18 highlights that reducing iterations substantially improves the efficiency of GyroBN.

7 Conclusion

We have introduced the pseudo-reductive gyrogroup, a novel gyro-structure on manifolds that establishes the prerequisites for principled normalization over gyrospaces. Building on this foundation, we proposed GyroBN, a general framework for batch normalization on gyrogroups that enables the normalization of non-Euclidean statistics. Our analysis reveals that several existing RBN methods, including LieBN on Lie groups and AIM-based SPDBNs, arise as special cases of GyroBN. We further instantiated GyroBN on the Grassmannian, five constant curvature spaces, and the correlation manifold, and demonstrated its effectiveness through extensive experiments. These contributions position GyroBN as a unified normalization paradigm for manifold-valued data. A natural direction for future work is to broaden this paradigm beyond gyrogroups, extending normalization to manifolds that do not admit gyro-structures.

Acknowledgments and Disclosure of Funding

This work was partly supported by the MUR PNRR project FAIR (PE00000013) funded by the NextGenerationEU, and the EU Horizon project ELIAS (No. 101120237). The authors also gratefully acknowledge the CINECA award under the ISCRA initiative for the availability of HPC resources support.

Appendix Contents

List of Acronyms	43
A Notations	43
B Existence and Uniqueness of the Weighted Fréchet Mean	43
C Grassmannian GyroBN under the projector perspective	45
D Experimental Details	48
D.1 Reviews of ManifoldNorm and LRBN	48
D.2 Details on the Grassmannian Experiments	48
D.2.1 Data Sets and Preprocessing	48
D.2.2 Basic Layers in GyroGr	49
D.2.3 Trivialization	49
D.2.4 Analysis on the Efficiency of GyroBN	50
D.3 Details on the Constant Curvature Space Experiments	50
D.3.1 Data Sets	50
D.3.2 Brief Review of Hyperbolic Neural Networks	51
D.4 Details on the Correlation Experiments	52
D.4.1 Data Sets and Preprocessing	52
D.4.2 Correlation Input in CorNets	52
D.5 Hardware	53
E Proofs	53
E.1 Proof of Theorem 7	53
E.2 Proof of Theorem 8	54
E.3 Proof of Theorem 10	55
E.4 Proof of Theorem 11	55
E.5 Proof of Theorem 12	57
E.6 Proof of Theorem 13	58
E.7 Proof of Theorem 14	58

E.8 Proof of Theorem 16	59
E.9 Proof of Theorem 19	60
E.10 Proof of Theorem 21	62
E.11 Proof of Theorem 22	63
E.12 Proof of Theorem 23	65
E.13 Proof of Theorem 24	65
E.14 Proof of Theorem 25	67
E.15 Proof of Theorem 26	69
E.16 Proof of Theorem 28	70
E.17 Proof of Theorem 30	70
E.18 Proof of Theorem 31	72
E.19 Proof of Theorem 32	73

List of Acronyms

BN	Batch Normalization 2
GyroBN	Gyrogroup Batch Normalization 2
LieBN	Lie Group Batch Normalization 2
RBN	Riemannian Batch Normalization 2
SPDBN	SPD Batch Normalization 2
PHCM	Poly-Hyperbolic-Cholesky Metric 9
ONB	Orthonormal Basis 7
PP	Projector Perspective 7
DNNs	Deep Neural Networks 1
FC	Fully Connected 30
MLR	Multinomial Logistics Regression 36
AIM	Affine-Invariant Metric 2
LCM	Log-Cholesky Metric 7
LEM	Log-Euclidean Metric 7
SPD	Symmetric Positive Definite 2

Appendix A. Notations

Table A.1 summarizes the key notations in the main paper.

Appendix B. Existence and Uniqueness of the Weighted Fréchet Mean

Let (\mathcal{M}, g) be an orientable complete Riemannian manifold equipped with a Riemannian metric g . The induced distance is denoted as $d(\cdot, \cdot)$. We denote the supremum of the sectional curvatures of \mathcal{M} by Δ . We recover the theorem on the existence and uniqueness of the Weighted Fréchet Mean (WFM) (Afsari, 2011). We acknowledge that Chakraborty et al. (2020, Appendix A) has also provided a summary of the following discussions.

Definition B.1 (Geodesic Ball (Do Carmo and Flaherty Francis, 1992)). Let $x \in \mathcal{M}$ and $r > 0$. Then $B_r(x) = \{y \in \mathcal{M} \mid d(x, y) < r\}$ is the open geodesic ball at x of radius r .

Definition B.2 (Injectivity Radius (Manton, 2004)). The local injectivity radius at $x \in \mathcal{M}$, $r_{\text{inj}}(x)$, is the largest radius r for which $\text{Exp}_P : T_P\mathcal{M} \supset B_r(\mathbf{0}) \rightarrow \mathcal{M}$ is a diffeomorphism onto its image. The injectivity radius of \mathcal{M} is defined as $r_{\text{inj}}(\mathcal{M}) = \inf_{x \in \mathcal{M}} \{r_{\text{inj}}(x)\}$.

Within the local injectivity radius, the exponential map is invertible and we call the inverse map as Riemannian logarithmic map, $\text{Log}_x : B_{r_{\text{inj}}(x)}(x) \rightarrow B_{r_{\text{inj}}(x)}(\mathbf{0}) \subset T_P\mathcal{M}$.

Definition B.3 (Strong Convexity (Chavel, 1995)). A subset $U \subset \mathcal{M}$ is strongly convex if for all $x, y \in U$, there exists a unique length-minimizing geodesic segment between x and y , and the geodesic segment lies entirely in U .

General notations	
(\mathcal{M}, g)	Riemannian manifold with metric g
$T_x\mathcal{M}$	Tangent space at $x \in \mathcal{M}$
$g_x(\cdot, \cdot), \langle \cdot, \cdot \rangle_x$	Riemannian metric at x ; $\ v\ _x = \sqrt{g_x(v, v)}$
$d(\cdot, \cdot)$	Geodesic distance on \mathcal{M}
$\text{Exp}_x, \text{Log}_x$	Riemannian exponential / logarithm at x
$f_{*,x}$	Differential of f at x
$\text{PT}_{x \rightarrow y}(\cdot)$	Parallel transport along the geodesic connecting x and y
FM, WFM	(Weighted) Fréchet mean under d
(G, \oplus, \odot)	Gyrovector space: \oplus gyroaddition, \odot scalar gyromultiplication
$e, \ominus x, \text{gyr}[x, y]$	Gyro identity, gyroinverse, gyration
$\langle \cdot, \cdot \rangle_{\text{gyr}}, \ \cdot\ _{\text{gyr}}, d_{\text{gyr}}(x, y)$	Gyro inner product, gyronorm, gyrodistance
$\mathbb{R}^n, \mathbb{R}^{n \times n}$	Euclidean vector / matrix spaces
$\langle \cdot, \cdot \rangle$	Standard (resp. Frobenius) inner product for vectors (resp. matrices)
$\ \cdot\ $	Norm induced by $\langle \cdot, \cdot \rangle$
$\mathbf{0}$	Zero vector or matrix
Matrix manifolds (SPD, Grassmannian, Correlation)	
$\mathcal{S}^n, \mathcal{S}_{++}^n$	Symmetric matrices, SPD matrices
I_n	$n \times n$ identity matrix
$\text{mexp}(\cdot), \text{mlog}(\cdot)$	Matrix exponential / logarithm
$\text{Chol}(\cdot), \text{Dlog}(\cdot)$	Cholesky decomposition; diagonal element-wise log
ψ_{LC}	$\psi_{\text{LC}} = \text{Dlog} \circ \text{Chol}$
$\oplus^{\text{AI}}, \oplus^{\text{LE}}, \oplus^{\text{LC}}$	SPD gyroaddition induced by AIM/LEM/LCM
$\text{Gr}(p, n), \widetilde{\text{Gr}}(p, n)$	Grassmannian (ONB / projector perspectives)
$I_{p,n}, \widetilde{I}_{p,n}$	Identity elements in ONB / projector perspectives
$\pi : \text{Gr}(p, n) \rightarrow \widetilde{\text{Gr}}(p, n)$	Isometry $U \mapsto UU^\top$
$\oplus^{\text{Gr}}, \ominus^{\text{Gr}}, \odot^{\text{Gr}}$	Grassmannian gyroaddition / inverse / scalar product (ONB)
$\overline{(\cdot)}$	PP logarithm at $\widetilde{I}_{p,n}$: $\text{Log}_{\widetilde{I}_{p,n}}(\cdot)$
$\text{Cor}^+(n)$	Full-rank correlation manifold
$\text{Cor}(\cdot)$	$\text{Cor}(\Sigma) = D(\Sigma)^{-1/2} \Sigma D(\Sigma)^{-1/2}$
Constant curvature spaces	
st_K^n	K -stereographic model (unifies \mathbb{P}_K^n for $K < 0$, \mathbb{R}^n for $K = 0$, \mathbb{D}_K^n for $K > 0$)
$\mathbb{P}_K^n, \mathbb{D}_K^n$	Poincaré ball ($K < 0$) and projected hypersphere ($K > 0$)
$\oplus_K, \ominus_K, \odot_K$	Stereographic gyroaddition / inverse / scalar product
\tan_K, \sin_K, \cos_K	Curvature-aware \tan_K, \sin_K, \cos_K
$\oplus_{\text{M}}, \ominus_{\text{M}}, \odot_{\text{M}}$	Möbius operations on \mathbb{P}_K^n
\mathcal{M}_K^n	K -radius model (unifies \mathbb{H}_K^n for $K < 0$, \mathbb{R}^n for $K = 0$, \mathbb{S}_K^n for $K > 0$)
$\mathbb{H}_K^n, \mathbb{S}_K^n$	Hyperboloid ($K < 0$) and sphere ($K > 0$)
$\langle \cdot, \cdot \rangle_K$	Euclidean inner product for $K > 0$ and Lorentz inner product for $K < 0$
$\ \cdot\ _K$	$\ x\ _K = \sqrt{\langle x, x \rangle_K}$
$\oplus_K^{\text{M}}, \ominus_K^{\text{M}}, \odot_K^{\text{M}}$	Radius gyroaddition / inverse / scalar product
$\mathbf{0}$	Origin of \mathcal{M}_K^n
$\pi_{\text{st}_K^n \rightarrow \mathcal{M}_K^n}, \pi_{\text{st}_K^n \rightarrow \mathcal{M}_K^n}$	Isometries between radius and stereographic models
λ_x^K	$\lambda_x^K = \frac{2}{(1+K\ x\ ^2)}$
\mathbb{K}_K^n	Beltrami–Klein model
$\oplus_{\text{E}}, \ominus_{\text{E}}, \odot_{\text{E}}$	Einstein addition / inverse / scalar product
$\pi_{\mathbb{K}_K^n \rightarrow \mathbb{P}_K^n}, \pi_{\mathbb{P}_K^n \rightarrow \mathbb{K}_K^n}$	Isometries between the Poincaré ball and Beltrami–Klein models
γ_x^K	$\gamma_x^K = \frac{1}{\sqrt{1+K\ x\ ^2}}$
$\text{HS}^n, \pi_{\text{HS}^n \rightarrow \mathbb{P}_1^{n-1}}$	Open hemisphere and its isometry to the unit Poincaré ball
$\mathbb{P}\mathbb{P}^{n-1} = \prod_{i=1}^{n-1} \mathbb{P}_1^i$	Product of unit Poincaré balls
$\pi_{\text{HS}^1 \rightarrow \mathbb{P}_1^1}$	Isometry from
Φ	Diffeomorphism from $\text{Cor}^+(n)$ to $\mathbb{P}\mathbb{P}^{n-1}$

Table A.1: Summary of key notations.

Definition B.4 (Convexity Radius (Groisser, 2004)). The local convexity radius at $x \in \mathcal{M}$, $r_{\text{cvx}}(x)$, is defined as

$$r_{\text{cvx}}(x) = \sup\{r \leq r_{\text{inj}}(x) \mid B_r(x) \text{ is strongly convex}\}. \quad (\text{B.1})$$

The convexity radius of \mathcal{M} is defined as $r_{\text{cvx}}(\mathcal{M}) = \inf_{x \in \mathcal{M}}\{r_{\text{cvx}}(x)\}$.

Theorem B.5 (Existence and Uniqueness of WFM (Afsari, 2011)). *The WFM exists and is unique inside a geodesic ball of radius $r_{\text{cvx}}(\mathcal{M})$.*

In the main paper, we always assume the involved Exp, Log, and WFM are well-defined.

Appendix C. Grassmannian GyroBN under the projector perspective

Given two isometric manifolds $\{\mathcal{M}_1, g^1\}$ and $\{\mathcal{M}_2, g^2\}$, the induced gyro-structures in Equation (1)-Equation (7) have the following relations. We first present a useful lemma.

Lemma C.6. *Given manifolds $\{\mathcal{M}_1, g^1\}$ and $\{\mathcal{M}_2, g^2\}$ and a Riemannian isometry $f : \mathcal{M}_1 \rightarrow \mathcal{M}_2$, we have the following:*

1. *The groupoid $\{\mathcal{M}_1, \oplus_1\}$ induced by g^1 is pseudo-reductive (left-invariant), iff the groupoid $\{\mathcal{M}_2, \oplus_2\}$ induced by g^2 is pseudo-reductive (left-invariant);*
2. *Any gyration in $\{\mathcal{M}_1, g^1\}$ preserves gyronorm iff any gyration in $\{\mathcal{M}_2, g^2\}$ preserves gyronorm;*
3. *f preserves the gyrodistance.*

Proof First, we review some facts about gyrogroups under the Riemannian isometry. As shown by Nguyen and Yang (2023, Theorem 2.5), $\{\mathcal{M}_1, \oplus_1\}$ satisfies (G1-G3) in Theorem 1 iff $\{\mathcal{M}_2, \oplus_2\}$ satisfies (G1-G3). Besides, f^{-1} is an isomorphism satisfying

$$f^{-1}(P \oplus_2 Q) = f^{-1}(P) \oplus_1 f^{-1}(Q), \quad (\text{C.1})$$

$$f^{-1}(t \odot_2 P) = t \oplus_1 f^{-1}(P), \quad (\text{C.2})$$

$$f^{-1}(\ominus_2 P) = \ominus_1 f^{-1}(P), \quad (\text{C.3})$$

$$\text{gyr}_2[P, Q](R) = f(\text{gyr}_1[f^{-1}(P), f^{-1}(Q)](f^{-1}(R))). \quad (\text{C.4})$$

where $P, Q, R \in \mathcal{M}_2$ are arbitrary points, $t \in \mathbb{R}$ is a real scalar, \ominus_i, gyr_i are the gyroinverses and gyrations on \mathcal{M}_i for $i = 1, 2$. f is also an isomorphism with similar properties.

We only need to prove one direction for the iff condition for the pseudo-reduction or norm invariance. We focus on \Rightarrow and follow the above notations in the following.

Pseudo-reduction:

$$\begin{aligned} \text{gyr}_2[\ominus P, P] &= f \circ \text{gyr}_1[f^{-1}(\ominus_2 P), f^{-1}(P)] \circ f^{-1} \quad (\text{Equation (C.4)}) \\ &= f \circ \text{gyr}_1[\ominus_1 f^{-1}(P), f^{-1}(P)] \circ f^{-1} \quad (\text{Equation (C.3)}) \\ &= \mathbb{1}. \end{aligned} \quad (\text{C.5})$$

Gyronorm invariance under gyrations: For simplicity, we denote the gyronorm, identity element, and Riemannian logarithm on \mathcal{M}_i as $\|\cdot\|_i, E_i$, and Log^i , respectively. First, the

following demonstrates that the Riemannian isometry f preserves gyronorm:

$$\begin{aligned}
 \|P\|_2 &= \|\text{Log}_{E_2}^2(P)\|_{E_2} \\
 &\stackrel{(1)}{=} \left\| \text{Log}_{f^{-1}(E_2)}^1(f^{-1}(P)) \right\|_{f^{-1}(E_2)} \\
 &\stackrel{(2)}{=} \|\text{Log}_{E_1}(f^{-1}(P))\|_{E_1} \\
 &= \|f^{-1}(P)\|_1
 \end{aligned} \tag{C.6}$$

(1) As $f : \mathcal{M}_1 \rightarrow \mathcal{M}_2$ is a Riemannian isometry, we have the following equations:

$$\text{Log}_P^2 Q = f_{*,f^{-1}(P)} \left(\text{Log}_{f^{-1}(P)}^1(f^{-1}(Q)) \right), \forall P, Q \in \mathcal{M}_2, \tag{C.7}$$

$$g_P^2(V, W) = g_{f^{-1}(P)}^1((f^{-1})_{*,P}(V), (f^{-1})_{*,P}(W)), \forall V, W \in T_P \mathcal{M}_2, \tag{C.8}$$

where $(\cdot)_*$ is the differential map;

(2) $E_2 = f(E_1)$.

Then we have the following:

$$\begin{aligned}
 \|\text{gyr}_2[P, Q](R)\|_2 &\stackrel{(1)}{=} \|f(\text{gyr}_1[f^{-1}(P), f^{-1}(Q)](f^{-1}(R)))\|_2 \\
 &\stackrel{(2)}{=} \|\text{gyr}_1[f^{-1}(P), f^{-1}(Q)](f^{-1}(R))\|_1 \\
 &\stackrel{(3)}{=} \|f^{-1}(R)\|_1 \\
 &\stackrel{(4)}{=} \|R\|_2
 \end{aligned} \tag{C.9}$$

The above derivation comes from the following.

- (1) Equation (C.4);
- (2) Equation (C.6);
- (3) Any gyration on \mathcal{M}_1 can preserve the gyronorm;
- (4) Equation (C.6).

Invariance of gyrodistance under f : Denoting the gyrodistance on \mathcal{M}_i as d_i , for any $U, V \in \mathcal{M}_1$, we have the following:

$$\begin{aligned}
 d_1(U, V) &= \|\ominus_1 U \oplus_1 V\|_1 \\
 &\stackrel{(1)}{=} \|f(\ominus_1 P \oplus_1 Q)\|_2 \\
 &\stackrel{(2)}{=} \|\ominus_1 f(P) \oplus_2 f(Q)\|_2 \\
 &= d_2(f(P), f(Q))_2
 \end{aligned} \tag{C.10}$$

The above derivation comes from the following.

- (1) f preserves gyronorm;

(2) f is an isomorphism. ■

Given a batch of activations $\{P_{1\dots N}\}$ on a gyrogroup $\{\mathcal{M}, \oplus\}$, we denote the GyroBN as

$$\text{GyroBN}(\{P_i\}; B, s, \epsilon, \eta), \quad (\text{C.11})$$

where $B \in \mathcal{M}$ and s are biasing and scaling parameters, ϵ is a small positive value, and η is the momentum.

Theorem C.7. *Given manifolds $\{\mathcal{M}_1, g^1\}$ and $\{\mathcal{M}_2, g^2\}$ and a Riemannian isometry $f : \mathcal{M}_1 \rightarrow \mathcal{M}_2$, for a batch of activation $\{P_{1\dots N}\}$ in \mathcal{M}_1 , $\text{GyroBN}_1(P_i; B, s, \epsilon, \gamma)$ in \mathcal{M}_1 can be calculated as*

$$\text{GyroBN}_1(P_i; B, s, \epsilon, \gamma) = f^{-1}(\text{GyroBN}_2(f(P_i); f(B), s, \epsilon, \gamma)), \quad (\text{C.12})$$

where GyroBN_2 is the GyroBN in \mathcal{M}_2 .

Proof This theorem is inspired by Chen et al. (2024b, Theorem 5.3), which characterizes the LieBNs under isometric manifolds. As gyrogroups are natural generalizations of Lie groups, our GyroBN is expected to have similar results. The following proof follows a similar logic to the one by Chen et al. (2024b, Theorem 5.3), except that all operations are gyro operations.

For $i = 1, 2$, we denote Equation (14) and binary gyro barycenter on \mathcal{M}_i as $\xi^i(\cdot | M, v^2, B, s)$ and $\text{Bar}_\eta^i(\cdot, \cdot)$. Let $\mathcal{B} = \{P_{1\dots N}\}$ and $f(\mathcal{B}) = \{f(P_{1\dots N})\}$. We only need to show the following:

$$M_2 = f(M_1), v_1 = v_2, \quad (\text{C.13})$$

$$\xi^1(P_i | M_1, v^2, B, s) = f^{-1}(\xi^2(f(P_i) | M_2, v^2, f(B), s)), \quad (\text{C.14})$$

$$\text{Bar}_\eta^1(P, Q) = f^{-1}(\text{Bar}_\eta^2(f(P), f(Q))), \forall P, Q \in \mathcal{M}_1. \quad (\text{C.15})$$

where M_i and v_i are the batch Fréchet mean and variance over \mathcal{M}_i for $i = 1, 2$. Equations (C.13) and (C.15) can be directly obtained by the invariance of gyrodistance under f (Theorem C.6). We only need to show Equation (C.14).

We have the following:

$$\begin{aligned} f^{-1}(\xi^2(f(P_i) | M_2, v^2, f(B), s)) &= f^{-1}(f(B) \oplus_2 (t \odot_2 (\ominus_2 M_2 \oplus_2 f(P_i)))) \\ &\stackrel{(1)}{=} f^{-1} \circ f(B \oplus_1 (t \odot (\ominus_1 M_1 \oplus_1 P_i))) \\ &= B \oplus_1 (t \odot (\ominus_1 M_1 \oplus_1 P_i)) \\ &= \xi^1(P_i | M, v^2, B, s), \end{aligned} \quad (\text{C.16})$$

where $t = \frac{s}{\sqrt{v^2 + \epsilon}}$. The above derivation comes from the following.

(1) f is an isomorphism preserving gyro operations.

■

As $\pi^{-1} : \widetilde{\text{Gr}}(p, n) \rightarrow \text{Gr}(p, n)$ is a Riemannian isometry, Theorem C.7 indicates that the GyroBN under the projector perspective can be calculated by the ONB perspective by the following process:

1. mapping data into the ONB perspective by $\pi^{-1} : \widetilde{\text{Gr}}(p, n) \rightarrow \text{Gr}(p, n)$;
2. normalizing data by the GyroBN under $\text{Gr}(p, n)$;
3. mapping normalized data back to $\widetilde{\text{Gr}}(p, n)$ by π .

Besides, both Theorem C.6 or Theorem 14 can guarantee theoretical control over the gyromean and gyrovariance under the projector perspective.

Appendix D. Experimental Details

D.1 Reviews of ManifoldNorm and LRBN

The key differences between Riemannian normalization methods lie in the way in which they implement centering, scaling, and biasing. We briefly review the corresponding formulations of ManifoldNorm (Chakraborty, 2020, Algorithm 1–2) and LRBN (Lou et al., 2020, Algorithm 2).

ManifoldNorm. Let $\{x_i\}_{i=1}^N \subset \mathcal{M}$ be a batch of activations and G the isometry group of the homogeneous Riemannian space \mathcal{M} . The core operations in ManifoldNorm are

$$\text{Centering: } x_i^1 = \text{Exp}_e(\text{PT}_{\mu \rightarrow e}(\text{Log}_\mu(P_i))), \quad (\text{D.1})$$

$$\text{Scaling: } x_i^2 = \text{Exp}_e(S(\text{Log}_e(x_i^1))), \quad (\text{D.2})$$

$$\text{Biasing: } x_i^3 = g \cdot x_i^2, \quad (\text{D.3})$$

where $\mu \in \mathcal{M}$ is the Fréchet batch mean, $g \in G$ is the bias parameter with \cdot denoting the group action, and S is a diagonal scaling matrix. Here, Equation (D.2) assumes the identification $T_e\mathcal{M} \cong \mathbb{R}^m$ with $m = \dim(\mathcal{M})$.

LRBN. Following the same notation, the core operation in LRBN is

$$x_i^1 = \text{Exp}_\beta \left(\frac{s}{v} \text{PT}_{\mu \rightarrow \beta}(\text{Log}_\mu(P_i)) \right), \quad (\text{D.4})$$

where v^2 is the Fréchet variance, s is the scaling parameter, and $\beta \in \mathcal{M}$ is the bias parameter.

D.2 Details on the Grassmannian Experiments

D.2.1 DATA SETS AND PREPROCESSING

*HDM05*¹³ (Müller et al., 2007). It consists of 2,273 skeleton-based motion capture sequences executed by different actors. Each frame records the 3D coordinates of 31 joints. We remove under-represented clips, trimming the data set down to 2,086 instances over 117 classes.

¹³. <https://resources.mpi-inf.mpg.de/HDM05/>

*NTU60*¹⁴ (Shahroudy et al., 2016). This data set contains 56,880 skeleton sequences classified into 60 classes, where each frame includes 3D coordinates of 25 or 50 joints. We focus on mutual actions and adopt the cross-view protocol (Shahroudy et al., 2016).

*NTU120*¹⁵ (Liu et al., 2019). This data set contains 114,480 sequences in 120 action classes. We again use mutual actions and adopt the cross-setup protocol (Liu et al., 2019).

Following Nguyen and Yang (2023), each sequence is represented as a Grassmannian matrix of size 93×10 , 150×10 , and 150×10 for HDM05, NTU60, and NTU120, respectively.

D.2.2 BASIC LAYERS IN GYROGR

GyroGr (Huang et al., 2018) mimics conventional densely connected feedforward networks and is composed of three basic building blocks. Given an ONB Grassmannian matrix U^{k-1} , the gyrotranslation and ProjMap layers are defined as

$$\text{Gyrotranslation: } U^k = W^k \oplus_{\text{Gr}} U^{k-1}, \quad W^k \in \text{Gr}(p, n), \quad (\text{D.5})$$

$$\text{ProjMap: } P^k = (U^{k-1})^\top U^{k-1}. \quad (\text{D.6})$$

In addition, the pooling is performed via the space of projection matrices. Specifically, Grassmannian data are first mapped to the space of projection matrices via the ProjMap layer. A standard mean pooling operation is applied to the resulting projection matrices. Finally, the pooled matrices are projected back to the ONB Grassmannian by SVD. The entire procedure can be expressed as

$$\begin{aligned} P^k &= f_p \left((U^{k-1})^\top U^{k-1} \right), \\ U^k &= O_{1:p}^k, \quad \text{where } P^k \stackrel{\text{SVD}}{:=} O^k \Sigma^k (O^k)^\top, \end{aligned} \quad (\text{D.7})$$

where f_p is a regular mean pooling.

D.2.3 TRIVIALIZATION

Following Nguyen and Yang (2023), we adopt the trivialization trick (Lezcano Casado, 2019) for the Grassmannian parameters in the gyrotranslation and our GyroBN layers. Each Grassmannian parameter $U \in \text{Gr}(p, n)$ is parameterized by a matrix $\mathfrak{U} \in \mathbb{R}^{(n-p) \times p}$ such that

$$\begin{bmatrix} 0 & -\mathfrak{U}^\top \\ \mathfrak{U} & 0 \end{bmatrix} = \left[\overline{UU^\top}, \tilde{I}_{p,n} \right].$$

where $\overline{(\cdot)} = \text{Log}_{\tilde{I}_{p,n}}(\cdot)$. The parameter U can be retrieved by

$$U = \text{mexp} \left(\left[\overline{UU^\top}, \tilde{I}_{p,n} \right] \right) I_{p,n} = \text{mexp} \left(\begin{bmatrix} 0 & -\mathfrak{U}^\top \\ \mathfrak{U} & 0 \end{bmatrix} \right) I_{p,n}. \quad (\text{D.8})$$

This reparameterization ensures that all variables lie in Euclidean space, thereby allowing the direct use of PyTorch optimizers (Paszke et al., 2019) and avoiding the additional computational burden of Riemannian optimization.

14. <https://github.com/shahroudy/NTURGB-D>

15. <https://github.com/shahroudy/NTURGB-D>

D.2.4 ANALYSIS ON THE EFFICIENCY OF GYROBN

As shown in Section 6.2.2, our Grassmannian GyroBN is more efficient than the ManifoldNorm (Chakraborty, 2020, Algorithm 1–2) or RBN (Lou et al., 2020, Algorithm 2). The key difference lies in their methods for centering, biasing, and scaling. GyroBN uses gyro operations, while ManifoldNorm and RBN rely on Riemannian operators, such as parallel transport and the Riemannian logarithmic and exponential maps. This distinction underpins the efficiency of GyroBN. The three primary contributing factors, ranked by importance, are as follows:

1. *Riemann vs. Gyro.* The Riemannian operators over the Grassmannian involve computationally expensive processes like SVD decomposition or matrix inversion (see Table 4 for Riemannian exp and log, and Edelman et al. (1998, Theorem 2.4) for parallel transport). Consequently, ManifoldNorm and RBN require multiple SVD or matrix inversion operations. In contrast, GyroBN is relatively simpler. As discussed in Section 5.3, the gyro operation can be further simplified, and the involved SVD is performed on a reduced $p \times p$ matrix instead of $n \times p$. Additionally, computationally intensive matrix exponentiation is efficiently approximated using the Cayley map.
2. *Reduced Matrix Products.* As shown in Table 4, each Riemannian operator involves several matrix products over $n \times p$ matrices. GyroBN reduces these to matrix products over $(n - p) \times p$ or $p \times p$ matrices, as shown in Theorem 19.
3. *Optimization.* The optimization of bias parameter in GyroBN is simpler. ManifoldNorm uses an $n \times n$ orthogonal matrix for biasing, and RBN employs an $n \times p$ Grassmannian matrix, both requiring Riemannian optimization. In contrast, GyroBN applies trivialization tricks (Equation D.8), making the bias parameter a $(n - p) \times p$ Euclidean matrix. Furthermore, Equation (D.8) and Equation (20) share a similar form, allowing them to be jointly simplified. Although RBN could adopt similar trivialization for biasing, this would introduce an additional Riemannian exp step, leaving little advantage over the Riemannian optimization. In summary, GyroBN benefits from joint simplification with trivialization, whereas the other two Grassmannian BN methods require additional Riemannian optimization.

D.3 Details on the Constant Curvature Space Experiments

D.3.1 DATA SETS

Cora (Sen et al., 2008). It is a citation network where the nodes represent scientific papers in the area of machine learning, the edges are citations between them, and the labels of the nodes are academic (sub)areas.

Disease (Anderson and May, 1991). It represents a disease propagation tree, simulating the SIR disease transmission model, with each node representing either an infection or a non-infection state.

Airport (Zhang and Chen, 2018). It is a transductive data set where nodes represent airports and edges represent airline routes as from OpenFlights.org.

Pubmed (Namata et al., 2012). This is a standard benchmark that describes citation networks where nodes represent scientific papers in the area of medicine, the edges are citations between them, and the node labels are academic (sub)areas.

D.3.2 BRIEF REVIEW OF HYPERBOLIC NEURAL NETWORKS

Hyperboloid Neural Networks. Let $x \in \mathbb{H}_K^n$ be the input vector and $W \in \mathbb{R}^{m \times n+1}, v \in \mathbb{R}^{n+1}$ the weight parameters. The Lorentz Fully-Connected (FC) layer (Chen et al., 2021, Equation 3) and activation layer (Bdeir et al., 2024, Equation 13) are defined in a spacetime manner:

$$\text{Activation: } y = \left[\begin{array}{c} \sqrt{\|\psi(x_s)\|^2 - 1/K} \\ \psi(x_s) \end{array} \right], \quad (\text{D.9})$$

$$\text{FC: } y = \left[\begin{array}{c} \sqrt{\|\phi(Wx, v)\|^2 - 1/K} \\ \phi(Wx, v) \end{array} \right], \quad (\text{D.10})$$

$$\text{with } \phi(Wx, v) = \lambda \sigma(v^T x + b') \frac{W\psi(x) + b}{\|W\psi(x) + b\|}, \quad (\text{D.11})$$

where ψ is an activation, $\lambda > 0$ is a learnable scaling parameter, and $b \in \mathbb{R}^n, \psi, \sigma$ denote the bias, activation, and sigmoid function, respectively.

Poincaré MLR. Lebanon and Lafferty (2004) first reformulated the Euclidean Multinomial Logistic Regression (MLR) $p(y=k | x) \propto \exp(\langle a_k, x \rangle - b_k)$ via the point-to-hyperplane distance:

$$p(y=k | x) \propto \exp(\text{sign}(\langle a_k, x \rangle - b_k) \|a_k\| d(x, H_{a_k, b_k})), \\ H_{a, b} = \{x \in \mathbb{R}^n : \langle a, x \rangle - b = 0\}, \quad \text{where } a \in \mathbb{R}^n, \text{ and } b \in \mathbb{R}.$$

Ganea et al. (2018, Equations 24–25) generalized this formulation to the Poincaré ball via geometric reinterpretation, and Shimizu et al. (2021, Section 3.1) further simplified it using trivialization. The resulting closed form is

$$v_k(x) = \frac{2\|z_k\|}{\sqrt{|K|}} \text{asinh} \left(\lambda_x^K \langle \sqrt{|K|}x, [z_k] \rangle \cosh(2\sqrt{|K|}r_k) - (\lambda_x^K - 1) \sinh(2\sqrt{|K|}r_k) \right),$$

where $\lambda_x^K = 2(1 - |K|\|x\|^2)^{-1}$ is the conformal factor, $p(y=k | x) \propto \exp(v_k(x))$, and $[z_k] = \frac{z_k}{\|z_k\|}$. Here, $z_k \in \mathbb{R}^n$ and $r_k \in \mathbb{R}$ are parameters. Note that $\lim_{K \rightarrow 0} v_k(x) = 4(\langle a_k, x \rangle - b_k)$.

Poincaré FC Layer. Shimizu et al. (2021) extended the Euclidean FC layer to the Poincaré ball via point-to-hyperplane distances. In Euclidean spaces, the FC can be written element-wise as $y_k = \langle a_k, x \rangle - b_k$ with $x, a_k \in \mathbb{R}^n$ and $b_k \in \mathbb{R}$, which may be interpreted as a linear transform whose output coordinate is the signed distance to the hyperplane passing through the origin and orthogonal to the k -th axis. Combining this view, the Poincaré FC layer takes the closed form:

$$y = \frac{w}{1 + \sqrt{1 + |K|\|w\|^2}}, \quad w_k = |K|^{-1/2} \sinh \left(\sqrt{|K|}v_k(x) \right),$$

where $c = |K|$ is the magnitude of the curvature. Here, $Z = \{z_k\}_{k=1}^m$ and $r = \{r_k\}_{k=1}^m$ parameterize the orientations and biases, and $v_k(x)$ is the Poincaré MLR.

Poincaré β -Concatenation. It generalizes the Euclidean concatenation into the hyperbolic Poincaré ball, stabilizing the norm of the Poincaré vector (Shimizu et al., 2021, Section 3.3). Given inputs $\{x_i \in \mathbb{P}_K^{n_i}\}_{i=1}^N$, it is defined as

$$\text{Exp}_{\mathbf{0}} \left(\beta_n \left(\beta_{n_1}^{-1} v_1^\top, \dots, \beta_{n_N}^{-1} v_N^\top \right) \right)^\top \in \mathbb{P}_K^n,$$

where $v_i = \text{Log}_{\mathbf{0}}(x_i)$, $n = \sum_{i=1}^N n_i$, and $\beta_\alpha = B(\alpha/2, 1/2)$ are the beta function.

RResNet. Euclidean residual blocks can be written as

$$x^{(i)} = x^{(i-1)} + n_i \left(x^{(i-1)} \right), \quad (\text{D.12})$$

where n_i is a network. Katsman et al. (2024) generalized this to manifolds by replacing addition with the Riemannian exponential map:

$$x^{(i)} = \text{Exp}_{x^{(i-1)}} \left(\ell_i(x^{(i-1)}) \right), \quad (\text{D.13})$$

where $\ell_i : \mathcal{M} \rightarrow T\mathcal{M}$ outputs a vector field parameterized by the neural network. As $\text{Exp}_x(v) = x + v$ for the Euclidean space, it can be immediately shown that Equation (D.13) naturally extends Equation (D.12) to manifolds.

D.4 Details on the Correlation Experiments

D.4.1 DATA SETS AND PREPROCESSING

HDM05. Please refer to Section D.2.

*Radar*¹⁶ (Brooks et al., 2019). It consists of 3,000 synthetic radar signals equally distributed in 3 classes.

*FPHA*¹⁷ (Garcia-Hernando et al., 2018). It includes 1,175 skeleton-based first-person hand gesture videos of 45 different categories with 600 clips for training and 575 for testing. Each frame contains the 3D coordinates of 21 hand joints.

For the HDM05 and FPHA data sets, we preprocess each sequence using the code¹⁸ provided by Vemulapalli et al. (2014) to normalize the lengths of the body parts and ensure invariance with scale and view.

D.4.2 CORRELATION INPUT IN CORNETS

Following Chen et al. (2025d), we model each sequence into multichannel correlation matrices. Specifically, according to Wang et al. (2024a); Nguyen et al. (2024), each sample is modeled as a multichannel SPD tensor. Then, each SPD matrix is transformed to their correlation matrix by

$$\text{Cor} : \mathcal{S}_{++}^n \ni \Sigma \mapsto C = \mathbb{D}(\Sigma)^{-\frac{1}{2}} \Sigma \mathbb{D}(\Sigma)^{-\frac{1}{2}} \in \text{Cor}^+(n).$$

16. <https://www.dropbox.com/s/dfnlx2bnyh3kjwy/data.zip?dl=0>

17. https://github.com/guiggh/hand_pose_action

18. <https://ravitejav.weebly.com/kbac.html>

After preprocessing, the input correlation tensor shapes are [7, 20, 20], [3, 28, 28], and [9, 28, 28] on the Radar, HDM05, and FPHA data sets, respectively. The following introduces SPD modeling.

HDM05 and FPHA. We first identify the closest left (right) neighbor of every joint based on their distance to the hip (wrist) joint, and then combine the 3D coordinates of each joint and those of its left (right) neighbor to create a feature vector for the joint. For a given frame t , we compute its Gaussian embedding (Lovrić et al., 2000):

$$Y_t = (\det \Sigma_t)^{-\frac{1}{n+1}} \begin{bmatrix} \Sigma_t + \mu_t (\mu_t)^T & \mu_t \\ (\mu_t)^T & 1 \end{bmatrix},$$

where μ_t and Σ_t are the mean vector and covariance matrix computed from the set of feature vectors within the frame. The lower part of the matrix $\log(Y_t)$ is flattened to obtain a vector \tilde{v}_t . All vectors \tilde{v}_t within a time window $[t, t + c - 1]$, where c is determined from a temporal pyramid representation of the sequence (the number of temporal pyramids is set to 2 in our experiments), are used to compute a covariance matrix:

$$\tilde{\Sigma}_t = \frac{1}{c} \sum_{i=t}^{t+c-1} (\tilde{v}_i - \bar{v}_t) (\tilde{v}_i - \bar{v}_t)^T,$$

where $\bar{v}_t = \frac{1}{c} \sum_{i=t}^{t+c-1} \tilde{v}_i$. The resulting $\{\tilde{\Sigma}_t\}$ are the covariance matrices that we need. On the FPHA data set, we generate covariance based on three sets of neighbors: left, right, and vertical (bottom) neighbors.

Radar. We follow (Wang et al., 2024a) to use the temporal convolution followed by a covariance pooling layer to obtain a multi-channel covariance tensor of shape $[c, 20, 20]$.

D.5 Hardware

All experiments are conducted on a single NVIDIA Quadro RTX A6000 48GB GPU.

Appendix E. Proofs

E.1 Proof of Theorem 7

Proof By Nguyen and Yang (2023, Lemma 2.3), easy computations show that Equation (9) holds for $\text{Gr}(p, n)$ iff it holds for $\widetilde{\text{Gr}}(p, n)$. Without loss of generality, we prove the case for the projector perspective.

Given any $P, Q \in \widetilde{\text{Gr}}(p, n)$, Definition 3.18 by Nguyen (2022a) gives the expression for gyration:

$$\text{gyr}[\ominus P, P]Q = F(\ominus P, P)Q(F(\ominus P, P))^{-1},$$

with $F(\ominus P, P)$ defined as

$$F(\ominus P, P) = \text{mexp} \left(- \left[\overline{\ominus P \oplus P}, \tilde{I}_{p,n} \right] \right) \text{mexp} \left(\left[\overline{\ominus P}, \tilde{I}_{p,n} \right] \right) \text{mexp} \left(\left[\overline{P}, \tilde{I}_{p,n} \right] \right),$$

where $\overline{(\cdot)} = \text{Log}_{\tilde{I}_{p,n}}(\cdot)$. This equation can be further simplified as

$$\begin{aligned} F(\ominus P, P) &\stackrel{(1)}{=} \text{mexp}(0) \text{mexp}\left(\left[\overline{\ominus P}, \tilde{I}_{p,n}\right]\right) \text{mexp}\left(\left[\overline{P}, \tilde{I}_{p,n}\right]\right) \\ &\stackrel{(2)}{=} \text{mexp}\left(\left[\overline{\ominus P}, \tilde{I}_{p,n}\right]\right) \text{mexp}\left(\left[\overline{P}, \tilde{I}_{p,n}\right]\right) \\ &\stackrel{(3)}{=} I_n. \end{aligned}$$

The above derivation follows from

- (1) $\overline{\ominus P} \oplus \overline{P} = \overline{\tilde{I}_{p,n}} = 0 \in \mathbb{R}^{n \times n}$.
- (2) $\text{mexp}(0) = I_n$.
- (3) $\overline{\ominus P} = -\overline{P}$ and $\text{mexp}\left(\left[-\overline{P}, \tilde{I}_{p,n}\right]\right) = \text{mexp}\left(\left[\overline{P}, \tilde{I}_{p,n}\right]\right)^{-1}$.

Therefore, $\text{gyr}[\ominus P, P]$ is the identity map. ■

E.2 Proof of Theorem 8

Proof This theorem follows (Ungar, 2022, Theorems. 2.10–2.11), which presents some useful properties for gyrogroups. We argue that all the properties except $\text{gyr}[a, a] = \mathbb{1}$ are independent of the left reduction law (G4), and are therefore satisfied on pseudo-reductive gyrogroups. All the properties can be proven in the same way as the ones for Theorems. 2.10–2.11 by Ungar (2022). We summarize the logic in the following:

- left gyroassociativity $\Rightarrow 1$
- left gyroassociativity + 1 $\Rightarrow 2$
- definition $\Rightarrow 3$
- left gyroassociativity + 1 + 3 $\Rightarrow 4$
- definition $\Rightarrow 5$
- left gyroassociativity + (G2) + 1 + 3 + 4 + 5 $\Rightarrow 6$
- 1+6 $\Rightarrow 7$
- left gyroassociativity + 3 $\Rightarrow 8$
- left gyroassociativity + left cancellation in 8 $\Rightarrow 9$
- gyro identity in 9 $\Rightarrow 10$
- 10 $\Rightarrow 11$
- left cancellation in 8 + gyro identity in 9 $\Rightarrow 12$
- left cancellation in 8 + gyro identity in 9 $\Rightarrow 13$

■

E.3 Proof of Theorem 10

Proof

$$\begin{aligned}
 y &\stackrel{(1)}{=} x \oplus (\ominus x \oplus y) \\
 &\stackrel{(2)}{=} \text{Exp}_x(\text{PT}_{e \rightarrow x}(\text{Log}_e(\ominus x \oplus y))) \\
 &\stackrel{(3)}{\Rightarrow} \text{Log}_x(y) = \text{PT}_{e \rightarrow x}(\text{Log}_e(\ominus x \oplus y)).
 \end{aligned} \tag{E.1}$$

The above comes from the following.

- (1) Left cancellation law.
- (2) Definition of gyroaddition.
- (3) Applying both sides with $\text{Log}_x(\cdot)$.

By the last equation, we have

$$\begin{aligned}
 d(x, y) &= \|\text{Log}_x(y)\|_x \\
 &= \|\text{PT}_{e \rightarrow x}(\text{Log}_e(\ominus x \oplus y))\|_x \\
 &\stackrel{(1)}{=} \|\text{Log}_e(\ominus x \oplus y)\|_e \\
 &= d_{\text{gyr}}(x, y),
 \end{aligned} \tag{E.2}$$

where (1) comes from

- Parallel transport preserving the norm (Do Carmo and Flaherty Francis, 1992, Section 3.1).
- $\text{PT}_{x \rightarrow e} \circ \text{PT}_{e \rightarrow x}(v) = v, \forall v \in T_e \mathcal{M}$.

■

E.4 Proof of Theorem 11

Proof We denote Log , gyr and $\|\cdot\|_{\text{gyr}}$ as the Riemannian logarithm and gyronorm on $\{\mathcal{M}, g\}$, while $\widetilde{\text{Log}}$, $\widetilde{\text{gyr}}$ and $\|\cdot\|_{\widetilde{\text{gyr}}}$ are the counterparts on $\{\widetilde{\mathcal{M}}, \widetilde{g}\}$. We recall the following from Nguyen and Yang (2023, Lemmas 2.1–2.3):

$$x \oplus y = \phi^{-1}(\phi(x) \widetilde{\oplus} \phi(y)), \tag{E.3}$$

$$t \otimes x = \phi^{-1}(t \widetilde{\otimes} \phi(x)), \tag{E.4}$$

$$\text{gyr}[x, y]z = \phi^{-1}(\widetilde{\text{gyr}}[\phi(x), \phi(y)]\phi(z)), \tag{E.5}$$

where $x, y, z \in \mathcal{M}$.

Gyrodistance.

$$\begin{aligned}
 \widetilde{d}_{\text{gyr}}(\phi(x), \phi(y)) &= \|\widetilde{\Theta}\phi(x)\widetilde{\Theta}\phi(y)\|_{\widetilde{\text{gyr}}} \\
 &\stackrel{(1)}{=} \|\phi(\Theta x \oplus y)\|_{\widetilde{\text{gyr}}} \\
 &= \left\langle \widetilde{\text{Log}}_{\widetilde{e}}(\phi(\Theta x \oplus y)), \widetilde{\text{Log}}_{\widetilde{e}}(\phi(\Theta x \oplus y)) \right\rangle_{\widetilde{e}} \\
 &\stackrel{(2)}{=} \langle \text{Log}_e(\Theta x \oplus y), \text{Log}_e(\Theta x \oplus y) \rangle_e \\
 &= \|\Theta x \oplus y\|_{\text{gyr}} \\
 &= d_{\text{gyr}}(x, y).
 \end{aligned}$$

The derivation above comes from the following.

(1) By Equations (E.3) and (E.4):

$$\phi(\Theta x \oplus y) = \phi(\Theta x)\widetilde{\Theta}\phi(y).$$

(2) By the isometry:

$$\begin{aligned}
 \text{Log}_x(y) &= (\phi_{*,x})^{-1} \left(\widetilde{\text{Log}}_{\phi(x)}(\phi(y)) \right), \forall x, y \in \mathcal{M}, \\
 \langle v, w \rangle_x &= \langle \phi_{*,x}(v), \phi_{*,x}(w) \rangle_{\phi(x)}, \forall x \in \mathcal{M} \text{ and } \forall v, w \in T_x\mathcal{M},
 \end{aligned}$$

where $\phi_{*,x}$ is the differential map. Here, the RHSs contain the operators over $\widetilde{\mathcal{M}}$, where the LHSs involve the ones over \mathcal{M} .

Gyroisometry. Given any $x, y, z, a \in \mathcal{M}$, we have the following by the isometry of ϕ .

For the gyroinverse:

$$\begin{aligned}
 d_{\widetilde{\text{gyr}}}(\widetilde{\Theta}\phi(x), \widetilde{\Theta}\phi(y)) &= d_{\widetilde{\text{gyr}}}(\phi(\Theta x), \phi(\Theta y)) \\
 &= d_{\text{gyr}}(\Theta x, \Theta y) \\
 &= d_{\text{gyr}}(x, y) \\
 &= d_{\widetilde{\text{gyr}}}(\phi(x), \phi(y)).
 \end{aligned}$$

For the gyration:

$$\begin{aligned}
 d_{\widetilde{\text{gyr}}}(\widetilde{\text{gyr}}[\phi(z), \phi(a)]\phi(x), \widetilde{\text{gyr}}[\phi(z), \phi(a)]\phi(y)) \\
 &= d_{\widetilde{\text{gyr}}}(\phi(\text{gyr}[z, a]x), \phi(\text{gyr}[z, a]y)) \\
 &= d_{\text{gyr}}(\text{gyr}[z, a]x, \text{gyr}[z, a]y) \\
 &= d_{\text{gyr}}(x, y) \\
 &= d_{\widetilde{\text{gyr}}}(\phi(x), \phi(y)).
 \end{aligned}$$

For the left gyrotranslation:

$$\begin{aligned}
 d_{\widetilde{\text{gyr}}}(\phi(z)\widetilde{\Theta}\phi(x), \phi(z)\widetilde{\Theta}\phi(y)) \\
 &= d_{\widetilde{\text{gyr}}}(\phi(z \oplus x), \phi(z \oplus y)) \\
 &= d_{\text{gyr}}(z \oplus x, z \oplus y) \\
 &= d_{\text{gyr}}(x, y) \\
 &= d_{\widetilde{\text{gyr}}}(\phi(x), \phi(y)).
 \end{aligned}$$

■

E.5 Proof of Theorem 12

We first prove a useful lemma.

Lemma E.8 (Left Gyrotranslation Law). *Every pseudo-reductive gyrogroup $\{G, \oplus\}$ verifies the left gyrotranslation law:*

$$\ominus(x \oplus y) \oplus (x \oplus z) = \text{gyr}[x, y](\ominus y \oplus z), \quad \forall x, y, z \in G.$$

Proof This lemma generalizes Lemmas I.1 and L.1 by Nguyen and Yang (2023), which prove the left gyrotranslation law on the specific gyrogroups of the SPD and Grassmannian manifolds. Their proof only relies on the left cancellation and the basic axioms (G1-3). Note that the original proof of left gyrotranslation on the Grassmannian (Nguyen and Yang, 2023, Lemma I.1) is questionable, as it relies on the left cancellation of gyrogroups, and the Grassmannian is not a gyrogroup but a non-reductive gyrogroup. Fortunately, as we show in Theorem 8, the general pseudo-reductive gyrogroups, including the Grassmannian, enjoy left cancellation. Therefore, all the proof by Nguyen and Yang (2023, Lemma I.1) can be readily generalized into the general pseudo-reductive gyrogroups. ■

Proof [Proof of Theorem 12] \Rightarrow : For any $z, a \in G$, the gyroautomorphism can be expressed by the gyrator identity in Theorem 8:

$$\begin{aligned} \text{gyr}[x, y]z &= X \oplus \bar{z}, \\ \text{gyr}[x, y]a &= X \oplus \bar{a}, \end{aligned}$$

where $X = \ominus(x \oplus y)$, $\bar{z} = x \oplus (y \oplus z)$, and $\bar{a} = x \oplus (y \oplus a)$. Then Equation (30) in (Nguyen and Yang, 2023) for the specific Grassmannian can be directly extended into the pseudo-reductive gyrogroup, as it only relies on left gyrotranslation, invariance of the norm under gyroautomorphisms, and the axioms of (G1-G3).

\Leftarrow :

$$\begin{aligned} \|\text{gyr}[x, y](z)\|_{\text{gyr}} &= \|\text{gyr}[x, y](\ominus e \oplus z)\|_{\text{gyr}} \quad (7 \text{ in Theorem 8 indicates } \ominus e = e) \\ &= \|\ominus \text{gyr}[x, y](e) \oplus \text{gyr}[x, y](z)\|_{\text{gyr}} \quad (\text{automorphism}) \\ &= d(\text{gyr}[x, y](e), \text{gyr}[x, y](z)) \\ &= d(e, z) \\ &= \|\ominus e \oplus z\|_{\text{gyr}} \\ &= \|z\|_{\text{gyr}}. \end{aligned}$$

■

E.6 Proof of Theorem 13

Proof Given any $x, y, z \in G$, we make the following proof.

Gyrometry of the Left Gyrotranslation. This property generalizes Theorems 2.12 and 2.16 by Nguyen and Yang (2023), which deal with the gyrotranslation in the SPD and Grassmannian, respectively. We have the following:

$$\begin{aligned}
 d(L_x(y), L_x(z)) &= d(x \oplus y, x \oplus z) \\
 &= \|\ominus(x \oplus y) \oplus (x \oplus z)\|_{\text{gyr}} \\
 &= \|\text{gyr}[x, y](\ominus y \oplus z)\|_{\text{gyr}} \quad (\text{left gyrotranslation law}) \\
 &= \|\ominus y \oplus z\|_{\text{gyr}} \quad (\text{gyrometry of the automorphism}) \\
 &= d(y, z).
 \end{aligned}$$

Gyrometry of the Gyroinverse.

$$\begin{aligned}
 d(\ominus x, \ominus y) &= \|x \ominus y\|_{\text{gyr}} \\
 &= \|\ominus y \oplus x\|_{\text{gyr}} \quad (\text{gyrocommutativity and gyrometry of the automorphism}) \\
 &= d(y, x) \\
 &= d(x, y) \quad (\text{Symmetry of the geodesic distance}).
 \end{aligned}$$

■

E.7 Proof of Theorem 14

Different from our conference version (Chen et al., 2025c, Appendix G.4), we give a much more concise argument based on Theorems 10, 12 and 13.

Proof First, all these gyrospaces are characterized by Equations (1) and (2). By Theorem 10, their gyrodistances agree with the geodesic distances. It thus remains to establish the gyrometries.

As shown by Theorems 12 and 13, it suffices to show that gyrations in each space preserve the gyronorm. This argument on the SPD and ONB Grassmannian has already been proven (Nguyen and Yang, 2023, Lemmas L.2 and I.2). Since the ONB Grassmannian is isometric to the PP Grassmannian via Equation (8), Theorem 11 implies that the same arguments apply for the PP. We therefore only need to treat \mathfrak{st}_K^n with $K \leq 0$. As the Euclidean case \mathbb{R}^n is trivial, we only need to show the Poincaré ball. In the following, a, b, x, y are arbitrary points in \mathbb{P}_K^n .

Norm Invariance under Gyration. As the Poincaré ball forms a real inner product gyrovector spaces (Ungar, 2022, Definition 6.2 and Theorem 6.85), any gyration preserves the Euclidean norm:

$$\|\text{gyr}[a, b](x)\| = \|x\|, \quad \forall x \in \mathfrak{st}_K^n.$$

For the gyronorm, we further have

$$\begin{aligned}
 \|\text{gyr}[a, b]x\|_{\text{gyr}} &= 2\|\text{Log}_{\mathbf{0}}(\text{gyr}[a, b]x)\|_{\mathbf{0}} \\
 &= \frac{2}{\sqrt{|K|}} \tanh^{-1}\left(\sqrt{|K|} \|\text{gyr}[a, b]x\|\right) \\
 &= \frac{2}{\sqrt{|K|}} \tanh^{-1}\left(\sqrt{|K|} \|x\|\right) \\
 &= \|x\|_{\text{gyr}}.
 \end{aligned}$$

■

E.8 Proof of Theorem 16

Proof According to Theorem 13, any left gyrotranslation is a gyroisometry. For any $y \in \mathcal{M}$, we have the following:

$$\begin{aligned}
 d(\beta \oplus x_i, y) &\stackrel{(1)}{=} d(\ominus\beta \oplus (\beta \oplus x_i), \ominus\beta \oplus y) \\
 &\stackrel{(2)}{=} d((\ominus\beta \oplus \beta) \oplus \text{gyr}[\ominus\beta, \beta](x_i), \ominus\beta \oplus y) \\
 &\stackrel{(3)}{=} d(x_i, \ominus\beta \oplus y).
 \end{aligned} \tag{E.6}$$

The above comes from the following.

- (1) Any left gyrotranslation is a gyroisometry.
- (2) Left gyroassociative law.
- (3) $\ominus\beta \oplus \beta = e$ and pseudo-reduction.

Denoting the gyromean of $\{x_i\}$ and $\{\beta \oplus x_i\}$ as μ and $\tilde{\mu}$, we have the following:

$$\begin{aligned}
 \beta \oplus \mu &\stackrel{(1)}{=} \beta \oplus (\ominus\beta \oplus \tilde{\mu}) \\
 &\stackrel{(2)}{=} \text{gyr}[\beta, \ominus\beta](\tilde{\mu}) \\
 &\stackrel{(3)}{=} \tilde{\mu}.
 \end{aligned} \tag{E.7}$$

The above comes from the following.

- (1) Equation (E.6) indicates that $\mu = \ominus\beta \oplus \tilde{\mu}$.
- (2) Left gyroassociative law.
- (3) Pseudo-reduction.

Algorithm 2: ONB Grassmann logarithm (Bendokat et al., 2024, Algorithm 5.3)

Input: $U, Y \in \text{Gr}(p, n)$ are Stiefel representatives under ONB perspective.

- 1 $QSR^T \stackrel{\text{SVD}}{:=} Y^T U$ with S in ascending order, and Q and R column-wisely flipped accordingly;
- 2 $\hat{S} = \sqrt{I_n - S^2}$;
- 3 $\Delta = (I_n - UU^\top)YQ \frac{\arcsin(\hat{S})}{\hat{S}} R^T$;

Output: $\text{Log}_U(Y) = \Delta$

Now, we proceed to deal with the second property. We have the following:

$$\begin{aligned}
 d(t \odot x_i, e) &\stackrel{(1)}{=} \|\ominus e \oplus (t \odot x_i)\|_{\text{gyr}} \\
 &\stackrel{(2)}{=} \|t \odot x_i\|_{\text{gyr}} \\
 &= \|t \text{Log}_e(x_i)\|_e \\
 &= |t| \|\text{Log}_e(x_i)\|_e \\
 &= |t| \|x_i\|_{\text{gyr}} \\
 &\stackrel{(3)}{=} |t| \|\ominus e \oplus x_i\|_{\text{gyr}} \\
 &= |t| d(e, x_i) \\
 &\stackrel{(4)}{=} |t| d(x_i, e)
 \end{aligned} \tag{E.8}$$

The above follows from the following.

- (1) Symmetry of gyrodistance (as geodesic distance).
- (2) $\ominus e = e$.
- (3) $x_i = \ominus e \oplus x_i$.
- (4) Symmetry of gyrodistance (as geodesic distance).

The last equation in Equation (E.8) indicates the homogeneity of dispersion from e . ■

E.9 Proof of Theorem 19

We first review a fast and stable algorithm for the ONB Grassmannian logarithm (Bendokat et al., 2024, Algorithm 5.3), and the calculation of Grassmannian logarithm under the projector perspective by the ONB Grassmannian logarithm (Nguyen et al., 2024, Proposition 3.12).

Algorithm 2 reviews a fast and stable algorithm for the Grassmannian Riemannian logarithm under the ONB perspective $\text{Gr}(p, n)$. The vanilla Riemannian logarithm in Table 4 requires an $n \times p$ SVD and a $p \times p$ matrix inverse, while Algorithm 2 only requires an $p \times p$ SVD. Therefore, Algorithm 2 is more efficient than the vanilla logarithm. Besides, Algorithm 2 can

also return a unique tangent vector when Y is in the cut locus of U . For more details, please refer to Bendokat et al. (2024, Section 5.2).

As the projector perspective is isometric to the ONB perspective, the Grassmannian logarithm under the projector perspective can be calculated by the ONB Grassmannian logarithm (Nguyen et al., 2024, Proposition 3.12).

Proposition E.9 ((Nguyen et al., 2024)). *Given any $P, Q \in \widetilde{\text{Gr}}(p, n)$ with $U = \pi^{-1}(P)$ and $V = \pi^{-1}(Q)$, the Riemannian logarithm $\widetilde{\text{Log}}_P(Q)$ on $\widetilde{\text{Gr}}(p, n)$ is given as*

$$\widetilde{\text{Log}}_P(Q) = \pi_{*,U}(\text{Log}_U V),$$

where Log is the Riemannian logarithm under the ONB perspective, $\pi_{*,U} : T_U \text{Gr}(p, n) \rightarrow T_P \widetilde{\text{Gr}}(p, n)$ is the differential map of π at U , which is defined as

$$\pi_{*,U}(\Delta) = \Delta U^\top + U \Delta^\top, \forall \Delta \in T_U \text{Gr}(p, n).$$

Now, we begin to present the proof.

Proof [Proof of Theorem 19] We first show the expression for $\text{Log}_{I_{p,n}}$ and $\widetilde{\text{Log}}_{\widetilde{I}_{p,n}}$.

First note the following:

$$\begin{aligned} (I_n - I_{p,n} I_{p,n}^\top) &= \begin{pmatrix} 0 & 0 \\ 0 & I_{n-p} \end{pmatrix}, \\ U^\top I_{p,n} &= (U_1^\top, U_2^\top) \begin{pmatrix} I_p \\ 0 \end{pmatrix} \\ &= U_1^\top, \end{aligned}$$

By the above two equations, the ONB Grassmannian logarithm at $I_{p,n}$ is

$$\begin{aligned} \text{Log}_{I_{p,n}}(U) &= \begin{pmatrix} 0 & 0 \\ 0 & I_{n-p} \end{pmatrix} \begin{pmatrix} U_1 \\ U_2 \end{pmatrix} Q \frac{\arcsin(\hat{S})}{\hat{S}} R^\top \quad (\text{Algorithm 2}) \\ &= \begin{pmatrix} 0 \\ U_2 Q \frac{\arcsin(\hat{S})}{\hat{S}} R^\top \end{pmatrix} \\ &= \begin{pmatrix} 0 \\ \widetilde{U}_2 \end{pmatrix}, \end{aligned} \tag{E.9}$$

where $QSR^\top \stackrel{\text{SVD}}{:=} U_1^\top$ with S in ascending order, and Q and R column-wisely flipped accordingly, and $\hat{S} = \sqrt{I_n - S^2}$.

For $\widetilde{\text{Log}}_{\widetilde{I}_{p,n}}$, we have

$$\begin{aligned} \widetilde{\text{Log}}_{\widetilde{I}_{p,n}}(UU^\top) &\stackrel{(1)}{=} \pi_{*,I_{p,n}}(\text{Log}_{I_{p,n}}(U)) \\ &\stackrel{(2)}{=} \pi_{*,I_{p,n}}\left(\begin{pmatrix} 0 \\ \widetilde{U}_2 \end{pmatrix}\right) \\ &\stackrel{(3)}{=} \begin{pmatrix} 0 & \widetilde{U}_2^\top \\ \widetilde{U}_2 & 0 \end{pmatrix}. \end{aligned}$$

The above derivation comes from the following.

- (1) Theorem E.9
- (2) Equation (E.9)
- (3) For any $\Delta = (\Delta_1^\top, \Delta_2^\top)^\top \in T_{I_{p,n}} \text{Gr}(p, n)$, where Δ_1 is $p \times p$, we have the following

$$\begin{aligned}
 \pi_{*, I_{p,n}} \left(\begin{pmatrix} \Delta_1 \\ \Delta_2 \end{pmatrix} \right) &= \begin{pmatrix} \Delta_1 \\ \Delta_2 \end{pmatrix} (I_p, 0) + \begin{pmatrix} I_p \\ 0 \end{pmatrix} (\Delta_1^\top, \Delta_2^\top) \\
 &= \begin{pmatrix} \Delta_1 & 0 \\ \Delta_2 & 0 \end{pmatrix} + \begin{pmatrix} \Delta_1^\top & \Delta_2^\top \\ 0 & 0 \end{pmatrix} \\
 &= \begin{pmatrix} \Delta_1 + \Delta_1^\top & \Delta_2^\top \\ \Delta_2 & 0 \end{pmatrix}.
 \end{aligned}$$

Combining all the above results together, we have the following:

$$\begin{aligned}
 [\overline{UU^\top}, \tilde{I}_{p,n}] &= [\widetilde{\text{Log}}_{\tilde{I}_{p,n}}(UU^\top), \tilde{I}_{p,n}] \\
 &= \left[\begin{pmatrix} 0 & \tilde{U}_2^\top \\ \tilde{U}_2 & 0 \end{pmatrix}, \tilde{I}_{p,n} \right] \\
 &= \begin{pmatrix} 0 & \tilde{U}_2^\top \\ \tilde{U}_2 & 0 \end{pmatrix} \begin{pmatrix} I_p & 0 \\ 0 & 0 \end{pmatrix} - \begin{pmatrix} I_p & 0 \\ 0 & 0 \end{pmatrix} \begin{pmatrix} 0 & \tilde{U}_2^\top \\ \tilde{U}_2 & 0 \end{pmatrix} \\
 &= \begin{pmatrix} 0 & -\tilde{U}_2^\top \\ \tilde{U}_2 & 0 \end{pmatrix}.
 \end{aligned}$$

■

E.10 Proof of Theorem 21

Proof Given $v \in T_{\mathbf{0}} \text{st}_K^n$, we have the following:

$$\begin{aligned}
 \lambda_{\mathbf{0}}^K &= 2, \\
 \text{Log}_{\mathbf{0}}(y) &= \tan_K^{-1} \left(\sqrt{|K|} \|y\| \right) \frac{y}{\sqrt{|K|} \|y\|}, \\
 \text{PT}_{\mathbf{0} \rightarrow x}(v) &= \frac{\lambda_{\mathbf{0}}^K}{\lambda_x^K} \text{gyr}[y, -\mathbf{0}](v) = \frac{2}{\lambda_x^K} v, \\
 \text{Exp}_{\mathbf{0}}(v) &= \tan_K \left(\sqrt{|K|} \|v\| \right) \frac{v}{\sqrt{|K|} \|v\|}.
 \end{aligned}$$

Therefore, we have

$$\begin{aligned}
 \text{Exp}_x(\text{PT}_{\mathbf{0} \rightarrow x}(\text{Log}_{\mathbf{0}}(y))) &= \text{Exp}_x \left(\frac{2}{\sqrt{|K|} \lambda_x^K} \tan_K^{-1} \left(\sqrt{|K|} \|y\| \right) \frac{y}{\|y\|} \right) \\
 &= x \oplus_K y,
 \end{aligned}$$

which implies

$$\text{Exp}_{\mathbf{0}}(t \text{Log}_{\mathbf{0}}(x)) = t \odot_K x.$$

■

E.11 Proof of Theorem 22

Proof As discussed in the main paper, we always assume the gyro operations are well-defined. We only need to show the case of $K > 0$. Let x, y, z, w be any vectors in \mathfrak{st}_K^n , and $s, t \in \mathbb{R}$ be real scalars.

We first notice the gyroaddition is a linear combination:

$$x \oplus_K y = \frac{(1 - 2K \langle x, y \rangle - K \|y\|^2)x + (1 + K \|x\|^2)y}{1 - 2K \langle x, y \rangle + K^2 \|x\|^2 \|y\|^2} = \frac{Ax + By}{D},$$

where

$$\begin{aligned} A &= 1 - 2K \langle x, y \rangle - K \|y\|^2, \\ B &= 1 + K \|x\|^2, \\ D &= 1 - 2K \langle x, y \rangle + K^2 \|x\|^2 \|y\|^2. \end{aligned} \tag{E.10}$$

Recalling Equation (21), the gyration $\text{gyr}[x, y](z)$ is also a linear expression:

$$\text{gyr}[x, y](z) = z + f_1 \cdot x + f_2 \cdot y.$$

Axioms G1-G3. Noting that $e = \mathbf{0}$ and $\ominus_K x = -x$, G1 and G2 can be immediately verified. The left gyroassociative law follows from the definition of gyration (Bachmann et al., 2020, Equation 36):

$$\text{gyr}[x, y](z) = -(x \oplus_K y) \oplus_K (x \oplus_K (y \oplus_K z)).$$

To confirm that any gyration is an automorphism of $(\mathfrak{st}_K^n, \oplus_K)$, we verify the the following identity using symbolic computation:

$$\text{gyr}[x, y](w \oplus_K z) = \text{gyr}[x, y](w) \oplus_K \text{gyr}[x, y](z). \tag{E.11}$$

Expanding all necessary inner products (e.g., $\langle x, w \oplus_K z \rangle$, $\langle y, w \oplus_K z \rangle$) and norms in terms of $\langle x, w \rangle$, $\langle x, z \rangle$, etc., we express the both sides of Equation (E.11) as linear combinations:

$$\begin{aligned} \text{gyr}[x, y](w \oplus_K z) &= f_1 x + f_2 y + f_3 w + f_4 z, \\ \text{gyr}[x, y](w) \oplus_K \text{gyr}[x, y](z) &= f'_1 x + f'_2 y + f'_3 w + f'_4 z. \end{aligned}$$

We use `SymPy` to compare the coefficients of x , y , w , and z on both sides. The above is exposed in `stereographic_gyr_automorphism.py`.

(G4) Left Reduction Law. Similarly, we expand $\text{gyr}[x \oplus_K z, y](w)$ and $\text{gyr}[x, y](w)$ and compare the coefficients, as implemented in `stereographic_left_reduction.py`.

Gyrocommutative Law. This has been verified by Bachmann et al. (2020, Lemma 11).

(V1) *Identity Scalar Multiplication.* This can be directly verified by definition:

$$t \odot_K x = \frac{\tan(t \tan^{-1}(\sqrt{-K} \|x\|))}{\sqrt{-K}} \frac{x}{\|x\|}, \forall x \neq 0.$$

(V2) *Scalar Distributive Law.* We want to verify

$$(s + t) \odot_K x = (s \odot_K x) \oplus_K (t \odot_K x). \quad (\text{E.12})$$

We only need to show the case of $x \neq \mathbf{0}$. Let $\theta = \tan^{-1}(\sqrt{K} \|x\|)$. Then scalar multiplication is simplified as

$$t \odot_K x = \frac{\tan(t\theta)}{\sqrt{K} \|x\|} x.$$

Using symbolic computation (see `stereographic_gyr_v2.py`), we obtain the following w.r.t. Equation (E.12):

$$\begin{aligned} \text{LHS} &= \frac{\tan((s+t)\theta)}{\sqrt{K} \|x\|}, \\ \text{RHS} &= \frac{\tan(s\theta) + \tan(t\theta)}{\sqrt{K} \|x\| (1 - \tan(s\theta)\tan(t\theta))}. \end{aligned}$$

The identity follows from the tangent addition formula:

$$\tan((s+t)\theta) = \frac{\tan(s\theta) + \tan(t\theta)}{1 - \tan(s\theta)\tan(t\theta)}.$$

(V3) *Scalar Associative Law.* This can be directly verified by definition.

(V4) *Gyroautomorphism.* We now verify

$$\text{gyr}[x, y](t \odot_K z) = t \odot_K \text{gyr}[x, y](z). \quad (\text{E.13})$$

Let us denote

$$\alpha_t^{(z)} = \frac{\tan\left(t \tan^{-1}\left(\sqrt{K} \|z\|\right)\right)}{\sqrt{K} \|z\|}.$$

By the linearity of gyration (Bachmann et al., 2020, Lemma 11), the left-hand side of Equation (E.13) becomes

$$\text{LHS} = \alpha_t^{(z)} \text{gyr}[x, y](z),$$

while the right-hand side reads

$$\text{RHS} = \alpha_t^{\text{gyr}[x, y](z)} \text{gyr}[x, y](z).$$

Since $\alpha_t^{(\cdot)}$ depends only on the norm of its argument, it suffices to show

$$\|z\| = \|\text{gyr}[x, y](z)\|,$$

which holds as proven by Bachmann et al. (2020, Lemma 11, iv)).

(V5) *Identity Gyroautomorphism.* In each of the three special cases when (i) $x = \mathbf{0}$, or (ii) $y = \mathbf{0}$, or (iii) x and y are parallel in \mathbb{V} , $x\|y$, we have

$$\begin{aligned}\text{gyr}[\mathbf{0}, x](z) &\stackrel{(1)}{=} z, \\ \text{gyr}[x, \mathbf{0}](z) &\stackrel{(2)}{=} z, \\ \text{gyr}[x, y](z) &\stackrel{(3)}{=} z, \quad x\|y,\end{aligned}$$

where (1–3) come from $Ax + By = 0$ in Equation (21). Therefore, we have

$$\text{gyr}[s \odot_K x, t \odot_K x] = \text{gyr}[\alpha_s^{(x)}x, \alpha_t^{(x)}x] = \mathbb{1}.$$

Note that (1–2) are also implied by the first gyrogroup theorem (Ungar, 2022, Theorem 2.10). ■

E.12 Proof of Theorem 23

This proof largely follows the one for Theorem 14.

Proof *Norm Invariance under Gyration.* By Bachmann et al. (2020, Lemma 11), any gyration preserves the Euclidean norm:

$$\|\text{gyr}[a, b](x)\| = \|x\|, \quad \forall x \in \mathfrak{st}_K^n.$$

For the gyronorm, we further have

$$\begin{aligned}\|\text{gyr}[a, b]x\|_{\text{gyr}} &= 2\|\text{Log}_{\mathbf{0}}(\text{gyr}[a, b]x)\|_{\mathbf{0}} \\ &= \frac{2}{\sqrt{|K|}} \tan_K^{-1}\left(\sqrt{|K|} \|\text{gyr}[a, b]x\|\right) \\ &= \frac{2}{\sqrt{|K|}} \tan_K^{-1}\left(\sqrt{|K|} \|x\|\right) \\ &= \|x\|_{\text{gyr}},\end{aligned}$$

with $\tan_K = \tanh$ for $K < 0$ and $\tan_K = \tan$ for $K > 0$.

Isometry of Left Gyrotranslation and Gyroinverse. As shown in Theorem 22, \mathfrak{st}_K^n forms a gyrocommutative gyrogroup. By Theorem 13, the left gyrotranslation and gyroinverse are gyroisometries. ■

E.13 Proof of Theorem 24

Proof *Non-Singular Cases.* Denoting $\|x\|_s = \|x_s\|$, $\forall x \in \mathcal{M}_K^n$, we have

$$(t \log_{\mathbf{0}} x)_s = t \frac{\cos_K^{-1}(\sqrt{|K|}x_t)}{\sqrt{|K|} \|x_s\|} x_s,$$

$$\begin{aligned} \|t \log_{\bar{0}} x\|_s &= t \frac{\cos_K^{-1}(\sqrt{|K|}x_t)}{\sqrt{|K|}}, \\ \sqrt{-K} \|t \log_{\bar{0}} x\|_s &= t \cos_K^{-1}(\sqrt{|K|}x_t), \end{aligned}$$

Putting the above into $\text{Exp}_{\bar{0}}$ in Table 6, one can obtain the result.

For $t = -1$, we have

$$\begin{aligned} -1 \ominus_K^{\mathcal{M}} x &= \frac{1}{\sqrt{|K|}} \left[\begin{array}{c} \cos_K \left(-\cos_K^{-1}(\sqrt{|K|}x_t) \right) \\ \frac{\sin_K \left(-\cos_K^{-1}(\sqrt{|K|}x_t) \right)}{\|x_s\|} x_s \end{array} \right] \\ &\stackrel{(1)}{=} \left[\begin{array}{c} x_t \\ -\frac{\sin_K \left(\cos_K^{-1}(\sqrt{|K|}x_t) \right)}{\sqrt{|K|}\|x_s\|} x_s \end{array} \right], \end{aligned}$$

where (1) comes from $\cos_K(-\theta) = \cos_K(\theta)$ and $\sin_K(-\theta) = -\sin_K(\theta)$. The rest is to show $\frac{\sin_K \left(\cos_K^{-1}(\sqrt{|K|}x_t) \right)}{\sqrt{|K|}\|x_s\|} = 1$:

$$\frac{\sin_K \left(\cos_K^{-1}(\sqrt{|K|}x_t) \right)}{\sqrt{|K|}\|x_s\|} \stackrel{(1)}{=} \frac{\sqrt{\text{sign}(K)(1 - |K|x_t^2)}}{\sqrt{|K|}\|x_s\|} \stackrel{(2)}{=} 1.$$

The derivation above is based on the following:

(1) $\cos_K^2(\theta) + \text{sign}(K) \sin_K^2(\theta) = 1$ implies

$$\sin_K(\theta) = \sqrt{\text{sign}(K)(1 - \cos_K^2(\theta))}, \quad \forall \theta > 0.$$

Considering $\cos_K^{-1}(\theta) \geq 0$ for any $\theta \in \text{dom}(\cos_K^{-1}(\cdot))$, we have (1).

(2)

$$\begin{aligned} \|x\|_K &= \text{sign}(K)x_t^2 + \|x_s\|^2 = \frac{1}{K} \\ \Rightarrow K \|x_s\|^2 &= 1 - |K|x_t^2 \\ \Rightarrow |K| \|x_s\|^2 &= \text{sign}(K)(1 - |K|x_t^2). \end{aligned}$$

Equivalence in the Singular Cases. By Equation (24),

$$\sqrt{K} \|u\| = \frac{\sqrt{K} \|x_s\|}{1 + \sqrt{K}x_t}.$$

Writing $\theta = \cos^{-1}(\sqrt{K}x_t)$ or $\sqrt{K}x_t = \cos \theta$, the sphere constraint gives $\sqrt{K} \|x_s\| = \sin \theta$. Hence

$$\sqrt{K} \|u\| = \frac{\sin \theta}{1 + \cos \theta} = \tan \frac{\theta}{2}, \quad \Rightarrow \tan^{-1}(\sqrt{K} \|u\|) = \frac{\theta}{2}.$$

Therefore (i) \iff (ii) since $t \tan^{-1}(\sqrt{K} \|u\|) = \frac{t\theta}{2}$.

Next, we use the closed form of gyromultiplication Equation (30). For $K > 0$, the gyromultiplication reads

$$t \odot_K^{\mathcal{M}} x = \frac{1}{\sqrt{K}} \begin{bmatrix} \cos(t\theta) \\ \frac{\sin(t\theta)}{\|x_s\|} x_s \end{bmatrix}.$$

If (ii) holds, then $\sin(t\theta) = 0$ and $\cos(t\theta) = -1$, whence $t \odot_K^{\mathcal{M}} x = [-1/\sqrt{K}, 0]^\top = -\bar{\mathbf{0}}$. \blacksquare

E.14 Proof of Theorem 25

Proof We denote $x \oplus_K^{\mathcal{M}} y = [z_t, z_s^\top]^\top$. As the results are trivial under $x = \bar{\mathbf{0}}$ or $y = \bar{\mathbf{0}}$, we assume $x \neq \bar{\mathbf{0}}$ and $y \neq \bar{\mathbf{0}}$ in the following.

Non-Singular Cases. We first consider the non-singular case: i) $K < 0$; ii) $K > 0$, $x, y \neq \pm\bar{\mathbf{0}}$, and $u \neq \frac{v}{K\|v\|^2}$. Since gyroadditions on \mathcal{M}_K^n and \mathfrak{st}_K^n are both defined by Equation (1), we have the following under isometries (Nguyen and Yang, 2023, Lemma 2.2):

$$x \oplus_K^{\mathcal{M}} y = \pi_{\mathfrak{st}_K^n \rightarrow \mathcal{M}_K^n} (\pi_{\mathcal{M}_K^n \rightarrow \mathfrak{st}_K^n} (x) \oplus_K \pi_{\mathcal{M}_K^n \rightarrow \mathfrak{st}_K^n} (y)).$$

Following Equation (E.10), we rewrite the gyroaddition on the stereographic model as

$$u \oplus_K v = \frac{(1 - 2K\langle u, v \rangle - K\|v\|^2)u + (1 + K\|u\|^2)v}{1 - 2K\langle u, v \rangle + K^2\|u\|^2\|v\|^2} = \frac{Au + Bv}{\Delta}.$$

where

$$A = 1 - 2K\langle u, v \rangle - K\|v\|^2, \quad B = 1 + K\|u\|^2, \quad \Delta = 1 - 2K\langle u, v \rangle + K^2\|u\|^2\|v\|^2.$$

Using $\langle u, v \rangle = s_{xy}/(ab)$, $\|u\|^2 = n_x/a^2$, $\|v\|^2 = n_y/b^2$, one obtains

$$A = \frac{ab^2 - 2Kb s_{xy} - Kan_y}{ab^2}, \quad B = \frac{a^2 + Kn_x}{a^2}, \quad \Delta = \frac{D}{a^2b^2}. \quad (\text{E.14})$$

Hence

$$\mathfrak{st}_K^n \ni w = u \oplus_K v = \frac{Au + Bv}{\Delta} = \frac{1}{\Delta} \left(\frac{A}{a} x_s + \frac{B}{b} y_s \right). \quad (\text{E.15})$$

Apply $\pi_{\mathfrak{st}_K^n \rightarrow \mathcal{M}_K^n}$ to w :

$$z_t = \frac{1}{\sqrt{|K|}} \frac{1 - K\|w\|^2}{1 + K\|w\|^2}, \quad z_s = \frac{2w}{1 + K\|w\|^2}. \quad (\text{E.16})$$

A direct expansion (`radius_gyroaddition.py`) yields

$$\|w\|^2 = \frac{A^2\|u\|^2 + B^2\|v\|^2 + 2AB\langle u, v \rangle}{\Delta^2} = \frac{N}{D}.$$

Substituting the above into Equation (E.16) gives

$$z_t = \frac{1}{\sqrt{|K|}} \frac{1 - KN/D}{1 + KN/D} = \frac{1}{\sqrt{|K|}} \frac{D - KN}{D + KN}. \quad (\text{E.17})$$

For z_s , using Equation (E.15), Equation (E.14) and $1 + K\|w\|^2 = (D + KN)/D$,

$$\begin{aligned} z_s &= \frac{2}{1 + KN/D} \cdot \frac{1}{\Delta} \left(\frac{A}{a}x_s + \frac{B}{b}y_s \right) \\ &= \frac{2}{D + KN} \left((Aab^2)x_s + (Ba^2b)y_s \right) \\ &= \frac{2(A_sx_s + A_yy_s)}{D + KN}. \end{aligned}$$

Gyroaddition in Singular Cases ($K > 0$). We show that the definition Equation (31) indeed returns $-\bar{\mathbf{0}}$ in this case.

Step 1: $\text{Log}_{\bar{\mathbf{0}}}(y)$. Write $R = 1/\sqrt{K}$ and choose the polar angle $\theta \in (0, \pi)$ so that

$$x = \begin{bmatrix} R \cos \theta \\ R \sin \theta \hat{s} \end{bmatrix}, \quad y = \begin{bmatrix} -R \cos \theta \\ R \sin \theta \hat{s} \end{bmatrix}, \quad \hat{s} = \frac{x_s}{\|x_s\|}. \quad (\text{E.18})$$

Using $\text{Log}_{\bar{\mathbf{0}}}$ in Table 6,

$$\text{Log}_{\bar{\mathbf{0}}}(y) = \begin{bmatrix} 0 \\ \frac{\cos^{-1}(\sqrt{K} y_t)}{\sqrt{K} \|y_s\|} y_s \end{bmatrix} = \begin{bmatrix} 0 \\ (\pi - \theta) R \hat{s} \end{bmatrix}.$$

Step 2: Parallel transport. With $1 + \sqrt{K} x_t = 1 + \cos \theta \neq 0$ (since $x \neq -\bar{\mathbf{0}}$) and $\text{PT}_{\bar{\mathbf{0}} \rightarrow x}$ in Table 6, we have

$$\text{PT}_{\bar{\mathbf{0}} \rightarrow x}(\text{Log}_{\bar{\mathbf{0}}}(y)) = \begin{bmatrix} 0 \\ (\pi - \theta) R \hat{s} \end{bmatrix} - \frac{K \langle x_s, (\pi - \theta) R \hat{s} \rangle}{1 + \sqrt{K} x_t} \begin{bmatrix} x_t + \frac{1}{\sqrt{K}} \\ x_s \end{bmatrix}. \quad (\text{E.19})$$

Using $\langle x_s, \hat{s} \rangle = \|x_s\| = R \sin \theta$, $KR^2 = 1$, and $x_t = R \cos \theta$, the scalar factor in Equation (E.19) equals

$$\frac{K(\pi - \theta)R \langle x_s, \hat{s} \rangle}{1 + \sqrt{K} x_t} = \frac{(\pi - \theta) \sin \theta}{1 + \cos \theta}.$$

A short simplification then yields the compact form

$$w = \text{PT}_{\bar{\mathbf{0}} \rightarrow x}(\text{Log}_{\bar{\mathbf{0}}}(y)) = R(\pi - \theta) \begin{bmatrix} -\sin \theta \\ \cos \theta \hat{s} \end{bmatrix}. \quad (\text{E.20})$$

Note that $\|w\|_x = R(\pi - \theta)$, so with $\alpha = \sqrt{K} \|w\|_x$ we have $\alpha = \pi - \theta$.

Step 3: Exponential at x . By Table 4,

$$\text{Exp}_x(w) = \cos(\alpha) x + \frac{\sin(\alpha)}{\alpha} w, \quad \alpha = \sqrt{K} \|w\|_x, \quad (\text{E.21})$$

and here $\cos(\alpha) = \cos(\pi - \theta) = -\cos \theta$, $\sin(\alpha) = \sin(\pi - \theta) = \sin \theta$. Substituting Equation (E.18) and Equation (E.20) into Equation (E.21),

$$\text{Exp}_x(w) = R \left[-\cos \theta \begin{bmatrix} \cos \theta \\ \sin \theta \hat{s} \end{bmatrix} + \sin \theta \begin{bmatrix} -\sin \theta \\ \cos \theta \hat{s} \end{bmatrix} \right] = R \begin{bmatrix} -1 \\ 0 \end{bmatrix} = -\bar{\mathbf{0}}.$$

We conclude that $x \oplus_K^{\mathcal{M}} y = -\bar{\mathbf{0}}$ in the singular configuration.

Equivalence in Singular Cases ($K > 0$). Recall the isometry between \mathcal{M}_K^n and \mathfrak{st}_K^n , we rewrite $u = \frac{x_s}{a}$, $v = \frac{y_s}{b}$.

(i) \Rightarrow (ii). Write $\alpha = K \|v\|^2 > 0$. From $u = \frac{v}{\alpha}$ and Equation (25) we get

$$\begin{aligned} y_t &= \frac{1}{\sqrt{K}} \frac{1 - \alpha}{1 + \alpha}, \\ x_t &= \frac{1}{\sqrt{K}} \frac{1 - \frac{1}{\alpha}}{1 + \frac{1}{\alpha}} = -\frac{1}{\sqrt{K}} \frac{1 - \alpha}{1 + \alpha} = -y_t, \\ x_s &= \frac{2u}{1 + K\|u\|^2} = \frac{2v/\alpha}{1 + K\|v\|^2/\alpha^2} = \frac{2v}{1 + \alpha} = y_s, \end{aligned}$$

Hence $x_s = y_s$ and $x_t = -y_t$.

(ii) \Rightarrow (iii). Under $x_s = y_s$ and $x_t = -y_t$, set $n = \|x_s\|^2 = \|y_s\|^2$ and note $s_{xy} = n$, $n_x = n_y = n$. Then,

$$D = a^2 b^2 - 2Kab s_{xy} + K^2 n_x n_y = (ab - Kn)^2.$$

On the sphere \mathbb{S}_K^n , we have the constraint $x_t^2 + \|x_s\|^2 = 1/K$. Since $y_t = -x_t$ and $\|y_s\|^2 = \|x_s\|^2 = n$,

$$\begin{aligned} ab &= (1 + \sqrt{K} x_t)(1 + \sqrt{K} y_t) \\ &= (1 + \sqrt{K} x_t)(1 - \sqrt{K} x_t) \\ &= 1 - K x_t^2 \\ &= 1 - K \left(\frac{1}{K} - n \right) = Kn. \end{aligned}$$

Therefore $D = (ab - Kn)^2 = 0$.

(iii) \Rightarrow (i). This can be obtained by the Cauchy-Schwarz's inequality as Bachmann et al. (2020, Appendix C.2.1.).

Consequences in Singular Cases ($K > 0$). Under (ii) we also have $a + b = 2$, so

$$N = a^2 n + 2abn + b^2 n = (a + b)^2 n = 4n > 0.$$

Using $D = 0$ and $N > 0$, Equation (E.17) gives

$$z_t = \frac{1}{\sqrt{K}} \frac{-KN}{KN} = -\frac{1}{\sqrt{K}}$$

Besides, since for $x_s = y_s$ one checks $A_s + A_y = (a + b)(ab - Kn) = 0$, Equation (E.17) yields $z_s = 0$. On the other hand, $u \oplus_K v = \infty$. ■

E.15 Proof of Theorem 26

Proof This has already been implied in the proof of Theorems 24 and 25. ■

E.16 Proof of Theorem 28

Proof The gyrovector space over the stereographic model is also defined by Equations (1) and (2):

$$\begin{aligned} x \oplus_K y &= \text{Exp}_x(\text{PT}_{\mathbf{0} \rightarrow x}(\text{Log}_{\mathbf{0}}(y))), \\ r \oplus_K x &= \text{Exp}_{\mathbf{0}}(\text{Log}_{\mathbf{0}}(x)), \end{aligned}$$

with $x, y \in \mathfrak{st}_K^n$ and $r \in \mathbb{R}$. Noting that $\pi_{\mathcal{M}_K^n \rightarrow \mathfrak{st}_K^n}(\bar{\mathbf{0}}) = \mathbf{0}$. As $(\mathfrak{st}_K^n, \oplus_M, \odot_M)$ is a gyrovector space, $(\mathcal{M}_K^n, \oplus_K^M, \odot_K^M)$ is also a gyrovector space (Nguyen and Yang, 2023, Theorem 2.4). ■

E.17 Proof of Theorem 30

Proof *Isometries:* The Beltrami–Klein model is isometric to the hyperboloid model by the following diffeomorphisms (Lee, 2018, Theorem 3.7):

$$\pi_{\mathbb{K}_K^n \rightarrow \mathbb{H}_K^n} : \mathbb{K}_K^n \ni x \mapsto \left(\frac{1}{\sqrt{-K}\sqrt{1+K\|x\|^2}}, \frac{x}{\sqrt{1+K\|x\|^2}} \right) \in \mathbb{H}_K^n, \quad (\text{E.22})$$

$$\pi_{\mathbb{H}_K^n \rightarrow \mathbb{K}_K^n} : \mathbb{H}_K^n \ni \begin{bmatrix} x_t \\ x_s \end{bmatrix} \mapsto \frac{x_s}{\sqrt{-K}\xi} \in \mathbb{K}_K^n. \quad (\text{E.23})$$

Combining the isometries Equations (E.22), (E.23), (24) and (25), one can readily obtain the isometries between Beltrami–Klein and Poincaré ball models. Now, we turn to the differential maps. Given a curve over $c(t) \in \mathcal{M}$ with $c(0) = x$ and $c'(0) = v$, the differential maps can be calculated by

$$\begin{aligned} \left. \frac{d\pi_{\mathbb{K}_K^n \rightarrow \mathbb{P}_K^n}(c(t))}{dt} \right|_{t=0} &= \left. \frac{d}{dt} \frac{c(t)}{\left(1 + \sqrt{1 + K\|c(t)\|^2}\right)} \right|_{t=0} \\ &= \frac{\left(1 + \sqrt{1 + K\|x\|^2}\right)v - \left(1 + K\|x\|^2\right)^{-\frac{1}{2}}K\langle x, v \rangle x}{\left(1 + \sqrt{1 + K\|x\|^2}\right)^2} \\ &= \frac{1}{1 + \sqrt{1 + K\|x\|^2}}v - \frac{K\langle x, v \rangle}{\left(1 + \sqrt{1 + K\|x\|^2}\right)^2\sqrt{1 + K\|x\|^2}}x, \\ \left. \frac{d\pi_{\mathbb{P}_K^n \rightarrow \mathbb{K}_K^n}(c(t))}{dt} \right|_{t=0} &= \left. \frac{d}{dt} \frac{2c(t)}{1 - K\|c(t)\|^2} \right|_{t=0} \\ &= \frac{2v(1 - K\|x\|^2) + 4K\langle x, v \rangle x}{(1 - K\|x\|^2)^2} \\ &= \frac{2}{(1 - K\|x\|^2)}v + \frac{4K\langle x, v \rangle}{(1 - K\|x\|^2)^2}x. \end{aligned}$$

Homomorphism: The homomorphism w.r.t. the scalar product can be readily obtained by the Riemannian isometry. Therefore, we first address it before proceeding to the addition. For simplicity, we denote $\phi = \pi_{\mathbb{P}_K^n \rightarrow \mathbb{K}_K^n}$.

Scalar Product: As shown by Ungar (2022), the geodesics under the Beltrami–Klein and Poincaré ball models are

$$\begin{aligned}\gamma_{\phi(x)\rightarrow\phi(y)}^{\mathbb{K}}(t) &= \phi(x) \oplus_{\mathbb{E}} t \odot_{\mathbb{E}} (-\phi(x) \oplus_{\mathbb{E}} \phi(y)), \\ \gamma_{x\rightarrow y}^{\mathbb{P}}(t) &= x \oplus_{\mathbb{M}} t \odot_{\mathbb{M}} (-x \oplus_{\mathbb{M}} y).\end{aligned}$$

Here, we use the fact that the gyro inverses in the Möbius and Einstein gyrovector spaces are exactly the familiar vector inverse. The above geodesics satisfy

$$\phi(x \oplus_{\mathbb{M}} t \odot_{\mathbb{M}} (-x \oplus_{\mathbb{M}} y)) = \phi(x) \oplus_{\mathbb{E}} t \odot_{\mathbb{E}} (-\phi(x) \oplus_{\mathbb{E}} \phi(x)).$$

The above comes from $\phi(\gamma_{x\rightarrow y}^{\mathbb{P}}(t)) = \gamma_{\phi(x)\rightarrow\phi(y)}^{\mathbb{K}}(t)$. Especially, the geodesic starting from the identity element brings

$$\phi(x \odot_{\mathbb{M}} t) = \phi(\gamma_{\mathbf{0}\rightarrow x}^{\mathbb{P}}(t)) = \gamma_{\phi(\mathbf{0})\rightarrow\phi(x)}^{\mathbb{K}}(t) \stackrel{(1)}{=} \phi(x) \odot_{\mathbb{E}} t,$$

where (1) comes from $\phi(\mathbf{0}) = \mathbf{0}$. The above holds for all $x \in \mathbb{P}_K^n$ and $\forall t \in \mathbb{R}$, as every hyperbolic geometry is geodesically complete (Lee, 2018, Page 139).

Addition: We first expand the LHS of Equation (40). Inspired by Mao et al. (2024, Equations 73–76), we express the Möbius addition as $x \oplus_{\mathbb{M}} y = \frac{Bx+Cy}{A}$ by denoting

$$\begin{aligned}A &= 1 - 2K\langle x, y \rangle + K^2\|x\|^2\|y\|^2, \\ B &= 1 - 2K\langle x, y \rangle - K\|y\|^2, \\ C &= 1 + K\|x\|^2.\end{aligned}$$

Then, the Möbius addition is

$$\begin{aligned}\phi(x \oplus_{\mathbb{M}} y) &= \frac{2\frac{Bx+Cy}{A}}{1 - K\left\|\frac{Bx+Cy}{A}\right\|^2} \\ &= \frac{2ABx + 2ACy}{A^2 - K\|Bx + Cy\|^2} \\ &= \frac{2ABx + 2ACy}{A^2 - B^2K\|x\|^2 - C^2K\|y\|^2 - 2BCK\langle x, y \rangle}.\end{aligned}\tag{E.24}$$

Inspired by Mao et al. (2024, Equations 77), we denote $\|x\| = a$, $\|y\| = b$, and $\langle x, y \rangle = ab\cos(\theta)$. In this way, we can resort to the symbolic computation package `SymPy` (Meurer et al., 2017) for the heavy algebra computation, which brings

$$\begin{aligned}\phi(x \oplus_{\mathbb{M}} y) &= \frac{2(-2Kab\cos(\theta) - Kb^2 + 1)}{K^2a^2b^2 - Ka^2 - 4Kab\cos(\theta) - Kb^2 + 1}x \\ &\quad + \frac{2Ka^2 + 2}{K^2a^2b^2 - Ka^2 - 4Kab\cos(\theta) - Kb^2 + 1}y.\end{aligned}\tag{E.25}$$

Now we turn to the RHS of Equation (40). For any $u, v \in \mathbb{K}_K^n$, the Einstein addition can be rewritten as

$$\begin{aligned} u \oplus_E v &= \frac{1}{1 - K \langle u, v \rangle} \left(u + \frac{1}{\gamma_u} v - K \frac{\gamma_u}{1 + \gamma_u} \langle u, v \rangle u \right) \\ &= \frac{1 - K \frac{\gamma_u}{1 + \gamma_u} \langle u, v \rangle}{1 - K \langle u, v \rangle} u + \frac{1}{\gamma_u (1 - K \langle u, v \rangle)} v. \end{aligned} \quad (\text{E.26})$$

The gamma factor and inner product under isometry can be rewritten as

$$\begin{aligned} r_\phi(x) &= \frac{1}{\sqrt{1 + K \|\phi(x)\|^2}} \\ &= \frac{1}{\sqrt{1 + K \left(\frac{2}{1 - K \|x\|^2} \right)^2 \|x\|^2}} \\ &= \frac{1 - K \|x\|^2}{\sqrt{(1 - K \|x\|^2)^2 + 4K \|x\|^2}} \\ &\stackrel{(1)}{=} \frac{1 - K \|x\|^2}{1 + K \|x\|^2}, \\ \langle x, y \rangle &= \frac{4}{(1 - K \|x\|^2)(1 - K \|y\|^2)} \langle x, y \rangle. \end{aligned}$$

where (1) comes from $\|x\|^2 < -\frac{1}{K} \Rightarrow K \|x\|^2 + 1 > 0$. Putting the above into Equation (E.26) and following the same notation as Equation (E.25), we can obtain the following by SymPy:

$$\begin{aligned} \phi(x) \oplus_E \phi(y) &= \frac{2 \cdot (2Kab \cos(\theta) + Kb^2 - 1)}{4Kab \cos(\theta) - (Ka^2 - 1)(Kb^2 - 1)} x \\ &\quad + \frac{-2Ka^2 - 2}{4Kab \cos(\theta) - (Ka^2 - 1)(Kb^2 - 1)} y, \end{aligned}$$

which is clearly equal to Equation (E.25). ■

E.18 Proof of Theorem 31

Proof For simplicity, we denote $\phi = \pi_{\mathbb{P}_K^n \rightarrow \mathbb{K}_K^n}$. The homomorphism and bijection of ϕ imply the homomorphism of its inverse ϕ^{-1} . Also note that $\phi(\mathbf{0}) = \phi^{-1}(\mathbf{0}) = \mathbf{0}$. The above brings

$$\begin{aligned} x \oplus_E y &= \phi \left(\phi^{-1}(x) \oplus_M \phi^{-1}(y) \right) \\ &\stackrel{(1)}{=} \phi \left(\text{Exp}_{\phi^{-1}(x)}^{\mathbb{P}} \left(\text{PT}_{\mathbf{0} \rightarrow \phi^{-1}(x)}^{\mathbb{P}} \text{Log}_{\mathbf{0}}^{\mathbb{P}}(\phi^{-1}(y)) \right) \right) \\ &\stackrel{(2)}{=} \text{Exp}_y^{\mathbb{K}} \left(\text{PT}_{\mathbf{0} \rightarrow y}^{\mathbb{K}} \text{Log}_{\mathbf{0}}^{\mathbb{K}}(y) \right). \end{aligned}$$

The above comes from the following.

- (1) For any Poincaré vectors $u, w \in \mathbb{P}_K^n$, the following holds:

$$\text{PT}_{\mathbf{0} \rightarrow u}^{\mathbb{P}}(v) = \text{Log}_u^{\mathbb{P}}(u \oplus_M \text{Exp}_{\mathbf{0}}^{\mathbb{P}}(v)) \Rightarrow u \oplus_M w = \text{Exp}_u^{\mathbb{P}} \left(\text{PT}_{\mathbf{0} \rightarrow u}^{\mathbb{P}}(\text{Log}_{\mathbf{0}}^{\mathbb{P}}(w)) \right),$$

where $v = \text{Log}_0^{\mathbb{P}}(w)$ and the LHS comes from Ganea et al. (2018, Theorem 4);

(2) It comes from the isometry:

$$\begin{aligned}\text{Exp}_x^{\mathbb{P}}(v) &= \phi^{-1} \left(\text{Exp}_{\phi(x)}^{\mathbb{K}}(\phi_{*,x}(v)) \right), \\ \text{Log}_x^{\mathbb{P}}(y) &= \phi_{*,x}^{-1} \left(\text{Log}_{\phi(x)}^{\mathbb{K}}(\phi(y)) \right), \\ \text{PT}_{x \rightarrow y}^{\mathbb{P}}(v) &= \phi_{*,y}^{-1} \left(\text{PT}_{\phi(x) \rightarrow \phi(y)}^{\mathbb{K}}(\phi_{*,x}(v)) \right).\end{aligned}$$

Similar with the gyro addition, isometry of ϕ implies the following w.r.t. the gyro scalar product:

$$\begin{aligned}t \odot_{\mathbb{E}} x &= \phi \left(t \odot_{\mathbb{M}} \phi^{-1}(x) \right) \\ &\stackrel{(1)}{=} \phi \left(\text{Exp}_{\mathbf{0}}^{\mathbb{P}}(t \text{Log}_{\mathbf{0}}^{\mathbb{P}}(\phi^{-1}(x))) \right) \\ &\stackrel{(2)}{=} \text{Exp}_{\mathbf{0}}^{\mathbb{K}}(t \text{Log}_{\mathbf{0}}^{\mathbb{K}}(x)).\end{aligned}$$

The above comes from the following.

(1) Ganea et al. (2018, Lemma 3);

(2) The isometry of ϕ .

■

E.19 Proof of Theorem 32

Proof Following Theorem 31, we denote $\phi = \pi_{\mathbb{P}_K^n \rightarrow \mathbb{K}_K^n}$ and $\psi = \pi_{\mathbb{K}_K^n \rightarrow \mathbb{P}_K^n}$. The results can be obtained by the properties of isometry and isomorphism of ϕ .

Riemannian exponential and logarithmic maps at the zero vector. First, we recall that the expression of $\text{Exp}_{\mathbf{0}}^{\mathbb{P}}(v)$ and $\text{Log}_{\mathbf{0}}^{\mathbb{P}}(v)$ under Poincaré ball model is the exactly Equations (44) and (45) (Ganea et al., 2018, Equation 13).

By Riemannian isometry, we have the following

$$\begin{aligned}
 \text{Exp}_{\mathbf{0}}^{\mathbb{K}}(v) &= \phi \left(\text{Exp}_{\mathbf{0}}^{\mathbb{P}}(\psi_{*,\mathbf{0}}(v)) \right) \\
 &= \phi \left(\tanh \left(\frac{\sqrt{-K}}{2} \|v\| \right) \frac{v}{\sqrt{-K}\|v\|} \right) \\
 &= \frac{2}{1 - K\|v\|^2} \frac{\tanh \left(\frac{\sqrt{-K}}{2} \|v\| \right)}{\left(\frac{\tanh \left(\frac{\sqrt{-K}}{2} \|v\| \right)}{\sqrt{-K}\|v\|} \right)^2} \frac{v}{\sqrt{-K}\|v\|} \\
 &= \frac{2 \tanh \left(\frac{\sqrt{-K}}{2} \|v\| \right)}{1 + \tanh \left(\frac{\sqrt{-K}}{2} \|v\| \right)^2} \frac{v}{\sqrt{-K}\|v\|} \\
 &\stackrel{(1)}{=} \tanh(\sqrt{-K}\|v\|) \frac{v}{\sqrt{-K}\|v\|},
 \end{aligned}$$

where (1) comes from $\tanh(2x) = \frac{2 \tanh x}{1 + \tanh^2 x}$.

As the inverse of $\text{Exp}_{\mathbf{0}}^{\mathbb{K}}(v)$, $\text{Log}_{\mathbf{0}}^{\mathbb{K}}(x)$, therefore, shares the expression with its counterpart under the Poincaré ball model. Here, we use the properties of isometry to further validate this result:

$$\begin{aligned}
 \text{Log}_{\mathbf{0}}^{\mathbb{K}}(x) &= \phi_{*,\mathbf{0}} \left(\text{Log}_{\mathbf{0}}^{\mathbb{K}}(\psi(x)) \right) \\
 &= 2 \tanh^{-1} \left(\frac{\sqrt{-K}\|x\|}{1 + \sqrt{1 + K\|x\|^2}} \right) \frac{x}{\sqrt{-K}\|x\|}.
 \end{aligned}$$

We only need to show

$$2 \tanh^{-1} \left(\frac{\sqrt{-K}\|x\|}{1 + \sqrt{1 + K\|x\|^2}} \right) = \tanh^{-1}(\sqrt{-K}\|x\|).$$

We denote $a = \sqrt{-K}\|x\| < 1$. Both sides are

$$\text{LHS: } 2 \tanh^{-1} \left(\frac{a}{1 + \sqrt{1 - a^2}} \right) = \ln \left(\frac{1 + \frac{a}{1 + \sqrt{1 - a^2}}}{1 - \frac{a}{1 + \sqrt{1 - a^2}}} \right) = \ln \left(\frac{1 + \sqrt{1 - a^2} + a}{1 + \sqrt{1 - a^2} - a} \right), \quad (\text{E.27})$$

$$\text{RHS: } \tanh^{-1}(a) = \tanh \left(\frac{\sqrt{1 + a}}{\sqrt{1 - a}} \right) = \tanh \left(\frac{\sqrt{1 - a^2}}{1 - a} \right).$$

Note that the below equation holds:

$$\frac{1 + \sqrt{1 - a^2} + a}{1 + \sqrt{1 - a^2} - a} = \frac{\sqrt{1 - a^2}}{1 - a}. \quad (\text{E.28})$$

Geodesic distances.

$$\begin{aligned}
 d^{\mathbb{K}}(x, y) &\stackrel{(1)}{=} d^{\mathbb{P}}(\psi(x), \psi(y)) \\
 &= \frac{2}{\sqrt{-K}} \tanh^{-1} \left(\sqrt{-K} \|\psi(x) \oplus_{\mathbb{M}} \psi(y)\| \right) \\
 &\stackrel{(2)}{=} \frac{2}{\sqrt{-K}} \tanh^{-1} \left(\sqrt{-K} \|\psi(-x \oplus_{\mathbb{E}} y)\| \right) \\
 &= \frac{2}{\sqrt{-K}} \tanh^{-1} \left(\sqrt{-K} \frac{\|-x \oplus_{\mathbb{E}} y\|}{1 + \sqrt{1 + K \|-x \oplus_{\mathbb{E}} y\|^2}} \right),
 \end{aligned}$$

where (1) comes from the isometry, while (2) comes from the isomorphism.

Exponential maps.

$$\begin{aligned}
 \text{Exp}_x^{\mathbb{K}}(v) &\stackrel{(1)}{=} \psi^{-1} \left(\text{Exp}_{\psi(x)}^{\mathbb{P}}(\psi_{*,x}(v)) \right) \\
 &\stackrel{(2)}{=} \psi^{-1} \left(\psi(x) \oplus_{\mathbb{M}} \text{Exp}_{\mathbf{0}} \left(\frac{\lambda_{\psi(x)}^K}{2} \psi_{*,x}(v) \right) \right) \\
 &\stackrel{(3)}{=} x \oplus_{\mathbb{E}} \psi^{-1} \circ \text{Exp}_{\mathbf{0}} \left(\frac{\lambda_{\psi(x)}^K}{2} \psi_{*,x}(v) \right) \\
 &\stackrel{(4)}{=} x \oplus_{\mathbb{E}} \text{Exp}_{\mathbf{0}} \left(\lambda_{\psi(x)}^K \psi_{*,x}(v) \right).
 \end{aligned}$$

The above comes from the following.

- (1) The isometry of ψ ;
- (2) $\text{Exp}_x^{\mathbb{P}}(v) = x \oplus_{\mathbb{M}} \text{Exp}_{\mathbf{0}} \left(\frac{\lambda_x^K}{2} v \right)$;
- (3) The isomorphism of ψ ;
- (4)

$$\begin{aligned}
 \psi^{-1} \circ \text{Exp}_{\mathbf{0}}(v) &= \psi^{-1} \circ \text{Exp}_{\mathbf{0}}^{\mathbb{P}}(v) \\
 &= \psi^{-1} \circ \psi \circ \text{Exp}_{\mathbf{0}}^{\mathbb{K}}(2v) \\
 &= \text{Exp}_{\mathbf{0}}(2v).
 \end{aligned}$$

The rest is to calculate $\lambda_{\psi(x)}^K \psi_{*,x}(v)$:

$$\begin{aligned}
 \lambda_{\psi(x)}^K &= \frac{2}{1 + K \frac{\|x\|^2}{(1 + \sqrt{1 + K\|x\|^2})^2}} \\
 &= \frac{2 \left(1 + \sqrt{1 + K\|x\|^2}\right)^2}{\left(1 + \sqrt{1 + K\|x\|^2}\right)^2 + K\|x\|^2} \\
 &= \frac{2 \left(1 + \sqrt{1 + K\|x\|^2}\right)^2}{2 + 2\sqrt{1 + K\|x\|^2} + 2K\|x\|^2} \\
 &= \frac{\left(1 + \sqrt{1 + K\|x\|^2}\right)^2}{1 + \sqrt{1 + K\|x\|^2} + K\|x\|^2} \\
 &= \frac{\left(1 + \sqrt{1 + K\|x\|^2}\right)}{\sqrt{1 + K\|x\|^2}}, \\
 \lambda_{\psi(x)}^K \psi_{*,x}(v) &= \lambda_{\psi(x)}^K \left(\frac{1}{1 + \sqrt{1 + K\|x\|^2}} v - \frac{K \langle x, v \rangle}{\left(1 + \sqrt{1 + K\|x\|^2}\right)^2 \sqrt{1 + K\|x\|^2}} x \right) \\
 &= \frac{1}{\sqrt{1 + K\|x\|^2}} v - \frac{K \langle x, v \rangle}{\left(1 + \sqrt{1 + K\|x\|^2}\right) (1 + K\|x\|^2)} x.
 \end{aligned}$$

Logarithmic maps.

$$\begin{aligned}
 \text{Log}_x^{\mathbb{K}}(y) &\stackrel{(1)}{=} \psi_{*,x}^{-1} \left(\text{Log}_{\psi(x)}^{\mathbb{P}} \psi(y) \right) \\
 &\stackrel{(2)}{=} \psi_{*,x}^{-1} \left(\frac{2}{\lambda_{\psi(x)}^K} \text{Log}_{\mathbf{0}}(-\psi(x) \oplus_{\mathbb{M}} \psi(y)) \right) \\
 &\stackrel{(3)}{=} \psi_{*,x}^{-1} \left(\frac{2}{\lambda_{\psi(x)}^K} \text{Log}_{\mathbf{0}}(-\psi(x) \oplus_{\mathbb{M}} \psi(y)) \right) \\
 &\stackrel{(4)}{=} \frac{2}{\lambda_{\psi(x)}^K} \phi_{*,\psi(x)} \left(\text{Log}_{\mathbf{0}}(-\psi(x) \oplus_{\mathbb{M}} \psi(y)) \right) \\
 &\stackrel{(5)}{=} \frac{1}{\lambda_{\psi(x)}^K} \phi_{*,\psi(x)} \left(\text{Log}_{\mathbf{0}}(-x \oplus_{\mathbb{E}} y) \right).
 \end{aligned}$$

The above comes from the following.

- (1) The isometry of ψ ;
- (2) $\text{Log}_x^{\mathbb{P}}(y) = \frac{2}{\lambda_x^K} \text{Log}_{\mathbf{0}}(-x \oplus_{\mathbb{M}} y)$;
- (3) The isomorphism of ψ ;

(4) The Linearity of differential maps;

(5)

$$\begin{aligned} \text{Log}_{\mathbf{0}}(-\psi(x) \oplus_{\mathbf{M}} \psi(y)) &= \text{Log}_{\mathbf{0}}^{\mathbb{P}}(-\psi(x) \oplus_{\mathbf{M}} \psi(y)) \\ &= \frac{1}{2} \text{Log}_{\mathbf{0}}^{\mathbb{K}}(\psi^{-1}(-\psi(x) \oplus_{\mathbf{M}} \psi(y))) \\ &= \frac{1}{2} \text{Log}_{\mathbf{0}}^{\mathbb{K}}(-x \oplus_{\mathbf{E}} y). \end{aligned}$$

■

Remark E.10. Mao et al. (2024, Theorem 9) extended the Möbius matrix-vector multiplication (Ganea et al., 2018, Lemma 6) into the Einstein space of the Beltrami–Klein model under $K = -1$, namely $\text{Exp}_{\mathbf{0}}(M \text{Log}_{\mathbf{0}}(x))$. Although their presented formulations are different from the Möbius one, this theorem indicates that matrix-vector multiplications over these two spaces are identical under any negative curvature. The equality can also be readily observed by Equations (E.27) and (E.28).

References

- B. Afsari. Riemannian Lp center of mass: Existence, uniqueness, and convexity. In *Proceedings of the American Mathematical Society*, 2011.
- R. M. Anderson and R. M. May. *Infectious Diseases of Humans: Dynamics and Control*. Oxford University Press, 1991.
- V. Arsigny, P. Fillard, X. Pennec, and N. Ayache. *Fast and simple computations on tensors with log-Euclidean metrics*. PhD thesis, INRIA, 2005.
- J. L. Ba, J. R. Kiros, and G. E. Hinton. Layer normalization. *arXiv preprint arXiv:1607.06450*, 2016.
- G. Bachmann, G. Bécigneul, and O. Ganea. Constant curvature graph convolutional networks. In *ICML*, 2020.
- A. Bdeir, K. Schwethelm, and N. Landwehr. Fully hyperbolic convolutional neural networks for computer vision. In *ICLR*, 2024.
- T. Bendokat, R. Zimmermann, and P.-A. Absil. A Grassmann manifold handbook: Basic geometry and computational aspects. *Advances in Computational Mathematics*, 50(1): 1–51, 2024.
- C. Bonet, B. Malézieux, A. Rakotomamonjy, L. Drumetz, T. Moreau, M. Kowalski, and N. Courty. Sliced-Wasserstein on symmetric positive definite matrices for M/EEG signals. In *ICML*, 2023.
- D. Brooks, O. Schwander, F. Barbaresco, J.-Y. Schneider, and M. Cord. Riemannian batch normalization for SPD neural networks. In *NeurIPS*, volume 32, 2019.

- J. W. Cannon, W. J. Floyd, R. Kenyon, W. R. Parry, et al. Hyperbolic geometry. *Flavors of geometry*, 31(59-115):2, 1997.
- R. Chakraborty. ManifoldNorm: Extending normalizations on Riemannian manifolds. *arXiv preprint arXiv:2003.13869*, 2020.
- R. Chakraborty, J. Bouza, J. Manton, and B. C. Vemuri. Manifoldnet: A deep neural network for manifold-valued data with applications. *IEEE T-PAMI*, 2020.
- I. Chami, Z. Ying, C. Ré, and J. Leskovec. Hyperbolic graph convolutional neural networks. *NeurIPS*, 32, 2019.
- I. Chavel. *Riemannian Geometry: A Modern Introduction*. Cambridge University Press, 1995.
- K. Chen, J. Song, S. Liu, N. Yu, Z. Feng, G. Han, and M. Song. Distribution knowledge embedding for graph pooling. *IEEE TKDE*, 2023a.
- T. Chen, X. Fu, Y. Gao, H. Qian, Y. Wei, K. Yan, H. Zhou, and J. Li. Galaxy walker: Geometry-aware VLMs for galaxy-scale understanding. In *CVPR*, 2025a.
- W. Chen, X. Han, Y. Lin, H. Zhao, Z. Liu, P. Li, M. Sun, and J. Zhou. Fully hyperbolic neural networks. *arXiv preprint arXiv:2105.14686*, 2021.
- Z. Chen, T. Xu, X.-J. Wu, R. Wang, Z. Huang, and J. Kittler. Riemannian local mechanism for SPD neural networks. In *AAAI*, 2023b.
- Z. Chen, Y. Song, G. Liu, R. R. Kompella, X. Wu, and N. Sebe. Riemannian multinomial logistics regression for SPD neural networks. In *CVPR*, 2024a.
- Z. Chen, Y. Song, Y. Liu, and N. Sebe. A Lie group approach to Riemannian batch normalization. In *ICLR*, 2024b.
- Z. Chen, Y. Song, R. Wang, X. Wu, and N. Sebe. RMLR: Extending multinomial logistic regression into general geometries. In *NeurIPS*, 2024c.
- Z. Chen, Y. Song, T. Xu, Z. Huang, X.-J. Wu, and N. Sebe. Adaptive log-Euclidean metrics for SPD matrix learning. *IEEE TIP*, 2024d.
- Z. Chen, Y. Song, X. Wu, G. Liu, and N. Sebe. Understanding matrix function normalizations in covariance pooling from the lens of Riemannian geometry. In *ICLR*, 2025b.
- Z. Chen, Y. Song, X. Wu, and N. Sebe. Gyrogroup batch normalization. In *ICLR*, 2025c.
- Z. Chen, X.-J. Wu, and N. Sebe. Riemannian networks over full-rank correlation matrices. *arXiv preprint*, 2025d.
- J. Dai, Y. Wu, Z. Gao, and Y. Jia. A hyperbolic-to-hyperbolic graph convolutional network. In *CVPR*, 2021.
- P. David and W. Gu. A Riemannian structure for correlation matrices. *Operators and Matrices*, 13(3):607–627, 2019.

- M. P. Do Carmo and J. Flaherty Francis. *Riemannian Geometry*, volume 6. Springer, 1992.
- A. Edelman, T. A. Arias, and S. T. Smith. The geometry of algorithms with orthogonality constraints. *SIAM journal on Matrix Analysis and Applications*, 20(2):303–353, 1998.
- M. Fréchet. Les éléments aléatoires de nature quelconque dans un espace distancié. In *Annales de l'institut Henri Poincaré*, 1948.
- O. Ganea, G. Bécigneul, and T. Hofmann. Hyperbolic neural networks. *NeurIPS*, 31, 2018.
- Z. Gao, C. Xu, F. Li, Y. Jia, M. Harandi, and Y. Wu. Exploring data geometry for continual learning. In *CVPR*, 2023.
- G. Garcia-Hernando, S. Yuan, S. Baek, and T.-K. Kim. First-person hand action benchmark with RGB-D videos and 3D hand pose annotations. In *CVPR*, 2018.
- D. Groisser. Newton’s method, zeroes of vector fields, and the riemannian center of mass. *Advances in Applied Mathematics*, 33(1):95–135, 2004.
- K. Grover, G. J. Gordon, and C. Faloutsos. CurvGAD: Leveraging curvature for enhanced graph anomaly detection. In *ICML*, 2025a.
- K. Grover, H. Yu, X. Song, Q. Zhu, H. Xie, V. N. Ioannidis, and C. Faloutsos. Spectro-Riemannian graph neural networks. In *ICLR*, 2025b.
- K. He, X. Zhang, S. Ren, and J. Sun. Deep residual learning for image recognition. In *CVPR*, 2016.
- N. He, M. Yang, and R. Ying. Lorentzian residual neural networks. In *KDD*, 2025.
- U. Helmke and J. B. Moore. *Optimization and Dynamical Systems*. Springer Science & Business Media, 2012.
- C. Hu, R. Wang, X. Song, T. Zhou, X.-J. Wu, N. Sebe, and Z. Chen. A correlation manifold self-attention network for EEG decoding. In *IJCAI*, 2025.
- Z. Huang and L. Van Gool. A Riemannian network for SPD matrix learning. In *AAAI*, 2017.
- Z. Huang, C. Wan, T. Probst, and L. Van Gool. Deep learning on Lie groups for skeleton-based action recognition. In *CVPR*, 2017.
- Z. Huang, J. Wu, and L. Van Gool. Building deep networks on Grassmann manifolds. In *AAAI*, 2018.
- Z. Huang, J. Wu, and L. Van Gool. Manifold-valued image generation with Wasserstein generative adversarial nets. In *AAAI*, 2019.
- S. Ioffe and C. Szegedy. Batch normalization: Accelerating deep network training by reducing internal covariate shift. In *ICML*, 2015.
- C. Ju, R. J. Kobler, L. Tang, C. Guan, and M. Kawanabe. Deep geodesic canonical correlation analysis for covariance-based neuroimaging data. In *ICLR*, 2024.

- H. Karcher. Riemannian center of mass and mollifier smoothing. *Communications on Pure and Applied Mathematics*, 30(5):509–541, 1977.
- I. Katsman, E. Chen, S. Holalkere, A. Asch, A. Lou, S. N. Lim, and C. M. De Sa. Riemannian residual neural networks. *NeurIPS*, 2024.
- R. R. Khan, P. Chlenski, and I. Pe’er. Hyperbolic genome embeddings. In *ICLR*, 2025.
- D. P. Kingma. Adam: A method for stochastic optimization. *arXiv preprint arXiv:1412.6980*, 2014.
- R. Kobler, J.-i. Hirayama, Q. Zhao, and M. Kawanabe. SPD domain-specific batch normalization to crack interpretable unsupervised domain adaptation in EEG. *NeurIPS*, 2022a.
- R. J. Kobler, J.-i. Hirayama, and M. Kawanabe. Controlling the Fréchet variance improves batch normalization on the symmetric positive definite manifold. In *ICASSP*, 2022b.
- M. Kochurov, R. Karimov, and S. Kozlukov. Geopt: Riemannian optimization in pytorch. *arXiv preprint arXiv:2005.02819*, 2020.
- G. Lebanon and J. Lafferty. Hyperplane margin classifiers on the multinomial manifold. In *ICML*, 2004.
- J. M. Lee. *Introduction to Riemannian Manifolds*, volume 2. Springer, 2018.
- M. Lezcano Casado. Trivializations for gradient-based optimization on manifolds. In *NeurIPS*, 2019.
- S. Li, M. Kawanabe, and R. J. Kobler. SPDIM: Source-free unsupervised conditional and label shift adaptation in EEG. In *ICLR*, 2025.
- Z. Lin. Riemannian geometry of symmetric positive definite matrices via Cholesky decomposition. *SIAM Journal on Matrix Analysis and Applications*, 40(4):1353–1370, 2019.
- J. Liu, A. Shahroudy, M. Perez, G. Wang, L.-Y. Duan, and A. C. Kot. NTU RGB+D 120: A large-scale benchmark for 3D human activity understanding. *IEEE T-PAMI*, 2019.
- A. Lou, I. Katsman, Q. Jiang, S. Belongie, S.-N. Lim, and C. De Sa. Differentiating through the Fréchet mean. In *ICML*, 2020.
- M. Lovrić, M. Min-Oo, and E. A. Ruh. Multivariate normal distributions parametrized as a riemannian symmetric space. *Journal of Multivariate Analysis*, 74(1):36–48, 2000.
- J. H. Manton. A globally convergent numerical algorithm for computing the centre of mass on compact Lie groups. In *The 8th Control, Automation, Robotics and Vision Conference, 2004.*, 2004.
- Y. Mao, J. Gu, M. C. Werner, and D. Zou. Klein model for hyperbolic neural networks. *arXiv preprint arXiv:2410.16813*, 2024.

- A. Meurer, C. P. Smith, M. Paprocki, O. Čertík, S. B. Kirpichev, M. Rocklin, A. Kumar, S. Ivanov, J. K. Moore, S. Singh, et al. Sympy: symbolic computing in python. *PeerJ Computer Science*, 3:e103, 2017.
- M. Müller, T. Röder, M. Clausen, B. Eberhardt, B. Krüger, and A. Weber. Documentation mocap database HDM05. Technical report, Universität Bonn, 2007.
- G. Namata, B. London, L. Getoor, B. Huang, and U. Edu. Query-driven active surveying for collective classification. In *10th International Workshop on Mining and Learning with Graphs*, 2012.
- X. S. Nguyen. The Gyro-structure of some matrix manifolds. In *NeurIPS*, 2022a.
- X. S. Nguyen. A Gyrovector space approach for symmetric positive semi-definite matrix learning. In *ECCV*, 2022b.
- X. S. Nguyen and S. Yang. Building neural networks on matrix manifolds: A gyrovector space approach. In *ICML*, 2023.
- X. S. Nguyen, S. Yang, and A. Histace. Matrix manifold neural networks++. In *ICLR*, 2024.
- A. Pal, M. van Spengler, G. M. D. di Melendugno, A. Flaborea, F. Galasso, and P. Mettes. Compositional entailment learning for hyperbolic vision-language models. In *ICLR*, 2024.
- Y.-T. Pan, J.-L. Chou, and C.-S. Wei. Matt: A manifold attention network for EEG decoding. *NeurIPS*, 2022.
- A. Paszke, S. Gross, F. Massa, A. Lerer, J. Bradbury, G. Chanan, T. Killeen, Z. Lin, N. Gimelshein, L. Antiga, et al. Pytorch: An imperative style, high-performance deep learning library. *NeurIPS*, 2019.
- X. Pennec, P. Fillard, and N. Ayache. A Riemannian framework for tensor computing. *IJCV*, 2006.
- J. G. Ratcliffe. *Foundations of Hyperbolic Manifolds*. Springer, 2006.
- P. Sen, G. Namata, M. Bilgic, L. Getoor, B. Galligher, and T. Eliassi-Rad. Collective classification in network data. *AI magazine*, 29(3):93–93, 2008.
- A. Shahroudy, J. Liu, T.-T. Ng, and G. Wang. NTU RGB+D: A large scale dataset for 3D human activity analysis. In *CVPR*, 2016.
- R. Shimizu, Y. Mukuta, and T. Harada. Hyperbolic neural networks++. In *ICLR*, 2021.
- O. Skopek, O.-E. Ganea, and G. Bécigneul. Mixed-curvature variational autoencoders. In *ICLR*, 2020.
- Y. Thanwerdas. Permutation-invariant log-Euclidean geometries on full-rank correlation matrices. *SIAM Journal on Matrix Analysis and Applications*, 45(2):930–953, 2024.

- Y. Thanwerdas and X. Pennec. Theoretically and computationally convenient geometries on full-rank correlation matrices. *SIAM Journal on Matrix Analysis and Applications*, 43(4): 1851–1872, 2022.
- D. Ulyanov, A. Vedaldi, and V. Lempitsky. Instance normalization: The missing ingredient for fast stylization. *arXiv preprint arXiv:1607.08022*, 2016.
- A. A. Ungar. *Analytic Hyperbolic Geometry and Albert Einstein’s Special Theory of Relativity (Second Edition)*. World Scientific, 2022.
- M. Van Spengler, E. Berkhout, and P. Mettes. Poincaré ResNet. In *ICCV*, 2023.
- R. Vemulapalli, F. Arrate, and R. Chellappa. Human action recognition by representing 3D skeletons as points in a Lie group. In *CVPR*, 2014.
- H. Wang, Z. Li, and W. Zhang. Get the best of both worlds: Improving accuracy and transferability by grassmann class representation. In *ICCV*, 2023.
- R. Wang, C. Hu, Z. Chen, X.-J. Wu, and X. Song. A Grassmannian manifold self-attention network for signal classification. In *IJCAI*, 2024a.
- R. Wang, X.-J. Wu, Z. Chen, C. Hu, and J. Kittler. SPD manifold deep metric learning for image set classification. *IEEE TNNLS*, 2024b.
- R. Wang, S. Jin, Z. Chen, X. Luo, and X.-J. Wu. Learning to normalize on the SPD manifold under Bures-Wasserstein geometry. In *CVPR*, 2025.
- Y.-C. Wong. Differential geometry of Grassmann manifolds. *Proceedings of the National Academy of Sciences*, 57(3):589–594, 1967.
- Y. Wu and K. He. Group normalization. In *ECCV*, 2018.
- R. Yataka, K. Hirashima, and M. Shiraishi. Grassmann manifold flows for stable shape generation. In *NeurIPS*, 2023.
- M. Zhang and Y. Chen. Link prediction based on graph neural networks. In *NeurIPS*, 2018.
- W. Zhao, F. Lopez, J. M. Riestenberg, M. Strube, D. Taha, and S. Trettel. Modeling graphs beyond hyperbolic: Graph neural networks in symmetric positive definite matrices. In *Joint European Conference on Machine Learning and Knowledge Discovery in Databases*, pages 122–139. Springer, 2023.